UNIVERSITÀ
DEGLI STUDI
DI PADOVA

Head Office: Università degli Studi di Padova
Department of Chemical Sciences

Ph.D. COURSE IN:
SCIENCE AND ENGINEERING OF MATERIALS AND NANOSTRUCTURES
XXX CYCLE

DEVELOPMENT AND CHARACTERIZATION OF NANOSTRUCTURED MATERIALS FOR ORGANIC AND HYBRID SOLAR CELLS

Coordinator: Ch.mo Prof. Giovanni Mattei
Supervisor: Prof. Lorenzo Franco

Ph.D. student: Alberto Privitera

PREFACE

"I'd put my money on the sun and solar energy. What a source of power! I hope we don't have to wait until oil and coal run out before we tackle that."

This statement that sounds rather contemporary was pronounced in 1931 by Thomas Edison, the godfather of electricity-intensive living. Edison's appreciation of solar energy was a bright soothsaying. Indeed, the sun is the world's biggest source of energy and in an hour and a quarter the amount of sunlight that threads through the clouds to the Earth's surface could power all the world's electricity, vehicles, boilers, furnaces and cooking stoves for a year.

Over the last half century many efforts have been devoted to sun-to-electricity conversion and the race for the highest efficiency and the cheapest production led to inorganic solar cell technologies. The best multijunction solar cells to date even reach power conversion efficiencies over 40%. However, this point of view does not consider one crucial point: the scarcity of materials to produce these solar cells. Indeed, considering the upscaling production to the terawatt scale needed for global supply, available technologies would hit a natural resource limitation. Therefore, the cheapest or most efficient technology is not automatically the best choice for widespread adoption. Instead, the technology that can be up-scaled the best will have a serious impact on energy production in the long run.

Organic photovoltaics aims to offer an environmentally-friendly, low-cost and up-scalable alternative. Nevertheless, this technology still lacks high power conversion

efficiencies and long stability. The intense scientific and technological research on this fundamental problem gave rise to a variety of new ideas and promising results. One of the new line of development for solar cells material is focused on the incorporation of colloidal nanocrystals and nanoparticles within organic photoactive layers. This approach has demonstrated to be a promising field to tackle the main issues related to the low efficiency. Thus far, the fabrication and the technological development of new hybrid nanostructured photovoltaic devices have been one of the spotlights of scientific research. However, the detailed understanding of the photophysics behind these recent solar cells is still under debate. Therefore, a gap can be recognized between the development of the devices and the comprehension of the photophysical interactions underlying hybrid nanostructured photoactive layers.

In this thesis, both the development of new hybrid photoactive nanocomposites and their detailed photophysical investigation is carried out. By the analysis of the photophysical interactions between nanostructures and organic photovoltaic materials, this work aims at enabling the reader to underpin the relevance of applying nanostructured architectures in organic photovoltaics for the development of next-generation solar cells.

TABLE OF CONTENTS

ABSTRACT

In the last years, the massive evolution of modern technologies has gradually created an alarming gap between the production and the consumption of energy. Traditional energy resources are no longer sufficient to satisfy the demand of energy without spoiling earth environment. Solar photovoltaics represents a highly promising technology to tackle this global energy issue. The thorough scientific discussion on this fundamental topic gave rise to interesting results and the organic solar cells (OSCs) are one of these achievements.

One major reason of the development and the increasing interest in this new technology is its eco-friendliness and the potentially low-cost production of solar modules on flexible (plastic) substrates. Furthermore, new applications are expected by flexible or semitransparent organic solar cells. Nevertheless, two main problems must be overcome before this promising technology replaces the long-established silicon solar cells: the low power conversion efficiency and the scarce stability. In order to tackle these fundamental issues the research efforts must be focused towards both the development of new materials and their detailed photophysical and morphological characterization.

Recently the application of nanostructured architectures within the active layers of OSCs has demonstrated to be an efficient alternative to boost solar cell efficiency. Indeed, the nanometric miniaturization of materials opened a huge amount of possibilities to tune and bolster their optical and electrical properties.

In this thesis work, the potentialities of the nanostructured architectures are explored. In particular, the attention of this work is addressed towards the development and the photophysical characterization of new hybrid nanostructured photoactive materials. Three different families of nanostructures, colloidal Quantum Dots, Carbon Dots, and

hybrid organic/inorganic perovskite nanoparticles, are blended with organic photovoltaic materials. The thorough investigation of the photo-physical and morphological interactions between the nanostructures and the organic materials aims to investigate these nanocomposite as new photoactive materials for next-generation solar cells.

The first step of the work focuses on the investigation of a prototypical active layer consisting in binary blends of the fullerene derivative PCBM and CdSe/CdS core-shell Quantum Dots (QDs) capped with different ligands (namely, oleylamine, octadecanethiol, and propanethiol). The double purpose is both to demonstrate that QDs do not influence only the morphology of the active layers, as it is often reported in literature, but also its photophysics and to unravel the pivotal role of QDs ligands on the electron transfer process, which is fundamental for organic solar cells. Through the combined use of steady-state, time resolved and pulsed electron paramagnetic resonance (EPR) techniques the photophysical role of QDs in OSCs is clarified and the possibility to tailor the electron transfer process through the proper choice of QDs ligands is demonstrated.

The second part of the work aims at promoting the application of carbon dots (CDs) as electron donor materials for OSCs. CDs seem to be a good alternative to colloidal QDs, thanks to their low toxicity, good biocompatibility and peculiar photo-physical properties, however their poor solubility in organic solvents and mediocre electron-donor properties hampered their photovoltaic application. To tackle these critical issues, the synthesis and photo-physical characterization of N-doped CDs functionalized with two different thiophene-containing groups is carried out in this work. The functionalization intends to enhance the electron donating properties of the CDs and improve their solubility in organic solvents. The increased solubility allows to investigate the photoinduced interactions of functionalized CDs with the PCBM in solution and in solid blends. Through the combined cyclic voltammetry, optical and EPR analysis the enhanced electron donor capabilities of the functionalized CDs are demonstrated and the electron transfer process is characterized in detail.

Finally, the last part of the work concentrates on the hybrid organic inorganic perovskite nanostructures. These recent nanostructures are definitely the best candidate to compete

with silicon solar cells since their bulk counterpart has already provided record photovoltaic efficiencies in less than five years. However, the application of perovskite nanoparticles (PNPs) in organic solar cells has been scarcely investigated so far. Therefore, in this thesis work the synthesis of PNPs and the investigation of their interaction with both the PCBM and the semiconducting polymer P3HT is carried out. After the confirmation of the obtained synthesis through optical spectroscopy, X-ray diffraction and XPS analysis, the electron transfer from PNPs to PCBM is investigated. In particular, the effect of the ligand length on the electron transfer is examined, probing the process with two different PNPs ligands: octylamine and oleylamine. Successively, the role of the PNPs in blend with P3HT is studied. A triple effect of PNPs on the polymer properties is observed: (1) an increment of the dimension of P3HT crystalline domains, (2) a p-doping of the P3HT, and (3) an enhanced interchain order.

The results of this work underpin the relevance of applying nanostructured architectures in organic photovoltaic materials, highlighting their beneficial role not only in morphology, but also in the main photo-physical processes that take place in solar cells. Additionally, the relevant role of the tailored surface engineering of nanostructures in the process of solar energy conversion is evidenced. All these observations aim at providing guidelines for the design and the fabrication of highly efficient solar cells.

ABSTRACT (ITA)

Negli ultimi anni, a causa della frenetica evoluzione delle moderne tecnologie, si è andata a creare una divergenza sempre più allarmante tra la produzione e il consumo di energia. Le risorse tradizionali di energia, infatti, non sono più sufficienti a soddisfare la sempre crescente domanda energetica senza il drastico effetto di rovinare l'ambiente che ci circonda. Il fotovoltaico rappresenta una tecnologia promettente per affrontare il problema energetico mondiale. La ricerca scientifica focalizzata su questo argomento fondamentale ha dato luogo a risultati molto interessanti e le celle solari organiche ne sono una dimostrazione.

Uno dei principali motivi dello sviluppo e del crescente interesse in questa nuova tecnologia è legato alla sua ecosostenibilità e al basso costo di produzione dei moduli solari che solitamente avviene su substrati (polimerici) flessibili. Inoltre, dal momento che questa tecnologia si basa sulla produzione di celle solari trasparenti e flessibili numerose applicazioni innovative sono già previste. Nonostante ciò, prima che il forovoltaico organico prevalga sulle celle solari al silicio che già da anni si sono affermate nella scena mondiale, due problemi principali devono essere affrontati: la bassa efficienza e la scarsa stabilità dei moduli fotovoltaici organici. Per far fronte a questi problemi la migliore alternativa è focalizzare gli sforzi della ricerca sia sullo sviluppo di nuovi materiali sia sulla loro caratterizzazione fotofisica e morfologica.

Recentemente, l'applicazione di nanostrutture all'interno degli strati attivi delle celle solari organiche ha dimostrato di essere un'idea efficace per promuovere l'efficienza delle celle solari. Infatti è risaputo che la miniaturizzazione a livello nanometrico dei materiali apre la strada a numerose possibilità per controllare e incrementare le loro proprietà ottiche ed elettriche.

In questo lavoro di tesi, le potenzialità delle nanostrutture vengono prese in considerazione. In particolare, l'attenzione di questa tesi è indirizzata allo sviluppo e alla caratterizzazione fotofisica di nuovi materiali nanostrutturati fotoattivi ibridi. Tre differenti famiglie di nanostrutture, i Quantum Dots colloidali, i Carbon Dots e le nanoparticelle di perovskite ibrida organica/inorganica, sono state incorporate all'interno di materiali fotovoltaici organici. Lo studio dettagliato delle interazioni fotofisiche e morfologiche tra le nanostrutture e i materiali organici ha permesso di considerare questi materiali nanocompositi come materiali promettenti per il fotovoltaico di nuova generazione.

La prima parte del lavoro si focalizza sullo studio di uno strato fotoattivo costituito dal derivato fullerenico PCBM e dai Quantum Dots (QDs) core-shell di CdSe/CdS funzionalizzati con tre leganti differenti (l'oleilammina, l'ottadecantiolo e il propantiolo). Il primo obiettivo è stato dimostrare che la presenza dei QDs non solo influenza la morfologia degli strati fotoattivi delle celle solari, come spesso è riportato in letteratura, ma anche la loro fotofisica. Il secondo obiettivo è stato chiarire il ruolo fondamentale dei leganti dei QDs nel processo di trasferimento elettronico, processo essenziale nelle celle solari organiche. Attraverso l'uso combinato di tecniche di risonanza magnetica elettronica di stato stazionario, risolte nel tempo e impulsate, il ruolo fotofisico dei QDs nelle celle solari organiche è stato chiarito in grande dettaglio. Inoltre, è stata dimostrata la possibilità di controllare opportunamente il processo di trasferimento elettronico attraverso la scelta accurata dei leganti dei QDs.

La seconda parte del lavoro mira a promuovere l'applicazione dei Carbon Dots (CDs) come materiale elettron-donatore nelle celle solari organiche. I CDs hanno dimostrato di essere una buona alternativa ai QDs colloidali grazie alla loro bassa tossicità e biocompatibilità e alle loro peculiari proprietà fotofisiche. Nonostante ciò, la loro scarsa solubilità in solventi organici e le loro deboli proprietà elettron-donatrici hanno ostacolato sinora la loro applicazione nel campo fotovoltaico. Per far fronte a queste criticità, è stata portata a termine la sintesi e la caratterizzazione fotofisica di CDs contenenti atomi di azoto e funzionalizzati con due diversi gruppi tiofenici. Lo scopo della funzionalizzazione è stato incrementare le proprietà elettron-donatrici dei CDs e migliorare la loro solubilità in solventi organici. L'aumento di solubilità ha permesso di studiare la loro interazione fotofisica con il PCBM sia in soluzione che in film. Tramite

l'utilizzo della voltammetria ciclica, della spettroscopia ottica e della spettroscopia EPR, sono state dimostrate le buone proprietà di trasferimento elettronico fotoindotto in questi materiali e il processo di trasferimento elettronico è stato studiato in dettaglio.

Infine, l'ultima parte di questo lavoro di tesi si concentra sulle nanoparticelle di perovskite ibrida organica/inorganica. Le perovskiti ibride sono a tutti gli effetti il miglior candidato nella corsa per sostituire le convenzionali celle solari al silicio. Negli ultimi cinque anni le perovskiti ibride massive hanno stabilito record straordinari di efficienza fotovoltaica. Nonostante ciò, l'utilizzo delle nanoparticelle di perovskite nelle celle solari organiche non è stato ancora studiato a fondo. Per ovviare a ciò, nell'ultima parte di questo lavoro è stata portata a termine la sintesi delle nanoparticelle di perovskite ed è stata studiata la loro interazione sia con il PCBM che con il polimero semiconduttore P3HT. Dopo aver confermato l'avvenuta sintesi mediante spettroscopia ottica, diffrazione a raggi X e spettroscopia di fotoemissione a raggi X, è stato analizzato il processo di trasferimento elettronico fotoindotto tra le nanoparticelle di perovskite e il PCBM. In particolare, grazie all'utilizzo di nanoparticelle funzionalizzate con due diversi leganti (ottilammina ed oleilammina), il ruolo fondamentale della lunghezza dei leganti nel processo di trasferimento elettronico è stato evidenziato. Successivamente, l'attenzione è stata rivolta al nanocomposito di nanoparticelle di perovskite e P3HT. In questo caso, è stato osservato che la presenza delle nanoparticelle di perovskite svolge un triplice effetto sulle proprietà del polimero: (1) un incremento nella dimensione dei domini cristallini, (2) un drogaggio di tipo p, e (3) un aumento dell'ordine intercatena nella fase polimerica.

I risultati di questo lavoro di tesi evidenziano la rilevanza delle nanostrutture nei materiali fotovoltaici organici sottolineando il loro effetto positivo non solo sulla morfologia, ma anche su tutti i principali processi fotofisici che hanno luogo nelle celle solari. Inoltre, viene dimostrata l'importante funzione dell'ingegnerizzazione superficiale di queste nanostrutture al fine di favorire il processo di conversione dell'energia solare. Tutti questi risultati hanno lo scopo di promuovere la progettazione, lo sviluppo e l'efficienza delle celle solari di nuova generazione.

OUTLINE

This thesis deals with the development and the spectroscopic investigation of various nanostructured hybrid photoactive blends. The main purpose of the thesis is to understand the photophysical processes that arise from the interaction between nanostructured architectures and organic photovoltaic materials and to suggest these hybrid nanocomposites for next-generation solar cells. The work reported in this thesis was carried out at the Department of Chemical Sciences of the University of Padova, under the supervision of Prof. Lorenzo Franco in the period 2014 - 2017.

This manuscript is organized in five Chapters.

Chapter 1 provides the description of the contextual background of this thesis. First, the organic photovoltaics is described with particular attention given to the photophysics behind Organic Solar Cells (OSCs). Subsequently, Quantum Dot Solar Cells are depicted focusing on the three different families of nanostructures (namely, (1) colloidal Quantum Dots, (2) carbon dots, and (3) hybrid organic/inorganic perovskite nanoparticles) which are employed in the subsequent chapters of the thesis.

Chapter 2 gives a brief description of the theoretical background and the experimental apparatus of Electron Paramagnetic Resonance (EPR) spectroscopy, which is the main spectroscopic technique adopted in this thesis.

Chapter 3 reports a detailed photo-physical description of the main processes that take place within prototypical PCBM/colloidal Quantum Dots (QDs) blends. The chapter is developed on a twofold aim: (1) to track the dynamics of charge generation, separation, and recombination in PCBM/QDs blends and (2) to unravel the role of QDs ligands on

the photoinduced electron transfer from QDs to PCBM in order to control and maximize this process.

Chapter 4 illustrates the functionalization and the spectroscopic characterization of N-doped carbon dots (CDs) with the aim to take advantage of the increased electron-donating properties of functionalized CDs for photoinduced electron transfer. Moreover, the photophysical picture of PCBM/CDs blends is reported suggesting these nanocomposites for all-carbon solar cells.

Chapter 5 contains the main results concerning perovskite nanoparticles (PNPs) nanocomposite. The chapter is divided in three sections. First, the synthesis and the basic characterization of PNPs are shown. Second, the detailed spectroscopic analysis carried out on PCBM/PNPs blends is reported and the photophysical properties of these blends are clarified. Finally, the enhanced electrical and morphological properties of semiconducting polymer P3HT deriving from its interaction with PNPs are depicted.

PART I

BACKGROUND

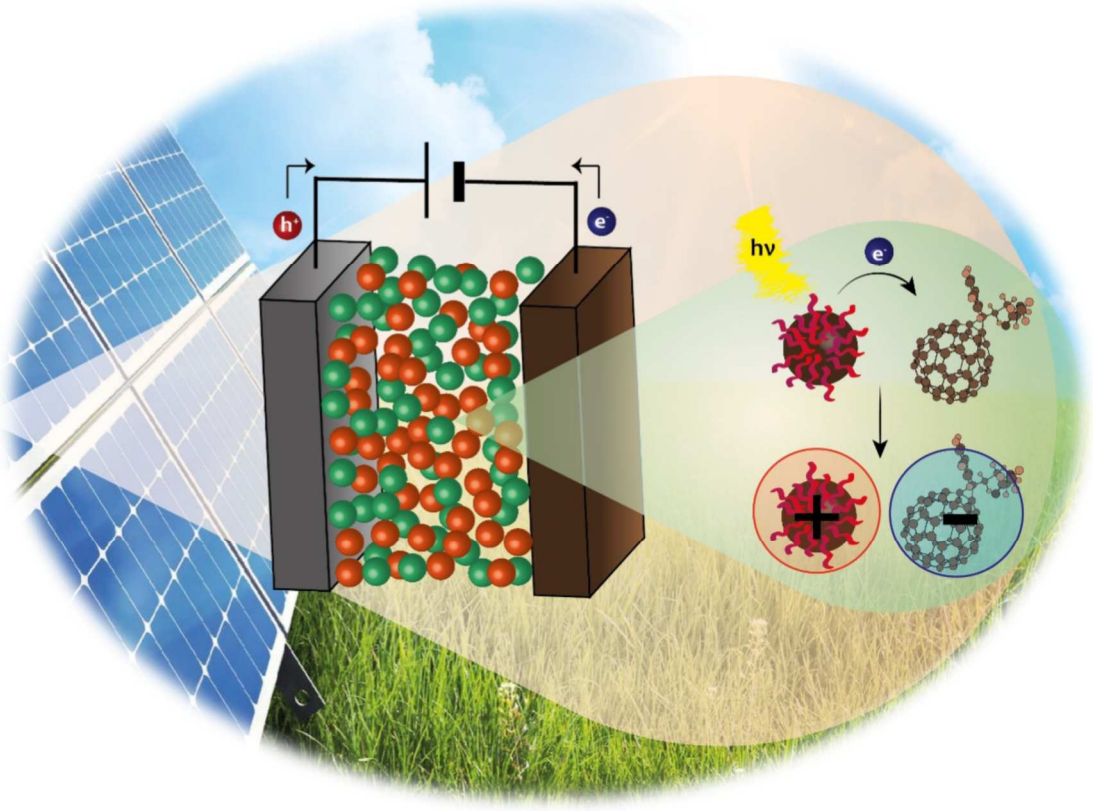

CHAPTER 1.
NEXT GENERATION SOLAR CELLS

Among the technologies for renewable energy, photovoltaics has gathered increasing interest from both the public and policymakers, due to its abundance and minimal impact on the environment.[1] The history of solar cells can be divided in three parts.[2] The "first-generation" of solar cells was based on crystalline silicon wafers. The main problem of this technology was the requirement of a large amount of starting material. To tackle this issue, a "second generation" of solar cells was developed from the early 1980s. These solar cells, based on amorphous silicon, copper indium gallium selenide (CIGS) or CdTe, revealed to be a promising technology due to the large reduction in costs by the minimisation of the quantity of the used material. Nevertheless, the need of a new technology that allowed to overcome the unfavourable balance between costs and energy produced was urgent. Therefore, a "third generation" of solar cells was developed. "Third generation" solar cells aimed to decrease costs to well below the 1 $/W level of second-generation photovoltaics potentially to 0.20 $/W or better, by significantly increasing efficiencies but maintaining the economic and environmental cost advantages of thin-film deposition techniques.[3] Among the various examples, multijunction solar cells, employing several layers of semiconductors to cover the whole solar spectrum, retain the record in terms of conversion efficiencies. The problem with these devices is the extremely high manufacturing cost that relegate these solar cells to applications where other advantages, such as weight, are more important. Conversely, emerging third generation solar cells have been trying to reduce production

costs using low cost processing techniques and materials. Even if the efficiencies of these solar cells are lower compared to nowadays multijunction devices the possible exploitation in real world applications makes them appealing and has attracted a lot of interest. In this category of solar cells, organic photovoltaics established itself as a highly promising technology.[4]

In this chapter, the materials, the device structure and the photophysics of organic photovoltaic devices are described. In addition, the description of the scientific developments of this technology is given, addressing the recent solar cells involving nanostructured architectures, which is the focus of this thesis. In section 1.1, the background of organic photovoltaics is presented by describing the principal device structures and the main materials used in the active layers of these solar cells. In section 1.2, the fundamentals of organic photovoltaic photophysics are explained. This section is fundamental in order to understand the main results obtained in this work. Finally, in section 1.3, Quantum Dots Solar Cells are described, focusing on the three different families of nanostructures, namely colloidal Quantum Dots, carbon dots, and hybrid organic/inorganic perovskite nanoparticles, all discussed in this thesis.

1.1 Organic Solar Cells

1.1.1 Device Structures

Organic solar cells, also referred as organic photovoltaics (OPV), take advantage of organic molecules, such as semiconducting organic polymers, small organic molecules and fullerene derivatives, for solar to electrical energy conversion. This technology was first developed in the 1990s and attracted a lot of interest mainly due to the reduced cost of production and due to additional possible applications.[5]

The first organic solar cells were based on single organic layers sandwiched between two metal electrodes of different work functions.[5] The rectifying behaviour of single layer devices was attributed to the formation of a Schottky-barrier between the p-type (hole conducting) organic layer and the metal with the lower work function. However, the power conversion efficiencies reported were generally poor.

This issue led the scientific community to introduce the bilayer heterojunction concept, in which two organic layers with specific electron or hole transporting properties were

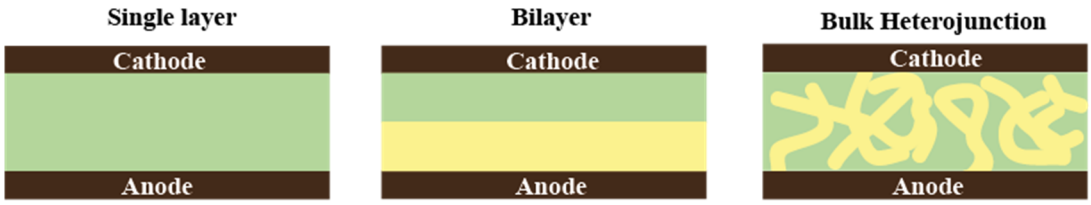

Figure 1.1 Schematic representation of single layer, bilayer and bulk heterojunction solar cells.

sandwiched between the electrodes. In 1986, Tang reported about 1% power conversion efficiency and this result was not surmounted for many years.[6]

Nevertheless, the real revolution occurred when the concept of Bulk Heterojunction (BHJ) was developed.[7] The bulk heterojunction (BHJ) architecture consists in a three-dimensional interpenetrated network of electron-donor and electron-acceptor materials and was introduced for the first time by blending acceptor/donor polymers. Moreover, the observation of a photoinduced electron transfer from optically excited conjugated polymers to the C_{60} molecule and the observation of highly increased photoconductivities upon C_{60} addition to the conjugated polymers paved the way to the polymer/fullerene BHJ that allowed to reach higher power conversion efficiencies.[8]

In Figure 1.1, a scheme which sums up the three types of organic solar cells (namely, monolayer, bilayer and bulk heterojunction) is reported.

The standard device structure for a BHJ solar cell consists in a sandwich of different layers.[5] The simplest device structure is characterized by an active layer consisting in semiconducting polymers or organic molecules sandwiched between the anode, commonly made by indium tin oxide (ITO), and the cathode, usually made by a lower work function metal, such as calcium or aluminium. Since the injection of charges to the electrodes and the photovoltage critically depend on the interfaces between the active layer and the electrodes, interfacial layers are often used for lowering the contact resistance. An ultrathin (<1 nm) layer of LiF between the metal cathode and the organic semiconductor is usually deposited to reduce the cathode workfunction and improve the contact efficiency. On the other side, the deposition of a layer of PEDOT:PSS (a molecularly doped conjugated polymer with a higher work function than ITO), between the anode and the active layer can contribute to enhance the PCE of the solar cell.

1.1.2 ACTIVE LAYER MATERIALS

The heart of the organic solar cells is the active layer. An intensive research has been carried out in the last few decades with the aim to create highly efficient photoactive organic layers and significant processes in OPV efficiency and stability has been made since the development of regioregular poly(3-hexylthiophene) (P3HT).[9] Nevertheless, P3HT still remains the most widely studied donor polymer for organic photovoltaic applications. P3HT is polymerized from thiophene rings with a hexyl side-chain attached. The regioregular P3HT has a partially crystalline structure in solution-processed thin films and a high conductivity. The band gap (~1.9 eV) of P3HT limits light absorption to below 650 nm, therefore the need to develop new, low band gap polymers with better spectral overlap with the solar irradiation is pivotal.

A popular approach to lower the optical bandgap consists in synthesizing polymers with alternating electron-rich and electron-poor moieties.[10] The possibility to take advantage of the different combinations of electron-rich and electron poor moieties allows fine tuning of the electronic energy levels (HOMO and LUMO) and hence to obtain lower optical band gaps. In addition, the alternating electron-rich and electron-poor moieties can create a 'push-pull' effect for intramolecular charge transfer. Such internal charge transfer transition in alternating donor-acceptor polymers increases the absorption coefficient, shifts the absorption to longer wavelengths and facilitates charge photogeneration in polymer/fullerene blends.

On the other hand, fullerene derivatives are the most used electron acceptors for polymer-based solar cells.[11] Many of the record breaking device efficiencies involved donor-acceptor polymers blended with fullerenes. Fullerenes are hollow spheres or ellipsoids composed of carbon atoms that are interconnected by alternating single and double bonds. There is a large variety of fullerenes with different numbers of carbon atoms and the most common fullerene is the spherical C_{60} that consists of 60 carbon atoms. Fullerenes are mostly produced by electrical arc-discharge from graphite electrodes in a helium atmosphere. The most famous fullerene derivative is PCBM ([6,6]-phenyl-C61 butyric acid methyl ester), a C_{60} derivative widely used due to its high solubility and ability to form appropriate blend morphology with most of the semiconducting polymers used. This property is beneficial for good charge transport.

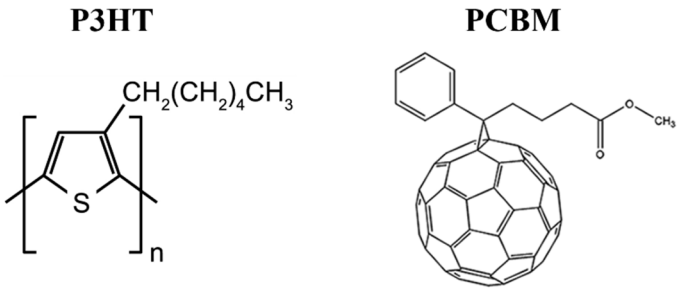

Figure 1.2 Molecular structure of the organic photovoltaic materials used in this thesis (namely, the semiconducting polymer P3HT and fullerene derivative PCBM).

In Figure 1.2 the molecular structures of P3HT and PCBM are reported. These two materials have been investigated in this thesis for a double motivation. First, these materials still play a critical role not only in organic solar cells but in many other optoelectronic devices. Second, these materials have been widely studied in the past and can be considered as good model systems. Despite only PCBM and P3HT have been studied in this work, the possibility to extend the results to other polymers and/or fullerene derivatives seems feasible.

1.1.3 Current-Voltage Characteristic

The performance of a photovoltaic device is based on its ability to convert incident light into electric current, and is typically assessed with a current-voltage (J-V) curve, also named *characteristic curve*.[12] The J-V curve is obtained with light intensity at 1 sun illumination (AM1.5) using a solar simulator. In Figure 1.3, an example of a typical characteristic curve for a solar cell is reported. From the curve, many important parameters can be obtained.

The short circuit current (J_{SC}) is the current generated when there is no potential difference between the electrodes, while the open circuit voltage (V_{OC}) is the maximum voltage available at zero current. The power of a solar cell is maximum when a particular combination of J and V is present. The ratio between the maximum power (i.e. $J_M \cdot V_M$) and the product J_{SC} and V_{OC} is called Fill Factor. The Fill Factor is essentially a measure of quality of solar cell and is directly affected by the values of the cell's series and shunt resistances and diode losses. Increasing the shunt resistance and decreasing the series resistance lead to a higher Fill Factor, thus resulting in greater efficiency.

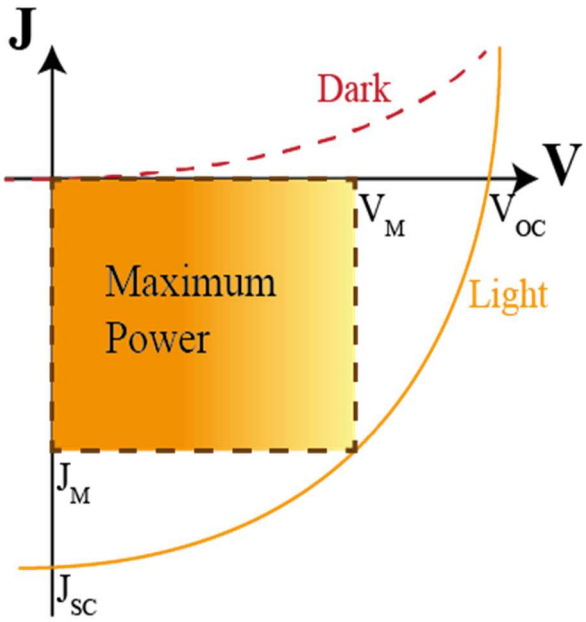

Figure 1.3 A typical current-voltage curve for organic solar cells. From the characteristic curve it is possible to assess the performance of the photovoltaic device.

From the J-V curve it is possible to calculate the power conversion efficiency (PCE) of the solar cell through the following relationship:

$$PCE = \frac{J_{SC} \times V_{OC} \times FF}{P_{incident}} \quad (1)$$

where $P_{incident}$ is the incident light power.

Another parameter that is also important to device performance is quantum efficiency. The external quantum efficiency (EQE) is defined as the ratio of the number of charge carriers being collected by the electrodes to the number of incident photons at a particular wavelength. On the other hand, internal quantum efficiency (IQE) refers to the ratio of charge carriers being collected by the electrodes to the number of photons being absorbed. The EQE depends on both light absorption and charge collection, and is therefore always lower in value than the IQE.

1.2 Photophysics of Organic Solar Cells

To improve organic photovoltaic performances and to move forward to commercial applications, the in depth understanding of the photophysical processes occurring in OPV devices is fundamental, in particular those that limit efficiency. Before describing

in much more detail the various processes that take place in solar cells a brief overview is given in the following.[13]

Upon photon absorption (usually by the donor), an electron is promoted to an excited state, forming an exciton which is tightly bound by Coulombic interaction. When this exciton diffuses to a donor-acceptor interface, electron transfer can take place from the donor to the acceptor. Due to the low dielectric constant of organic materials, this electron transfer process can result in the formation of a bound polaron pair, rather than free charges as in inorganic semiconductors. This bound polaron pair still needs to overcome the Coulombic interaction in order to fully dissociate into free charge carriers or polarons. These polarons then need to be transported to the electrodes for photocurrent generation.

1.2.1 Exciton Generation and Charge Transfer

The processes that follow the light absorption in a semiconducting polymer and/or fullerene derivative are depicted in the Jablonsky diagram in Figure 1.4. When a photon of the appropriate wavelength is absorbed, photoexcitation from the ground state S_0 to some singlet excited states S_n (n= 1, 2…) can occur. Electrons excited in higher singlet states (e.g. S_2) can undergo rapid internal conversion to the lowest lying excited state S_1.[14]

In isolated molecules, the main decay pathways of the lowest singlet excited state are the decay to the ground state (via radiative emission or non-radiative processes) or the conversion to the excited triplet state (S = 1) via Intersystem Crossing (ISC) promoted by spin−orbit interaction.

The radiative decay from S_1 to S_0 is the fluorescence. Due to vibrational relaxation and internal conversion, the photon energy being emitted is less than that initially absorbed. This gives rise to a red-shift in energy of the emission band relative to the absorption band which is known as the *Stokes shift*.

On the other hand, ISC is a non-radiative process which allows the lowest singlet state S_1 (anti parallel spins) to become a triplet state T_1 with parallel spin.[15] The decay of this triplet state to the ground state is forbidden by the spin selection rules and can only take place when there is efficient spin-orbit coupling. Semiconducting polymers generally

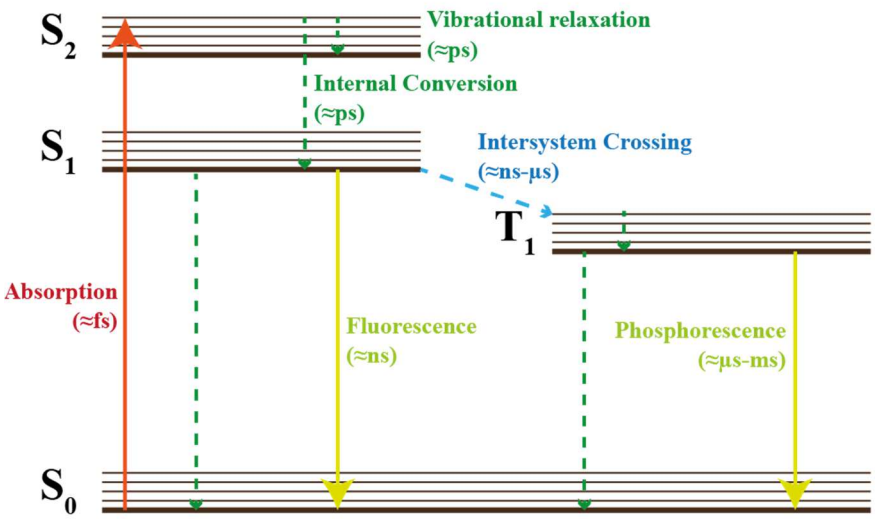

Figure 1.4 Jablonski diagram showing electronic transitions in isolated organic molecules and the corresponding timescales. Dotted lines indicate non-radiative transitions, while straight lines indicate transitions that involves photons.

have weak spin-orbit coupling unless heavy elements are incorporated; hence the radiative emission of triplet state via phosphorescence is a weak and slow process. Therefore, such triplet states are generally longer-lived than singlet states. For further details about triplet state, refer to chapter 2.

In the presence of a suitable electron donor or acceptor, the excited state (either singlet or triplet) can undergo a charge transfer at the donor/acceptor interface. The difference in electron affinities between the donor and acceptor at the interface creates a downhill driving energy for exciton dissociation. Sometimes an exciton is formed away from a donor/acceptor interface within the active layer blend. In such case, the exciton needs to diffuse to an interface before it returns to ground state, in order for exciton dissociation to occur. The distance which an exciton can travel before decaying to ground state is known as the *exciton diffusion length*.[16]

Two charge transfer processes can occur: electron and hole transfer.[17] Electron transfer can occur if the LUMO of the donor is higher in energy than the LUMO of the acceptor. In this case an electron from the LUMO of the donor jumps into the LUMO of the acceptor. Conversely, the hole transfer can occur when the photon is absorbed by the acceptor molecule if the HOMO of the acceptor is lower in energy than the HOMO of the donor. When this condition is satisfied, a hole from the HOMO of the acceptor jumps into the HOMO of the donor.

1.2.2 Charge Transfer State

Following charge transfer process at the D/A interface, the electron is localised on the acceptor LUMO while the hole is localised on the donor HOMO. This has been suggested to create a partially bound electron-hole pair which is called charge transfer (CT) state.[17] This intermediate state is also called bound polaron pair or geminate pair. Since in CT states, the electron and hole are spatially separated from each other compared to an exciton, but there is still significant mutual Coulombic attraction, this state can be considered to be an intermediate species between a tightly bounded exciton and fully dissociated free charges.

1.2.3 Charge Separated State

The CT state can immediately recombine (geminate recombination) and decay to the singlet ground state or may dissociate to produce free charge carriers in the material (CS states). The precise mechanisms by which efficient charge separation can occur in organic systems with high exciton binding energy is not yet fully understood. One of the proposed models is the following. After its generation, the CT state may be initially formed with an excess of thermal energy (*hot* CT state). Based on Onsager theory, this hot CT state may dissociate into free charge carriers if the electron-hole separation is greater than Coulomb capture radius.[18]

Another possible evolution of CT states is the singlet to triplet interconversion, which is expected to proceed within a few tens of nanoseconds. Consequently, the CT states in triplet state may recombine to a lower-lying triplet excited state (triplet exciton) localized either on the electron acceptor or on the electron donor species depending on their relative energies.

In Figure 1.5 the energy level diagram representing the main processes that occur in the photoactive material of a solar cell after light absorption is depicted.

1.2.4 Loss Processes

In addition to the various steps described in the previous sections, many loss processes can take place in a solar cell. The loss channels limit the efficiency of the solar cell and

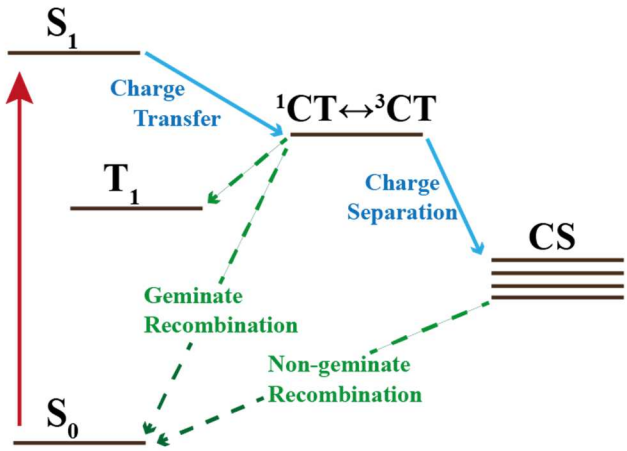

Figure 1.5 Energy level diagram summarizing the main photophysical processes that can occur in organic solar cells.

therefore it is of pivotal importance to identify and characterize them. The different loss channels are depicted in Figure 1.6 and include the following:[19]

1. Incomplete photon absorption in the photoactive layer, mainly for three reasons:
   a. The optical gap of organic materials is typically larger than 1.4 eV; hence, photons with lower energies are not absorbed by the photoactive layer.
   b. The photoactive layer is rather thin (100 nm) and thus captures only a fraction of the above-bandgap photons because of its limited optical density.
   c. The fullerene derivatives, frequently used as acceptors, contribute only little to the total absorbance of the photoactive layer, as their absorption cross sections are small in the visible spectrum.
2. The exciton diffusion length in organic materials is limited to about 10 nm. This is a consequence of the short exciton lifetime, which is typically in the range of several hundred picoseconds, and the incoherent exciton motion process.
3. The CT state does not necessarily evolve into a CS state, because of the geminate recombination process. Geminate recombination is a unimolecular process as it involves an electron and a hole that originate from the same photogenerated exciton. In addition, charges that have dissociated but remain trapped in their respective domains such that the same electron and hole recombine, is also a unimolecular, geminate recombination. This type of recombination has been reported to occur on a short timescale (from picoseconds to nanoseconds), and can therefore often compete with charge dissociation.

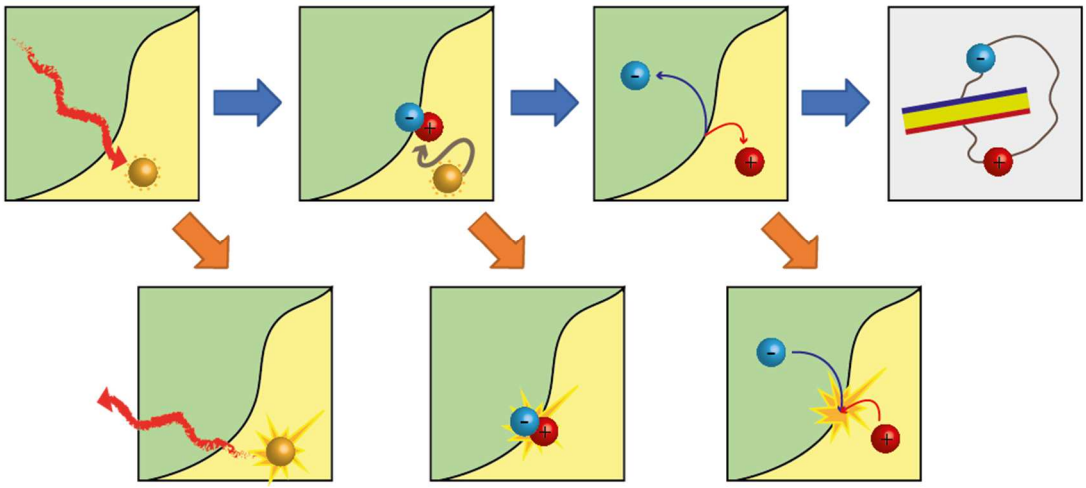

Figure 1.6 Pictorial representation of the photophysical processes taking place in organic solar cells leading to current photogeneration (upper row) and main photocurrent loss mechanisms (lower row). Adapted from ref 19.

4. Charge carrier recombination of dissociated free charges during the transport to the electrodes is often the main loss mechanism for state-of-the-art solar cells. This type of recombination processes is called *non-geminate recombination*. This process occurs from the CS state to the ground state, but it is also possible to proceed through the formation of CT states which then recombine. As non-geminate recombination requires the diffusion of charges to within their Coulomb capture radius, it occurs on a longer timescale than geminate recombination, typically nanoseconds to milliseconds.
5. Finally, at the electrodes the charge carriers are extracted from the photoactive layer. Extraction of the wrong carrier type can be avoided by adding to the device hole- or electron-blocking layers. Note that energy barriers at the metal–organic interface can hinder charge extraction.

The afore-mentioned loss mechanisms are responsible for the reduction of the photocurrent, the fill factor and the open circuit voltage of the solar cells. In order to tackle these losses, many approaches have been used in literature. One of the most promising is the insertion of Quantum Dots within the active layers of organic solar cells.[20]

1.3 QUANTUM DOTS SOLAR CELLS

Hybrid system composed of conjugated polymers and semiconductor QDs are of particular interest for several reasons.[21,22] First, QDs give a significant contribution to the absorption of sunlight thanks to their favourable energy gap and their high absorption coefficient in the spectral range of solar radiation. This observation was for example shown by Zutz et al.[23] who presented absorption spectra measured through the active layer of P3HT/CdSe QDs solar cells. Furthermore, measurements of the external quantum efficiency showed that light absorption in QDs can also lead to a significant contribution to the photocurrent generated by P3HT/CdSe QDs solar cells if the surface of QDs is suitably designed. A second potential advantage of QDs originates from the quantum size effect. The change of energy gap as a function of particle size is accompanied by a shift of the conduction and valence band edges. If in a hybrid solar cell the QDs act as electron donors, an up-shift of the acceptor's conduction band edge means an increase of the effective bang gap of the donor/acceptor heterojunction. Since the effective band gap is related to the maximum possible open-circuit voltage, tuning the particle size of QDs should enable adjusting the energy levels in order to improve the open-circuit voltage.[24] Third, the presence of QDs blended with semiconducting polymers significantly reduce the energetic driving force for charge separation due to the high dielectric permittivity and consequently low electrostatic binding energy within the inorganic phase. Nelson et al.[25] explored this concept recently by combining several types of conjugated polymers with in situ formed CdS QDs.

Although the large variety of advantages, one of the intrinsic shortcoming of binary polymer/QDs hybrids is poor, hopping-type electron transport in the inorganic phase. In order to reach the percolation threshold, high QDs loading within the polymer is required, which can lead to non-optimal morphologies and hence to reduced hole transport in the organic phase. One way to circumvent this problem is to take advantage of elongated nanocrystals such as nanorods to improve the electron transport along a particular direction. Huynh et al.[26] convincingly demonstrated the beneficial effect of elongated nanocrystals by comparing hybrid solar cells with quasi-spherical CdSe nanoparticles and CdSe nanorods of different lengths. Another approach was based on the blending of a three-component blend based on semiconducting polymer/QDs/fullerene derivative system. This approach enabled to enhance free

charge carrier generation through QDs addition in a standard organic solar cell, while maintaining efficient transport.[27]

Clearly, the presence of QDs blended with organic active layers showed many promising effects and the investigation of the photophysical interactions between nanostructured architectures with semiconducting polymers and fullerene derivatives is of pivotal importance. In addition, the development of new blends taking advantage of the challenging properties of further nanostructures, in addition to the common III-V QDs, can be useful for the enhancement of photovoltaic efficiency. In the following, three different families of nanoparticles are described in detail. The photophysical interactions between these three families of nanoparticles (namely, core-shell QDs, carbon dots and hybrid perovskite nanoparticles) and the previously described P3HT and PCBM have been investigated in this thesis.

1.3.1 COLLOIDAL QUANTUM DOTS (QDS)

PHYSICS OF QDS

In a bulk semiconductor crystal (*i.e.* dimensions >> 10 nm), electrons and holes are free to move and there is no confinement.[28] The energy levels of holes and electrons are so close to each other and packed such that energy bands are formed. The highest occupied band (*valance band*) and the lowest unoccupied band (*conduction band*) are separated by the *energy bandg*ap E_g. As the size dimensions of the bulk crystal are decreased down to the nanoscale (≤ 15 nm), the number of participating valence states is also decreased. The width of each band of allowed states then begins to narrow, resulting in nearly discrete, atomic-like states for nanocrystals.[29,30] In Figure 1.7 the electronic energy levels of bulk and nanoscale semiconductors are reported.

The band gap of a semiconductor is an intrinsic property and much efforts has been devoted to tune it in the last 60 years. This ability is fundamental for modern optoelectronic devices, which are based on the excitonic state, i.e. a Coulombically bound electron–hole pair that is formed at the band gap. In a bulk semiconductor, this bound electron-hole system (*exciton*) form a hydrogen like atom. The separation between the electron and the hole is called *Bohr radius*. When the size dimensions of the semiconductor are reduced to the Bohr radius strict terminal boundaries begin to be

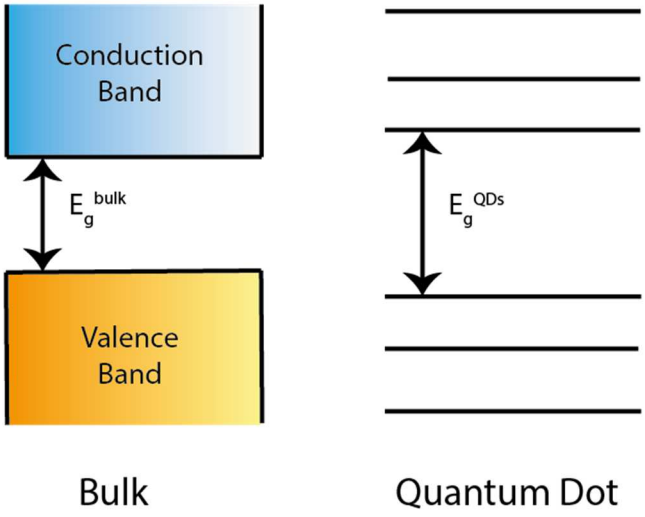

Figure 1.7 Representation of energetic levels of a bulk semiconductor crystal and a semiconductor QD. The reduced size dimension results in atomic-like energy levels.

enforced for the carrier wavefunctions. This action of quantum confinement essentially creates a *particle-in-a-box* situation, affecting the energy-level spacing for band gap states. The band gap energy of the nanocrystal quantum dot is well described by the following relationship:[31]

$$E_g^{QD} = E_g^{bulk} + \frac{\hbar^2 \pi^2}{2\mu R^2} - \frac{1.8e^2}{4\pi\epsilon_0 \epsilon R} \qquad (2)$$

where μ is the reduced electron–hole mass, ε is the dielectric constant of the semiconductor, ε_0 that of free space and R is the quantum dot radius.

In combination with the continuous flexibility offered by size-tuning, the band gap can also be engineered through more traditional methods: impurity doping, strain fields, and heterostructuring.[31,32] In particular, heterostructure formation involving a layered growth procedure allows to obtain different nanoparticle band gap configurations (depicted in Figure 1.8).

Type I band alignment generally results in both carriers being localized to the smaller band gap material, which increases wavefunction overlap. Oftentimes, colloidal QDs are terminated with a much larger band gap material, which serves as a passivation layer, protecting against the formation of dangling-bond trap states that act as localization sites and non-radiative recombination channels. An example of this type of QDs are CdSe/ZnS core-shell QDs. On the other hand, Type II alignment minimizes the

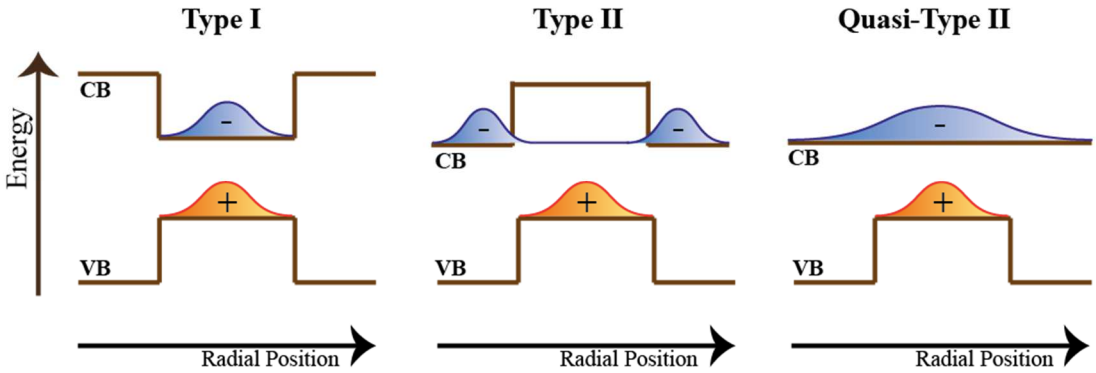

Figure 1.8 Common types of QDs heterostructures. In Type I band structures, both electron and hole are co-localized to the same material. Type II heterojunctions minimize wavefunction overlap by forcing charges to occupy adjacent materials. In quasi-Type II heterostructures, one charge is localized while its partner is delocalized across the two materials.

overlap of carrier wavefunctions due to the opposing mismatch between corresponding charge carrier bands. In type-II systems, shell growth aims at a significant redshift of the emission wavelength of the QDs. The staggered band alignment leads to a smaller effective bandgap than each one of the constituting core and shell materials. The interest of these systems is the possibility to manipulate the shell thickness and thereby tune the emission colour towards spectral ranges, which are difficult to attain with other materials. Among this family of QDs, CdTe/CsSe and CdS/ZnSe core-shell QDs are two examples. Finally, an intermediate regime also exists, termed quasi-Type II, in which there is nearly equal alignment between the two conduction or valence bands. An example of this type of QDs are CdSe/CdS core-shell QDs.

Optical Properties and Passivating Ligands

As the band gap of these nanoscale materials can be continuously varied by changing various parameters, also optical properties can be tuned. Band-edge absorption and emission frequencies directly scale with the degree of quantum confinement of the exciton. With decreasing particle radii, this is observed as a corresponding optical blue-shift in both absorption and emission.

In order to achieve good optical properties, particular attention has to be pointed to defects on the surface of QDs.[33] Since defects such as dangling bonds are detrimental for QD photoluminescence and other optoelectronic properties, their removal is a

crucial issue. One of the alternatives to passivate the surface defects is the use of organic ligand molecules binding to the QD surface.[34,35]

In addition, the presence of organic ligands plays a pivotal role in the photoinduced interactions between QDs and other molecules. Indeed, since the photoinduced interactions between two different species are ruled by surface processes, the proper engineering of surface ligands can favour a large variety of surface processes, such as the photoinduced electron transfer. Finally, QDs ligands enable the stabilization of QDs in solution and the proper ligand choice can favour the film deposition and therefore the properties of the final device.

The majority of established QD synthetic routes use organic ligands composed by a long hydrocarbon tail and a polar head. Such surfactants include oleic acid, oleylamine, and/or trioctylphosphine oxide. The choice of ligands is determined by the coordination chemistry with QD surface atoms. On the basis of the Lewis concept of acids and bases, a hard Lewis acid will favour bonding to a hard Lewis base such as oxygen. By contrast, metal cations with a lower charge to size ratio (soft acids) prefer bonding to thiol surfactants (soft bases).[36,37]

1.3.2 Carbon Dots (CDs)

Synthesis

Carbon Dots (CDs) have provided a step forward from inorganic QDs. Research on these organic nanoparticles has grown rapidly since their first discovery in 2004 with many applications and potential benefits. CDs are a class of compounds mainly composed of carbon atoms forming extended conjugated graphene-like structures joined together by sp^3 hybridized carbon domains, with a size below 10 nm. The CD edges usually consist of functional groups containing heteroatoms such as carboxylic, carbonyl and hydroxyl groups.[38-40]

Many methods have been proposed to prepare CDs during the last decade, which can be classified into top-down and bottom-up approaches.[39,40] Using the “top-down” approach, pristine CDs are broken off from mass carbon materials through arc-discharge, laser-ablation and electrochemical soaking, followed by chemical treatments. Using the “bottom-up” approach, CDs are formed through agglomeration of

carbon contents generated from decomposition or pyrolysis of small organic molecules. Although both are successful in the preparation of CDs, they suffer from three main problems: (1) carbonaceous aggregation during carbonization, (2) size control and uniformity, and (3) surface properties that are critical for solubility and selected applications. Among the various bottom-up synthetic routes, microwave assisted hydrothermal synthesis distinguished itself to be a rapid and low-cost method to synthesize CDs. Basically, a solution of organic precursors in ultrapure water is prepared and irradiated in a microwave oven. Although a poor control over size can be obtained through this method, this route is extremely rapid, scalable, cost-effective and eco-friendly.[41]

Surface modification is a powerful method to tune the surface properties of materials for selected applications. There are many approaches for functionalizing the surface of CDs through the surface chemistry or interactions, such as covalent bonding,[42] coordination,[43] π-π interactions[44] and sol-gel technology.[45] Since the majority of CDs are rich in oxygen containing groups, the covalent bonding is the most used methodology. Surface passivation via covalent bonding of amine-containing agents, for example, is a common method to improve the photoluminescence of CDs. In addition, the covalent functionalization allows to achieve higher stability.

Finally, doping is a widely-used approach to tune the photoluminescent properties of CDs. Various doping methods with dozens of elements such as nitrogen, sulphur, and phosphor have been reported to tune the properties of CDs. N-doping is the most studied way to enhance the emission of the CDs by inducing an upward shift in the Fermi level of electrons in the conduction band. The easiest way to dope CDs is by starting from organic precursor molecules that contain nitrogen groups.

In Figure 1.9, a schematic illustration of CDs synthetic approaches, and modification including functionalization and doping is reported.

OPTICAL PROPERTIES

Generally, CDs show strong optical absorption in the UV region with a tail extending into the visible range. For the carbon core, a maximum peak at ca. 230 nm is ascribed to the π–π* transition of aromatic C–C bonds, whereas a shoulder at 300 nm is attributed to the n–π* transition of C=O bonds or other connected groups.[46] Moreover, the

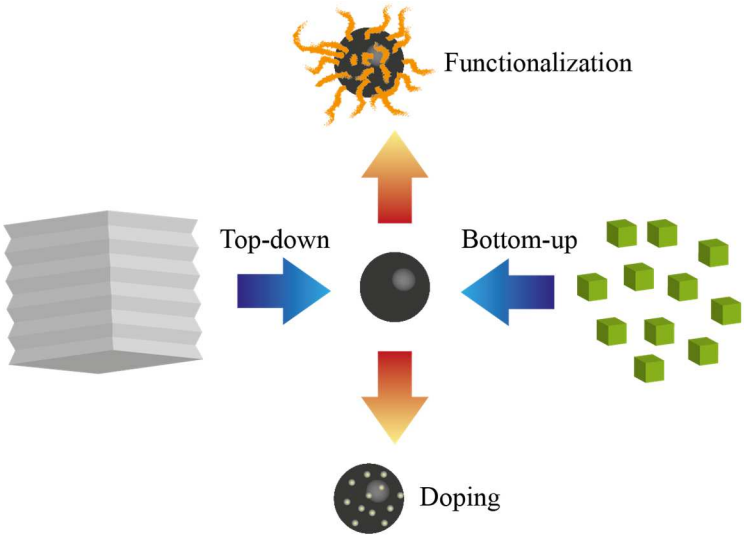

Figure 1.9 Schematic illustration of CQDs preparation via "top-down" and "bottom-up" approaches, and modification including functionalization, doping and nanohybrids. Adapted from ref 40.

connected chemical groups contribute to the absorption at the UV–visible regions. The observed deviations in absorption spectra data, indeed, indicate differences in composition or structure of CDs.

The actual mechanism of the photoluminescence of CDs is still an open issue among researchers. Generally, the emission spectra of CDs are roughly symmetrical on the wavelength scale. The emission peaks of CDs are usually wide, with large Stokes shifts as compared with the emission of organic dyes. The emission peak position is always related to the excitation wavelength, which is known as *wavelength-dependent behaviour*. To rationalize this behaviour many hypothesis have been considered, such as: (1) a wide distribution of differently sized dots, (2) a large variety of surface moieties, (3) different emissive traps (solvation effect), or (4) a mixture of different aromatic species within the carbon core. So far, a unanimous agreement in the scientific community on the emission mechanisms is still lacking.[46-48]

1.3.3 Perovskite Nanoparticles (PNPs)

Hybrid Organic-Inorganic Perovskite: From Bulk to Nanoscale

Perovskites are a class of crystalline materials with the formula ABX_3, in which A and B are cations and X represents the anion. The ideal perovskite has a simple cubic crystal structure consisting of a corner-sharing BX_6 octahedral network with a B–X–B bond

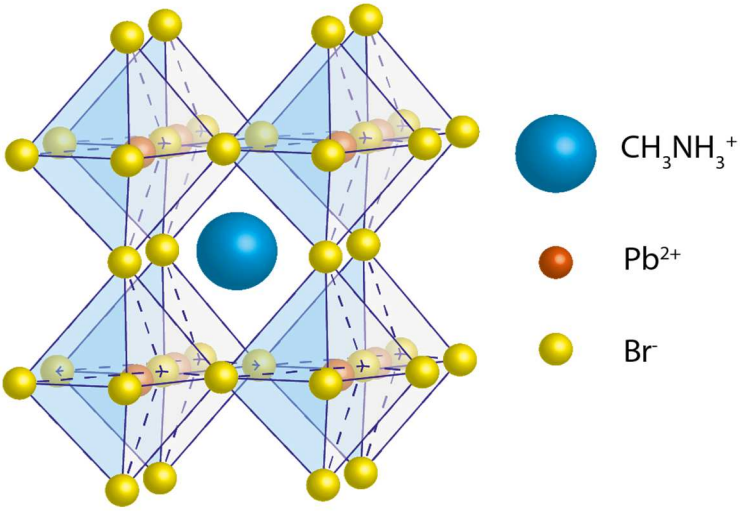

Figure 1.10 Scheme of methyl-ammonium lead bromide ($MAPbBr_3$) perovskite structure.

angle of 180° and A ions in the interstices. In hybrid organic–inorganic perovskites (HOIPs), A is a monovalent organic cation, such as methylammonium (MA or $CH_3NH_3^+$) or formamidinium (FA or $(NH_2)_2CH^+$), B is a divalent metal cation (e.g. lead, tin) and X is a halide anion.[49-51] In Figure 1.10, the structure of the $MAPbBr_3$ perovskite which is used in this thesis is reported.

HOIP perovskites gathered a huge amount of attention in the last years due to the recent breakthroughs in photovoltaic performances achieved using these highly promising materials.[49] Indeed, since the first report on HOIP based solar cells in 2009, the record HOIP solar cell efficiency (certified) has now reached 22%.[52] This represents the highest solar cell efficiency among all solution-processed materials and the fastest rate of efficiency improvement in the history of all photovoltaic materials. In addition, other major advantages of HOIP materials are their low energetic and monetary cost and their composition based on Earth-abundant and available elements. Although the many benefits of perovskite materials, there are still a number of key challenges to be overcome. Indeed, the potential environmental impact of the lead content of the perovskites and the scalability of their production to a useful commercial size are still open points. Moreover, the long-term stability of perovskites needs also to be improved because of perovskites sensitivity to moisture.

Along with the rapid development of bulk perovskites deposited from precursor solutions, the research into colloidal perovskite nanoparticles (NPs) has also emerged

very recently.[53-62] Nano-sized perovskites provide additional means for tailoring electronic and optical properties via the effects of quantum confinement and wave function engineering. A highlight of perovskite NPs is that they exhibit superior photoluminescence properties, making them especially attractive for lighting and display technology. Indeed, the photoluminescent quantum yield (PLQY) of perovskite colloidal solutions could reach 80% for methylammonium lead bromide ($MAPbBr_3$).

SYNTHESIS AND OPTICAL PROPERTIES OF PNPS

Many different methodologies were adopted to synthesize perovskite nanoparticles. Pérez-Prieto and co-workers pioneered the wet chemistry colloidal synthesis of free-standing hybrid perovskite NPs employing a simple one-step approach.[54] A mixture of ammonium bromide with short methyl chain and longer alkyl chains (e.g. octadecyl or octyl) was reacted with $PbBr_2$ in the presence of oleic acid (OA) and octadecene (ODE). In these perovskite NPs, the MA cations are embedded in the central part of the crystal to connect neighbouring $[PbBr_6]^-$ octahedra, while the longer alkyl ammonium cations occupy the outer space, terminating the growth of NPs. Thus, these longer alkyl ammonium cations work as the capping ligands of the NPs, and keep the NPs dispersible in a wide range of organic solvents. The obtained nanoparticles could be stable in concentrated solutions as well as in solid state for several months. From TEM investigation, it was observed that this synthetic procedure usually produces a mixture of nanodots and nanoplatelets which possess different optical properties.[63]

Another convenient and versatile method to produce perovskite nanoparticles is the ligand assisted reprecipitation (LARP) technique.[64] The LARP synthesis is accomplished by simply mixing a solution of perovskite precursors in good solvent (such as DMF) into vigorously stirred poor solvent (toluene) with long chain organic ligands. This procedure results in the controlled crystallization of precursors into colloidal nanoparticles.

Nanometer miniaturization of perovskite strongly increases photoluminescence quantum yield due to the increased binding energy related to the size reduction as well as proper chemical passivation of the bromine-rich surface. In addition, due to the quantum confinement effect, the emission wavelength of perovskite NPs is blue shifted compared to bulk. Analogously to semiconductor QDs, by varying a large variety of

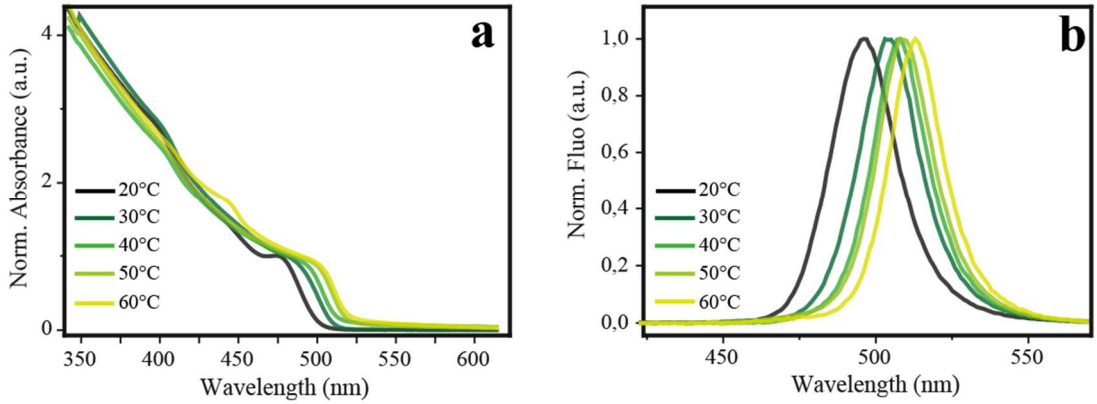

Figure 1.11 (a) Absorption and (b) PL spectra for a series of perovskite NPs synthesized at different temperatures, in toluene dispersion, by LARP technique.

synthetic conditions, such as the solvent, the temperature, the ligands and the precursors, it is possible to tune the optical properties of perovskite NPs in a continuous way. An example of the easy tunability of optical properties of perovskite NPs is shown in Figure 1.11. The absorption and PL spectra for a series of perovskite NPs synthetized at different temperatures by LARP technique show a red shift of both the absorption edge and the emission band at increasing temperatures of synthesis. Higher temperatures of synthesis, indeed, favour a larger dimension of perovskite NPs. A larger nanoparticle dimension results in a lower exciton confinement effect and therefore a red-shift of both the absorption and PL spectra. The facile tunability of perovskite NPs properties provided opportunities for white-light emission and therefore for their application in highly efficient LEDs.[65,66]

1.4 BIBLIOGRAPHY

(1) Luque, A.; Hegedus, S.: Handbook of Photovoltaic Science and Engineering; Wiley, 2011.

(2) Green, M. A.: Third Generation Photovoltaics: Advanced Solar Energy Conversion; Springer, 2003.

(3) Conibeer, G. Third-generation photovoltaics. *Mater. Today* **2007**, 10, 42-50.

(4) Leo, K. Elementary Processes in Organic Photovoltaics, Springer, 2017.

(5) Hoppe, H.; Sariciftci, N. S. Organic solar cells: An overview. *J. Mater. Res.* **2011**, 19, 1924-1945.

(6) Tang, C. W. Two-layer organic photovoltaic cell. *Appl. Phys. Lett.* **1986**, 48, 183-185.

(7) Yu, G.; Gao, J.; Hummelen, J. C.; Wudl, F.; Heeger, A. J. Polymer Photovoltaic Cells: Enhanced Efficiencies via a Network of Internal Donor-Acceptor Heterojunctions. *Science* **1995**, 270, 1789.

(8) He, Z.; Zhong, C.; Su, S.; Xu, M.; Wu, H.; Cao, Y. Enhanced power-conversion efficiency in polymer solar cells using an inverted device structure. *Nat Photon* **2012**, 6, 591-595.

(9) Huang, F.; Yip, H. L.; Cao, Y.: Polymer Photovoltaics: Materials, Physics, and Device Engineering; Royal Society of Chemistry, 2015.

(10) Müllen, K.; Pisula, W. Donor–Acceptor Polymers. *J. Am. Chem. Soc.* **2015**, 137, 9503-9505.

(11) Lai, Y.-Y.; Cheng, Y.-J.; Hsu, C.-S. Applications of functional fullerene materials in polymer solar cells. *Energy Environ Sci.* **2014**, 7, 1866-1883.

(12) Castañer, L.; Silvestre, S. Modelling Photovoltaic Systems Using PSpice®; John Wiley & Sons, 2006.

(13) Lanzani, G.: The Photophysics behind Photovoltaics and Photonics; Wiley, 2012.

(14) Lanzani, G.: Photophysics of Molecular Materials: From Single Molecules to Single Crystals; Wiley, 2006.

(15) Marian, C. M. Spin–orbit coupling and intersystem crossing in molecules. Wiley *Interdiscip Rev Comput Mol Sci.* **2012**, 2, 187-203.

(16) Gregg, B. A. Excitonic Solar Cells. *J. Phys. Chem. B* **2003**, 107, 4688-4698.

(17) Bakulin, A. A.; Dimitrov, S. D.; Rao, A.; Chow, P. C. Y.; Nielsen, C. B.; Schroeder, B. C.; McCulloch, I.; Bakker, H. J.; Durrant, J. R.; Friend, R. H. Charge-Transfer State Dynamics Following Hole and Electron Transfer in Organic Photovoltaic Devices. *JPCL* **2013**, 4, 209-215.

(18) Deibel, C.; Strobel, T.; Dyakonov, V. Role of the Charge Transfer State in Organic Donor–Acceptor Solar Cells. *Adv. Mater.* **2010**, 22, 4097-4111.

(19) Laquai, F.; Andrienko, D.; Deibel, C.; Neher, D.: Charge Carrier Generation, Recombination, and Extraction in Polymer–Fullerene Bulk Heterojunction Organic Solar Cells. In *Elementary Processes in Organic Photovoltaics*; Springer, 2017; pp 267-291.

(20) Borchert, H.: Solar Cells Based on Colloidal Nanocrystals; Springer, 2014.

(21) Zhou, Y.; Eck, M.; Kruger, M. Bulk-heterojunction hybrid solar cells based on colloidal nanocrystals and conjugated polymers. *Energy Environ Sci.* **2010**, 3, 1851-1864.

(22) Merhari, L.: Hybrid Nanocomposites for Nanotechnology: Electronic, Optical, Magnetic and Biomedical Applications; Springer US, 2009.

(23) Zutz, F.; Lokteva, I.; Radychev, N.; Kolny-Olesiak, J.; Riedel, I.; Borchert, H.; Parisi, J. Study of the influence of the Cd:Se precursor ratio during the synthesis of CdSe nanocrystals on the performance of CdSe/P3HT hybrid solar cells. *Phys. Status Solidi A* **2009**, 206, 2700-2708.

(24) Brandenburg, J. E.; Jin, X.; Kruszynska, M.; Ohland, J.; Kolny-Olesiak, J.; Riedel, I.; Borchert, H.; Parisi, J. Influence of particle size in hybrid solar cells composed of CdSe nanocrystals and poly(3-hexylthiophene). *J. Appl. Phys.* **2011**, 110, 064509.

(25) Bansal, N.; Reynolds, L. X.; MacLachlan, A.; Lutz, T.; Ashraf, R. S.; Zhang, W.; Nielsen, C. B.; McCulloch, I.; Rebois, D. G.; Kirchartz, T.; Hill, M. S.; Molloy, K. C.; Nelson, J.; Haque, S. A. Influence of Crystallinity and Energetics on Charge Separation in Polymer–Inorganic Nanocomposite Films for Solar Cells. *Sci. Rep.* **2013**, 3, 1531.

(26) Huynh, W. U.; Dittmer, J. J.; Alivisatos, A. P. Hybrid Nanorod-Polymer Solar Cells. *Science* **2002**, 295, 2425.

(27) Lefrançois, A.; Luszczynska, B.; Pepin-Donat, B.; Lombard, C.; Bouthinon, B.; Verilhac, J.-M.; Gromova, M.; Faure-Vincent, J.; Pouget, S.; Chandezon, F.; Sadki, S.; Reiss, P. Enhanced Charge Separation in Ternary P3HT/PCBM/CuInS2 Nanocrystals Hybrid Solar Cells. *Sci. Rep.* **2015**, 5, 7768.

(28) Ashcroft, N. W.; Mermin, N. D.: Solid State Physics; Holt, Rinehart and Winston, 1976.

(29) Scholes, G. D.; Rumbles, G. Excitons in nanoscale systems. *Nat. Mater.* **2006**, 5, 683-696.

(30) Brus, L. E. Electron–electron and electron-hole interactions in small semiconductor crystallites: The size dependence of the lowest excited electronic state. *J. Chem. Phys.* **1984**, 80, 4403-4409.

(31) Smith, A. M.; Mohs, A. M.; Nie, S. Tuning the optical and electronic properties of colloidal nanocrystals by lattice strain. *Nat Nano* **2009**, 4, 56-63.

(32) Park, K.; Deutsch, Z.; Li, J. J.; Oron, D.; Weiss, S. Single Molecule Quantum-Confined Stark Effect Measurements of Semiconductor Nanoparticles at Room Temperature. *ACS Nano* **2012**, 6, 10013-10023.

(33) Jones, M.; Lo, S. S.; Scholes, G. D. Quantitative modeling of the role of surface traps in CdSe/CdS/ZnS nanocrystal photoluminescence decay dynamics. *Proc. Natl. Acad. Sci.* **2009**, 106, 3011-3016.

(34) Wuister, S. F.; de Mello Donegá, C.; Meijerink, A. Influence of Thiol Capping on the Exciton Luminescence and Decay Kinetics of CdTe and CdSe Quantum Dots. *J. Phys. Chem. B* **2004**, 108, 17393-17397.

(35) Peterson, M. D.; Cass, L. C.; Harris, R. D.; Edme, K.; Sung, K.; Weiss, E. A. The Role of Ligands in Determining the Exciton Relaxation Dynamics in Semiconductor Quantum Dots. *Annu. Rev. Phys. Chem.* **2014**, 65, 317-339.

(36) Boles, M. A.; Ling, D.; Hyeon, T.; Talapin, D. V. The surface science of nanocrystals. *Nat Mater* **2016**, 15, 141-153.

(37) Green, M. The nature of quantum dot capping ligands. *J. Mater. Chem.* **2010**, 20, 5797-5809.

(38) Lim, S. Y.; Shen, W.; Gao, Z. Carbon quantum dots and their applications. *Chem. Soc. Rev.* **2015**, 44, 362-381.

(39) Li, H.; Kang, Z.; Liu, Y.; Lee, S.-T. Carbon nanodots: synthesis, properties and applications. *J. Mater. Chem.* **2012**, 22, 24230-24253.

(40) Wang, Y.; Hu, A. Carbon quantum dots: synthesis, properties and applications. *J. Mater. Chem. C* **2014**, 2, 6921-6939.

(41) Mosconi, D.; Mazzier, D.; Silvestrini, S.; Privitera, A.; Marega, C.; Franco, L.; Moretto, A. Synthesis and Photochemical Applications of Processable Polymers Enclosing Photoluminescent Carbon Quantum Dots. *ACS Nano* **2015**, 9, 4156-4164.

(42) Yin, J.-Y.; Liu, H.-J.; Jiang, S.; Chen, Y.; Yao, Y. Hyperbranched Polymer Functionalized Carbon Dots with Multistimuli-Responsive Property. *ACS Macro Lett.* **2013**, 2, 1033-1037.

(43) Zhao, H. X.; Liu, L. Q.; Liu, Z. D.; Wang, Y.; Zhao, X. J.; Huang, C. Z. Highly selective detection of phosphate in very complicated matrixes with an off-on fluorescent probe of europium-adjusted carbon dots. *Chem. Commun.* **2011**, 47, 2604-2606.

(44) Li, H.; Zhang, Y.; Wang, L.; Tian, J.; Sun, X. Nucleic acid detection using carbon nanoparticles as a fluorescent sensing platform. *Chem. Commun.* **2011**, 47, 961-963.

(45) Wang, F.; Xie, Z.; Zhang, H.; Liu, C.-y.; Zhang, Y.-g. Highly Luminescent Organosilane-Functionalized Carbon Dots. *Adv. Funct. Mater.* **2011**, 21, 1027-1031.

(46) Zhu, S.; Song, Y.; Zhao, X.; Shao, J.; Zhang, J.; Yang, B. The photoluminescence mechanism in carbon dots (graphene quantum dots, carbon nanodots, and polymer dots): current state and future perspective. *Nano Res.* **2015**, 8, 355-381.

(47) Righetto, M.; Privitera, A.; Fortunati, I.; Mosconi, D.; Zerbetto, M.; Curri, M. L.; Corricelli, M.; Moretto, A.; Agnoli, S.; Franco, L.; Bozio, R.; Ferrante, C. Spectroscopic Insights into Carbon Dot Systems. *JPCL* **2017**, 8, 2236-2242.

(48) Fu, M.; Ehrat, F.; Wang, Y.; Milowska, K. Z.; Reckmeier, C.; Rogach, A. L.; Stolarczyk, J. K.; Urban, A. S.; Feldmann, J. Carbon Dots: A Unique Fluorescent Cocktail of Polycyclic Aromatic Hydrocarbons. *Nano Lett.* **2015**, 15, 6030-6035.

(49) Brenner, T. M.; Egger, D. A.; Kronik, L.; Hodes, G.; Cahen, D. Hybrid organic—inorganic perovskites: low-cost semiconductors with intriguing charge-transport properties. *Nat Rev Mater* **2016**, 1, 15007.

(50) Gonzalez-Carrero, S.; Galian, R. E.; Pérez-Prieto, J. Organic-inorganic and all-inorganic lead halide nanoparticles [Invited]. *Opt. Express* **2016**, 24, A285-A301.

(51) González-Carrero, S.; Galian, R. E.; Pérez-Prieto, J. Organometal Halide Perovskites: Bulk Low-Dimension Materials and Nanoparticles. *Part. Part. Syst. Charact.* **2015**, 32, 709-720.

(52) Yang, W. S.; Park, B.-W.; Jung, E. H.; Jeon, N. J.; Kim, Y. C.; Lee, D. U.; Shin, S. S.; Seo, J.; Kim, E. K.; Noh, J. H.; Seok, S. I. Iodide management in formamidinium-lead-halide–based perovskite layers for efficient solar cells. *Science* **2017**, 356, 1376.

(53) Sichert, J. A.; Tong, Y.; Mutz, N.; Vollmer, M.; Fischer, S.; Milowska, K. Z.; García Cortadella, R.; Nickel, B.; Cardenas-Daw, C.; Stolarczyk, J. K.; Urban, A. S.;

Feldmann, J. Quantum Size Effect in Organometal Halide Perovskite Nanoplatelets. *Nano Lett.* **2015**, 15, 6521-6527.

(54) Schmidt, L. C.; Pertegás, A.; González-Carrero, S.; Malinkiewicz, O.; Agouram, S.; Mínguez Espallargas, G.; Bolink, H. J.; Galian, R. E.; Pérez-Prieto, J. Nontemplate Synthesis of $CH_3NH_3PbBr_3$ Perovskite Nanoparticles. *J. Am. Chem. Soc.* **2014**, 136, 850-853.

(55) Mittal, M.; Jana, A.; Sarkar, S.; Mahadevan, P.; Sapra, S. Size of the Organic Cation Tunes the Band Gap of Colloidal Organolead Bromide Perovskite Nanocrystals. *JPCL* **2016**, 7, 3270-3277.

(56) Ahmed, G. H.; Liu, J.; Parida, M. R.; Murali, B.; Bose, R.; AlYami, N. M.; Hedhili, M. N.; Peng, W.; Pan, J.; Besong, T. M. D.; Bakr, O. M.; Mohammed, O. F. Shape-Tunable Charge Carrier Dynamics at the Interfaces between Perovskite Nanocrystals and Molecular Acceptors. *JPCL* **2016**, 7, 3913-3919.

(57) Luo, B.; Pu, Y.-C.; Yang, Y.; Lindley, S. A.; Abdelmageed, G.; Ashry, H.; Li, Y.; Li, X.; Zhang, J. Z. Synthesis, Optical Properties, and Exciton Dynamics of Organolead Bromide Perovskite Nanocrystals. *J. Phys. Chem. C* **2015**, 119, 26672-26682.

(58) Gonzalez-Carrero, S.; Galian, R. E.; Perez-Prieto, J. Maximizing the emissive properties of $CH_3NH_3PbBr_3$ perovskite nanoparticles. *J. Mater. Chem. A* **2015**, 3, 9187-9193.

(59) Martinez-Sarti, L.; Koh, T. M.; La-Placa, M.-G.; Boix, P. P.; Sessolo, M.; Mhaisalkar, S. G.; Bolink, H. J. Efficient photoluminescent thin films consisting of anchored hybrid perovskite nanoparticles. *Chem. Commun.* **2016**, 52, 11351-11354.

(60) Luo, B.; Pu, Y.-C.; Lindley, S. A.; Yang, Y.; Lu, L.; Li, Y.; Li, X.; Zhang, J. Z. Organolead Halide Perovskite Nanocrystals: Branched Capping Ligands Control Crystal Size and Stability. *Angew. Chem. Int. Ed.* **2016**, 55, 8864-8868.

(61) Muthu, C.; Agarwal, S.; Vijayan, A.; Hazra, P.; Jinesh, K. B.; Nair, V. C. Hybrid Perovskite Nanoparticles for High-Performance Resistive Random Access Memory Devices: Control of Operational Parameters through Chloride Doping. *Adv. Mater. Interfaces* **2016**, 3, 1600092.

(62) Weidman, M. C.; Seitz, M.; Stranks, S. D.; Tisdale, W. A. Highly Tunable Colloidal Perovskite Nanoplatelets through Variable Cation, Metal, and Halide Composition. *ACS Nano* **2016**, 10, 7830-7839.

(63) Tyagi, P.; Arveson, S. M.; Tisdale, W. A. Colloidal Organohalide Perovskite Nanoplatelets Exhibiting Quantum Confinement. *JPCL* **2015**, 6, 1911-1916.

(64) Zhang, F.; Zhong, H.; Chen, C.; Wu, X.-g.; Hu, X.; Huang, H.; Han, J.; Zou, B.; Dong, Y. Brightly Luminescent and Color-Tunable Colloidal CH3NH3PbX3 (X = Br, I, Cl) Quantum Dots: Potential Alternatives for Display Technology. *ACS Nano* **2015**, 9, 4533-4542.

(65) Zhang, X.; Liu, H.; Wang, W.; Zhang, J.; Xu, B.; Karen, K. L.; Zheng, Y.; Liu, S.; Chen, S.; Wang, K.; Sun, X. W. Hybrid Perovskite Light-Emitting Diodes Based on Perovskite Nanocrystals with Organic–Inorganic Mixed Cations. *Adv. Mater.* **2017**, 29, 1606405.

(66) Kim, Y.-H.; Wolf, C.; Kim, Y.-T.; Cho, H.; Kwon, W.; Do, S.; Sadhanala, A.; Park, C. G.; Rhee, S.-W.; Im, S. H.; Friend, R. H.; Lee, T.-W. Highly Efficient Light-Emitting Diodes of Colloidal Metal–Halide Perovskite Nanocrystals beyond Quantum Size. *ACS Nano* **2017**, 11, 6586-6593.

CHAPTER 2.
ELECTRON PARAMAGNETIC RESONANCE

EPR spectroscopy, which is sometimes referred to as electron spin resonance (ESR), is a spectroscopic technique based on the physical properties of the electron spin. Therefore, it is particularly useful for the investigation of paramagnetic species. A large variety of information can be obtained by EPR spectroscopy, such as structural and dynamical properties of the paramagnetic species and their interaction with the surrounding environment.

In this chapter, an overview is presented on the theoretical background and on the experimental details of electron paramagnetic resonance (EPR) spectroscopy. In particular, in sections 2.1 and 2.2, the Zeeman and the electron-electron interactions are described, respectively. These interactions are fundamental to understand all the spectra reported in this thesis. In section 2.3, 2.4 and 2.5, the main concepts useful to understand the time-resolved EPR spectra are outlined. In particular, the theory of the paramagnetic triplet state, of the electron spin polarization and of the spin-correlated radical pairs is explained. In section 2.6, the main line broadening mechanisms are listed and in section 2.7, the description of the time evolution of spin systems, which is the basis for the understanding of pulsed EPR spectra, is given. Finally, in section 2.8 and 2.9, the description of the EPR experiments performed in this thesis (steady state, time resolved and pulsed EPR) is illustrated and the experimental details are reported.

The chapter follows the description of the classical textbooks on the basic principles of EPR spectroscopy,[1-3] on the description of triplet states and SCRP,[4-6] and on some recent papers on the application of EPR to organic photovoltaics.[7-9] For the description of pulsed EPR and spin dynamics the main reference is the book of Schweiger.[10] Finally, for the description of EPR instrumental details the main classical source is the book of Poole.[11]

2.1 ZEEMAN INTERACTION

The origin of EPR spectroscopy is the Zeeman effect which is the result of the interaction between the magnetic moment of a paramagnetic species and the externally applied magnetic field.

The simplest system to be studied with EPR is a spin-1/2 particle: e.g. a free electron. The spin Hamiltonian for this system in an external magnetic field is given by:

$$\hat{H}_{Zeeman} = -\hat{\boldsymbol{\mu}}\mathbf{B_0} \tag{1}$$

where $\hat{\boldsymbol{\mu}}$ is the operator of the magnetic moment and $\mathbf{B_0}$ is the external magnetic field. For a free electron, the magnetic moment operator is related to the operator of spin angular momentum by the following relationship:

$$\hat{\boldsymbol{\mu}} = -\frac{g_e \mu_B}{\hbar}\hat{\boldsymbol{S}} \tag{2}$$

Here, g_e is the electron g-factor or Landé factor, μ_B the Bohr magneton and $\hat{\boldsymbol{S}}$ the spin operator vector. The eigenstates of this system are spin up ($|\alpha\rangle$, m_s=+1/2) and down ($|\beta\rangle$, m_s=-1/2) states, which are quantized along the direction of the magnetic field. Their respective eigenenergies are:

$$\begin{aligned} E_\alpha &= +\frac{1}{2} g_e \mu_B B_0 \\ E_\beta &= -\frac{1}{2} g_e \mu_B B_0 \end{aligned} \tag{3}$$

The resonance condition is fulfilled when the energy difference of spin up and down states is equal to the energy of photons with frequency ν. Under the condition (transition selection rule) $\Delta m_s = \pm 1$, the resonance frequency for EPR is therefore:

$$\Delta E = g_e \mu_B B_0 = h\nu \quad (4)$$

For a free electron, the g-value is a dimensionless quantity whose value is g=2.0023. In solid state, however, the g-factor deviates from this value due to the combined effect of the presence of other electrons and of the coupling of the electron spin with the electron orbital angular momentum. The spin-orbit coupling is the origin of the anisotropy of the Zeeman interaction. Therefore, in general, the g-factor must be described by a second-order tensor that represents the dependence of the Zeeman interaction on the orientation of the molecules with respect to the magnetic field. The symmetric g-tensor can always be diagonalized by proper choice of the reference axes and is fully defined by the three diagonal elements when the tensor is calculated in the principal axis system:

$$\boldsymbol{g} = \begin{pmatrix} g_{xx} & 0 & 0 \\ 0 & g_{yy} & 0 \\ 0 & 0 & g_{zz} \end{pmatrix} \quad (5)$$

In general, the Zeeman interaction can be expressed by the following spin Hamiltonian:

$$\hat{H}_{Zeeman} = \mu_B \mathbf{B_0} \bar{\bar{\boldsymbol{g}}} \hat{\boldsymbol{S}} \quad (6)$$

For frozen solutions, amorphous solids and crystal powders, the molecular orientations within the sample are randomly distributed. Therefore, the EPR spectrum is the result of all the molecular orientations, a so-called *powder spectrum.* Conversely, for paramagnetic species in non-viscous solutions, fast molecular tumbling leads to an averaging of the g-factor components. Only a single isotropic line is observed at the spectral position of the averaged g -factor $g_{iso} = \frac{1}{3}(g_{xx} + g_{yy} + g_{zz})$.

In Figure 2.1.a the Zeeman splitting, proportional to the magnetic field strength, for a system with spin-1/2 is reported. Resonant photons in EPR spectroscopy usually belong to the microwave spectral range. From the experimental point of view, EPR spectroscopy is based on sweeping the magnetic field B_0 and continuously irradiating the sample with a monochromatic microwave radiation (MW) until the resonance condition is satisfied. Because of the particular detection scheme (magnetic field modulation and phase-sensitive lock-in amplification) the EPR spectrum is detected as the first-derivative of the MW absorption. In Figure 2.1.b, an example of powder and solution spectra is reported.

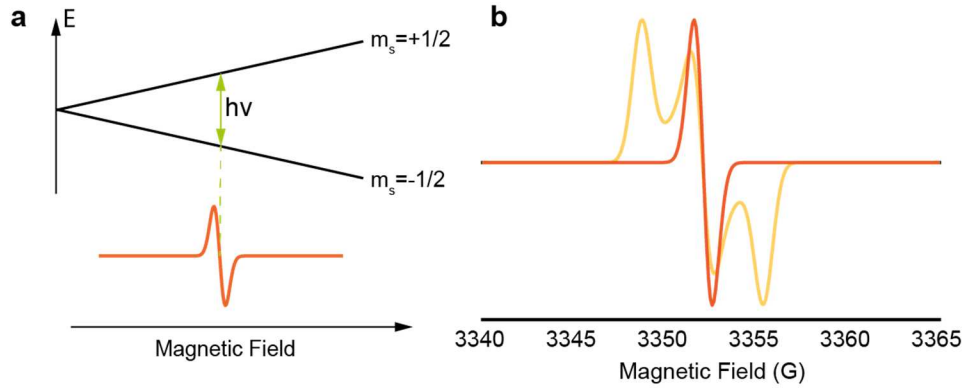

Figure 2.1 (a) Energy level diagram for a S=1/2 paramagnetic species as a function of the applied magnetic field and first-derivative EPR spectrum in correspondence of the resonance field. (b) Powder EPR spectrum (orange line) and averaged EPR spectrum (red line) for a paramagnetic species.

2.2 ELECTRON-ELECTRON INTERACTION

When two unpaired spins (with spin S_1 and S_2) are sufficiently close, two additional interactions must be considered: exchange and magnetic dipolar interaction. The spin Hamiltonian for a system of two interacting spins can be expressed in the following form:

$$\hat{H}_{ee} = -2J\hat{\boldsymbol{S}}_{\boldsymbol{1}}\hat{\boldsymbol{S}}_{\boldsymbol{2}} + 2\hat{\boldsymbol{S}}_{\boldsymbol{1}}\bar{\bar{\boldsymbol{D}}}\hat{\boldsymbol{S}}_{\boldsymbol{2}} \qquad (7)$$

where the first term is the isotropic exchange interaction term, and the second one is the anisotropic dipole-dipole interaction term. In the following, these two contributions are described.

2.2.1 THE EXCHANGE INTERACTION

The exchange interaction is a quantum mechanical effect that only occurs between identical particles, such as two electrons. The effect is due to exchange symmetry of the wavefunction of indistinguishable particles. When two indistinguishable particles are exchanged their wavefunction can either remain unchanged (symmetric, for bosons) or change its sign (antisymmetric, for fermions). For fermions, such as electrons, exchange interaction is related to *Pauli exclusion principle* and accounts for the energetic separation between the singlet and triplet states of two coupled electron spins.

Two non-interacting electrons can be described by the product of the eigenstates of the single electrons ($|\alpha_1\alpha_2\rangle, |\alpha_1\beta_2\rangle, |\beta_1\alpha_2\rangle|\beta_1\beta_2\rangle$), i.e. the *uncoupled basis*. Applying the

exchange Hamiltonian to this basis, the representative matrix is not diagonal. Diagonalizing the exchange Hamiltonian, the following eigenstates are obtained (*coupled basis*):

$$\begin{aligned} |T_{+1}\rangle &= |\alpha_1\alpha_2\rangle \\ |T_0\rangle &= \frac{1}{\sqrt{2}}|\alpha_1\beta_2 + \beta_1\alpha_2\rangle \\ |T_{-1}\rangle &= |\beta_1\beta_2\rangle \\ |S\rangle &= \frac{1}{\sqrt{2}}|\alpha_1\beta_2 - \beta_1\alpha_2\rangle \end{aligned} \tag{12}$$

The first three states are triplet states (S=1) and they are symmetric under the exchange of the electrons, while the last state is a singlet state (S=0) and it is antisymmetric under the exchange operation. In the coupled basis, the energies of the triplet state and of the singlet state are $E_T = -\frac{1}{2}J$ and $E_S = +\frac{3}{2}J$ respectively. The exchange interaction parameter J is usually assumed to fall off exponentially with the distance r between the two electron spins:

$$J(r) = J_0 e^{-\beta r} \tag{8}$$

Where J_0 can be positive as well as negative: reported values lie in the range of $1.4 \cdot 10^{10}$ mT < $|J_0|$ < $8 \cdot 10^{10}$ mT.[12] The value for β is in the range between 14 – 18 nm^{-1}.[12] The exchange coupling interaction is negligible for distances between the two electrons larger than ≈ 1,5 nm.

2.2.2 THE DIPOLE-DIPOLE INTERACTION

The magnetic dipole-dipole interaction term results from the interaction between the magnetic moments of the neighbouring spins. In particular, spin 1 is subjected to a shift of its local magnetic field due to the magnetic moment of spin 2 and vice versa. The dipolar interaction is independent from the applied external magnetic field and it accounts for the absence of degeneracy of the sublevels in a S=1 species (triplet state) in the absence of magnetic field. For this reason, dipole-dipole interaction term is also called zero-field splitting (ZFS). ZFS is an anisotropic term and is described by a second rank tensor:

$$\hat{H}_{dip} = 2\hat{\boldsymbol{S}}_{\boldsymbol{1}}\bar{\bar{\boldsymbol{D}}}\hat{\boldsymbol{S}}_{\boldsymbol{2}}$$

$$\bar{\bar{\boldsymbol{D}}} = \begin{pmatrix} D_{xx} & 0 & 0 \\ 0 & D_{yy} & 0 \\ 0 & 0 & D_{zz} \end{pmatrix} = \begin{pmatrix} \frac{1}{3}D - E & 0 & 0 \\ 0 & \frac{1}{3}D + E & 0 \\ 0 & 0 & -\frac{2}{3}D \end{pmatrix} \quad (9)$$

The D tensor is traceless (the sum of all diagonal elements is zero) and symmetric. It is fully described by the two scalar parameters D and E, also called ZFS parameters:

$$D = \frac{3}{2}D_{zz}$$
$$E = \frac{1}{2}(D_{xx} - D_{yy}) \quad (10)$$

The D parameter is related to the average interaction between the two unpaired electrons, and therefore to their mean distance. In detail, D is proportional to $\langle r^{-3} \rangle$, where the angular brackets indicate that the distance *r* between the two unpaired electrons must be averaged over the electronic spatial wavefunction. The E parameter describes the off-axial interaction strength for systems with symmetry lower than axial.

2.2.3 Comparison between J and D

The exchange parameter J and the dipolar coupling parameter D are energy values, but they are usually handled in frequency (J/h, D/h) or magnetic field units (J', D'). The relation between the two is:

$$\frac{J}{h}[MHz] = \frac{g\mu_b}{h}J'[mT]$$
$$\frac{D}{h}[MHz] = \frac{g\mu_b}{h}D'[mT] \quad (11)$$

Figure 2.2 shows a graphical representation of the strength of exchange and dipolar coupling in magnetic field units. The dipolar coupling D'(r) usually has the longer range and dominates the exchange interaction J'(r), except at very small inter-spin separations. D'(r) becomes negligible for separations larger than 3–4 nm, which means free, non-interacting spins. The relative strength between D' and J' can be separated into three

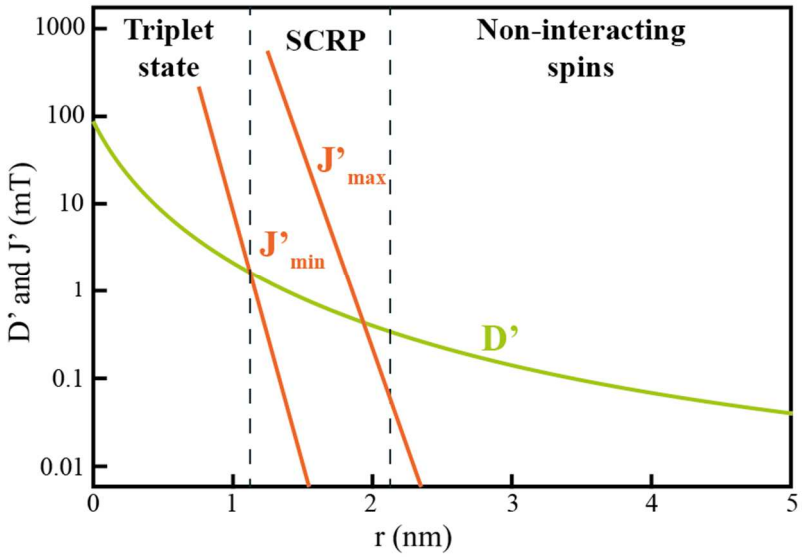

Figure 2.2 Representation of dipolar and exchange interaction as a function of inter-radical distance r. Three different regimes are separated by dashed boundary lines: triplet states, spin correlated radical pairs and non-interacting spins.

regimes of interaction. In the strong coupling regime, the unpaired electrons are coupled and a pure triplet state can be observed with EPR spectroscopy. For intermediate coupling, the system can be described as spin correlated radical pair (SCRP), with a complex dependence of the spectrum on the specific parameter set. In the weak coupling regime, the parameters D' and J' are negligible and can be considered non-interacting. The boundary lines plotted in Figure 2.2 are only representative and may change in different systems.

While the case of non-interacting spins is well described by the Zeeman interaction Hamiltonian (section 2.1), the triplet state and the SCRP need a further discussion. In the following the two different systems are described.

2.3 THE TRIPLET STATE

As previously discussed, the triplet state is defined by the following three spin wavefunctions corresponding to the three allowed projections of the total spin (S=1) onto the z-axis:

$$|T_{+1}\rangle = |\alpha_1\alpha_2\rangle$$
$$|T_0\rangle = \frac{1}{\sqrt{2}}|\alpha_1\beta_2 + \beta_1\alpha_2\rangle \qquad (12)$$

$$|T_{-1}\rangle = |\beta_1\beta_2\rangle$$

In the zero-field case, the spin Hamiltonian that describes the triplet state includes only the dipole-dipole interaction term previously discussed. In this case, a proper linear combination of the triplet spin wavefunctions must be considered to describe the eigenstates of this spin Hamiltonian:

$$\begin{aligned} |T_x\rangle &= \frac{1}{\sqrt{2}}|T_{-1} - T_{+1}\rangle \\ |T_y\rangle &= \frac{i}{\sqrt{2}}|T_{-1} + T_{+1}\rangle \\ |T_z\rangle &= |T_0\rangle \end{aligned} \tag{13}$$

Applying the spin Hamiltonian to these wavefunctions the following eigenvalues can be obtained:

$$\begin{aligned} E_x &= \frac{1}{3}D - E \\ E_y &= \frac{1}{3}D + E \\ E_z &= -\frac{2}{3}D \end{aligned} \tag{14}$$

where the D and E parameters are the ZFS parameters previously described. When an external magnetic field B_0 is applied, a special direction in space is introduced. In the following a magnetic field B_0 along a z-axis is considered, where z is also one of the dipolar tensor principal axes; the other two possibilities in which the external magnetic field is aligned with the x and y axis can be readily derived by permutation. With the external magnetic field aligned along the z direction, $|T_z\rangle$ is still an eigenstate, while $|T_z\rangle$ and $|T_z\rangle$ are mixed together according the following relationship:

$$\begin{aligned} |\sigma_x\rangle &= cos\theta|T_{+1}\rangle - sin\theta|T_{-1}\rangle \\ |\sigma_y\rangle &= sin\theta|T_{+1}\rangle + cos\theta|T_{-1}\rangle \\ |\sigma_z\rangle &= |T_z\rangle = |T_0\rangle \end{aligned} \tag{15}$$

Where the mixing angle θ is defined as $\theta = \frac{1}{2}\tan^{-1}[E_x - E_y/2g\mu_B B_0]$.

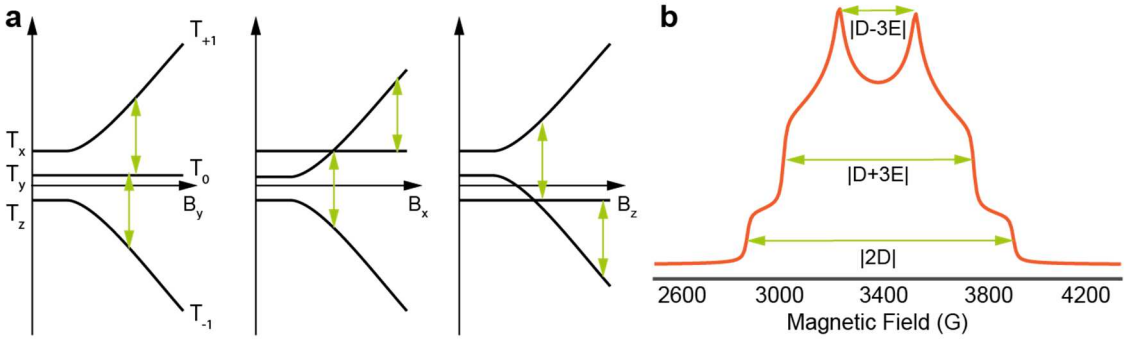

Figure 2.3 (a) Energy level diagram as a function of the applied magnetic field for a triplet state characterized by D > 0 and E < 0. Transitions labelled by arrows correspond to Δms=±1. (b) Example of a powder absorption EPR spectrum for a triplet state.

Appling the spin Hamiltonian including the Zeeman and dipolar interaction terms to these eigenstates, the following eigenenergies of the three triplet sublevels are obtained:

$$U_x = \frac{1}{2}(E_x + E_y) + \frac{1}{2}(E_x - E_y)tan\theta + g\mu_B B_0$$

$$U_y = \frac{1}{2}(E_x + E_y) - \frac{1}{2}(E_x - E_y)tan\theta - g\mu_B B_0 \qquad (16)$$

$$U_z = -\frac{2}{3}D$$

Eigenstates and corresponding energies can readily be obtained when the external magnetic field is aligned along the x and y directions considering the same procedure illustrated above. In Figure 2.3.a, the dependence of the energy levels on the strength of the external field at different magnetic field orientations is reported. In Figure 2.3.b, instead, a typical powder EPR absorption lineshape of a triplet state is depicted. Notably from the spectrum it is possible to obtain the D and E parameters that allow to get information on the triplet state wavefunction.

2.4 Spin Polarization

2.4.1 Thermal equilibrium

In a magnetic field, spins are aligned along quantized orientations according to their spin quantum numbers. For a spin-1/2 species, the population ratio of the two spin sublevels α and β is described by the Boltzmann distribution:

$$\frac{N_\beta}{N_\alpha} = \exp\left(-\frac{\Delta E_{Zeeman}}{k_B T}\right) \quad (17)$$

where N_α and N_β are the numbers of spins in the two spin states. At ordinary magnetic fields B_0 the energy splitting between two orientations spin up and spin down is much smaller than the thermal energy $k_B T$.

In case of photogenerated excited triplet states, the spin sublevel populations are generated in a ratio different from thermal equilibrium. In this case *spin polarization*, i.e. a deviation from the thermal population distribution, can be observed, which induces an anomalous EPR lineshape. The main cause of spin polarization is related to the Intersystem Crossing (ISC) mechanism that is described in the following.

2.4.2 Intersystem Crossing Polarization

Usually molecules possess a singlet electronic ground state: electronic levels are well separated in energy and electrons are coupled with opposite spins according to the Pauli's exclusion principle. Due to the spin angular momentum selection rules, during an electromagnetic-induced electronic transition a change in the total spin of the system is forbidden. Then, a singlet ground state can be excited only to a singlet excited state. In presence of spin-orbit interaction, however, this spin selection rule is no longer strictly valid and an intersystem crossing (ISC) process from the excited singlet state to a long-living excited triplet state can occur. Since the intersystem crossing process is characterized by a strong anisotropy of the populating rates of the three spin sublevels ($|T_x\rangle, |T_y\rangle, |T_z\rangle$), a deviation from the Boltzmann population can be observed in photoexcited triplet states. The reason of the spin-selectivity of the ISC mechanism is related to the different values of the spin orbit matrix elements ($\langle S_1|\hat{H}_{SO}|T_x\rangle, \langle S_1|\hat{H}_{SO}|T_y\rangle$ and $\langle S_1|\hat{H}_{SO}|T_z\rangle$) where $\hat{H}_{SO} = -\lambda\hat{\boldsymbol{L}}\hat{\boldsymbol{S}}$.

2.4.3 Radical Pair Recombination Polarization

Some other population paths for an excited triplet state are possible. Among these the radical pair recombination mechanism is of particular interest. As explained in Chapter 1, the primary absorption process in a molecule or a material, produces a singlet excited state. In presence of suitable electron donor or acceptor, the excited state can undergo electron transfer, giving rise to a pair of bound ion radicals. This pair of bound radicals

(CT state) can recombine to a lower-lying triplet states through a spin-selective process. This mechanism generates a completely different spin-polarization pattern compared to ISC process and, for example, an excess population on $|T_{+1}\rangle$ and $|T_{-1}\rangle$ states is generated. This can be rationalized in the frame of SCRP model. As section 2.5 describes in detail, two weakly interacting unpaired electrons can exist in four spin states. The standard recombination pathway starts from the radical ion pair in singlet state, which decays to the singlet ground state by a spin-allowed back-electron transfer. The singlet state recombination eliminates all the pairs which possess m_s=0 spin components. According to SCRP theory (section 2.5), the singlet state $|S\rangle$ of the pair is partially mixed with the $|T_0\rangle$ triplet state. Thus, also the population of $|T_0\rangle$ is depleted by the singlet recombination process leaving an excess of population on $|T_{+1}\rangle$ and $|T_{-1}\rangle$ states. Charge recombination can happen from the radical ion pair to an energetically low-lying neutral triplet state transferring the excess population of $|T_{+1}\rangle$ and $|T_{-1}\rangle$ states. This process generates an excess of spin population in $|T_{+1}\rangle$ and $|T_{-1}\rangle$ states.

2.5 Spin Correlated Radical Pairs

After the photoinduced electron transfer process, the radical cation and the radical anion are in proximity of each other. While they are closer than ≈ 1.5 nm, both the dipole-dipole interaction and the exchange interaction must be considered in order to describe their EPR spectrum. This system is called *spin correlated radical pair* (SCRP). The spin Hamiltonian comprises the Zeeman Hamiltonian of both the electrons, the dipole-dipole coupling Hamiltonian and the exchange Hamiltonian. A unitary transformation

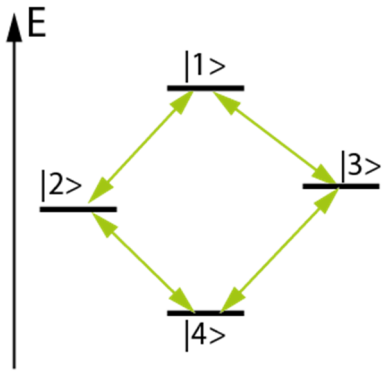

Figure 2.4 Diagram of the energy levels of SCRP at magnetic field $g\mu_B B_0 >> J$, $J < 0$. Green lines represent the allowed transitions.

is necessary to diagonalize the Hamiltonian and to calculate its eigenstates and transitions. This procedure leads to the following eigenstates:

$$\begin{aligned} |1\rangle &= |T_{+1}\rangle \\ |2\rangle &= cos\theta|S\rangle + sin\theta|T_0\rangle \\ |3\rangle &= -sin\theta|S\rangle + cos\theta|T_0\rangle \\ |4\rangle &= |T_{-1}\rangle \end{aligned} \tag{18}$$

where the mixing angle is $\theta = \frac{1}{2}\tan^{-1}\left(\frac{\frac{1}{2}\mu_B B_0(g_1-g_2)}{J+\frac{D_{zz}}{2}}\right)$. The corresponding energies are:

$$\begin{aligned} E_1 &= \omega - J + D_{zz}/2 \\ E_2 &= \Omega - D_{zz}/2 \\ E_3 &= -\Omega - D_{zz}/2 \\ E_4 &= -\omega - J + D_{zz}/2 \end{aligned} \tag{19}$$

Here, $\Omega^2 = \left(\frac{1}{2}\mu_B B_0(g_1 - g_2)\right)^2 + \left(J + \frac{D_{zz}}{2}\right)^2$ and $\omega = \frac{1}{2}\mu_B B_0(g_1 + g_2)$.

In Figure 2.4 the energy diagram for SCRP is reported together with the allowed spin transitions. Analogously to EPR spectra of photoexcited triplet states, also SCRP presents the phenomenon of spin polarization. Indeed, the photoinduced electron transfer is a spin selective mechanism. The polarization of the spectrum depends on the multiplicity of the precursor state of the radical pair state. If the precursor is a singlet state, $|2\rangle$ and $|3\rangle$ states will be predominantly populated. Conversely, if the precursor is a triplet state, $|1\rangle$ and $|4\rangle$ states will be mainly populated.

2.6 LINE BROADENING

The natural lineshape for spectroscopic transitions is a *Lorentzian* profile, with the width being determined by the inverse lifetime of the states involved in the transition – also called natural linewidth. *Homogeneous* spectral lines possess a linewidth that depends only on the lifetime of the states, whereas inhomogeneous lines may have additional line broadenings due to several interactions and are often of *Gaussia*n shape.

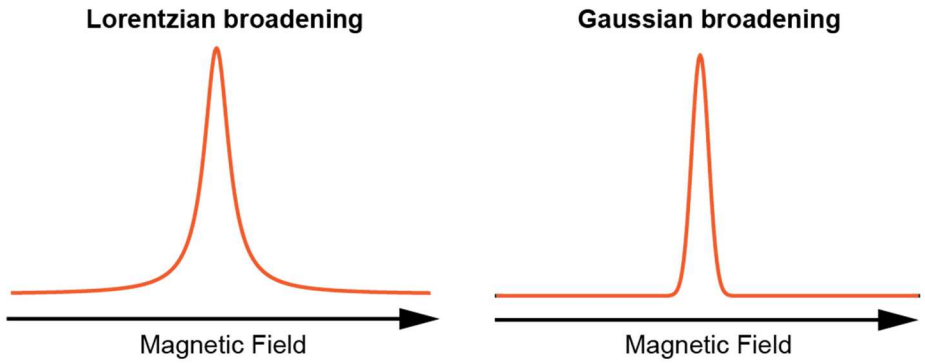

Figure 2.5 Examples of homogeneous (Lorentzian) and inhomogeneous (Gaussian) line broadening.

In Figure 2.5, the two kinds of line broadening are depicted. In the following the main mechanisms of line broadening are discussed.

2.6.1 Homogeneous Broadening

Homogeneous line broadening for a set of spins occurs when all spins see the same net magnetic field and have the same spin Hamiltonian parameters. This means that the lineshape is the same for each spin. The linewidth of homogeneously broadened EPR spectra is a measure of the interaction between spins. The main interaction among spin within organic materials is the magnetic dipolar coupling. In addition to this interaction, another important contribution to linewidth could derive from the microwave radiation.

In EPR spectroscopy, similarly to other magnetic resonance techniques, at sufficiently high resonant microwave powers, due to fast stimulated transition between the spin states a severe Lorentzian broadening of the line is observed. At the extreme limit of a strong microwave power, the populations of the upper and lower states are equalized and the EPR absorption decreases or even cancels. This phenomenon is called *saturation*.

2.6.2 Inhomogeneous Broadening

Several EPR inhomogeneous broadening mechanisms can be present in organic materials. The principal ones are: magnetic dipole-dipole interaction and unresolved hyperfine interaction.

The first occurs when two spin-carrying particles are nearby. In this case, the local magnetic field of the first spin is perturbed by the other and vice versa. This shifts the

resonance field of the two spins and if distances are statistically distributed, a Gaussian broadening can be expected.

The second mechanism is also a type of dipole-dipole broadening but due to the interaction between the electron spins and the surrounding nuclear spins (*hyperfine interaction*). If the number of interacting nuclei is very large, no individual hyperfine structure with a discrete splitting in the EPR spectrum is observed. Instead, the spectrum is averaged over many possible hyperfine interactions. Hence, only the envelope of all partially overlapping lines is detected.

2.7 TWO-LEVEL DYNAMICS

In order to describe the dynamics of a spin system two different formalisms are usually adopted: the classical vector model and the quantum mechanical density operator formalism. For the purposes of this thesis, the first description can be straightforward applied. This model describes the evolution of the macroscopic magnetization vector under the application of static and time-dependent magnetic fields. Spin relaxation phenomena are introduced in a phenomenological way. This classical description is usually suitable for the description of continuous-wave (CW) EPR and the most common pulsed EPR experiments.

2.7.1 THE VECTOR MODEL

In an ensemble of spins, the individual spins distribute themselves between the spin sublevels according to the Boltzmann distribution. The vector sum of all the spins produces a macroscopic magnetic moment whose value per unit volume is called magnetization $\boldsymbol{M}$. The net magnetization, which is the sum of all the spin magnetic moments, will be parallel to the external magnetic field since the xy components of the various magnetic moments cancel each other out and the parallel state of the magnetic moments (m_s=+1/2) will be more populated at the thermal equilibrium. The magnetization vector, which is also associated to an angular momentum, in a magnetic field precesses about the field direction at an angular frequency called Larmor frequency:

$$\omega_L = -\gamma_e \boldsymbol{B_0} \tag{15}$$

where γ_e is the gyromagnetic ratio. In a continuous-wave EPR experiment, the resonant condition is achieved when the Larmor frequency resulting from the sweeping magnetic field equals the monochromatic microwave radiation sent to the sample. In this condition an absorption of microwave radiation is detected.

In a pulsed EPR experiment, the microwave radiation is sent to the sample in the form of short (typically tens of nanoseconds) pulses of high intensity (up to kW peak power). To understand the effect of the pulses on a spin system, it is useful to describe the effect of the pulses in a reference frame rotating at a convenient frequency around the z direction. According to the rotating frame description, as long as the radiation (either CW or pulsed) is applied, the magnetization vector **M** precesses about $\mathbf{B_1}$, the oscillating magnetic field component of the microwave radiation, assumed parallel to the x direction, as described by the Bloch equations:

$$\begin{aligned} M_x &= 0 \\ M_y &= -M_0 \sin(\omega_{MW} t_p) \\ M_z &= M_0 \cos(\omega_{MW} t_p) \end{aligned} \tag{16}$$

Where t_p is the pulse length and $\beta = \omega_{MW} t_p$ is the flip angle of the magnetization.

2.7.2 Relaxation Phenomena

When a $\pi/2$ pulse is applied, the magnetization vector flips from z-direction into the xy plane and the spin system is clearly out of equilibrium. Since the spins interact with their surroundings, after e certain period of time the magnetization will return to the thermal equilibrium position. This process is called relaxation and is characterized by two constants: the longitudinal relaxation time, T_1 and the transverse relaxation time, T_2.

The longitudinal relaxation tends to restore the z component of the magnetization. The energy required to change the m_s number is provided by transient fluctuating fields which are induced by lattice vibration or molecular motion and is usually referred to as *spin-lattice relaxation*. On the other hand, the transverse relaxation cancels out the xy component of **M** (transverse magnetization) promoting the loss of phase coherence because the single spins tend to assume randomly distributed phases. This process is

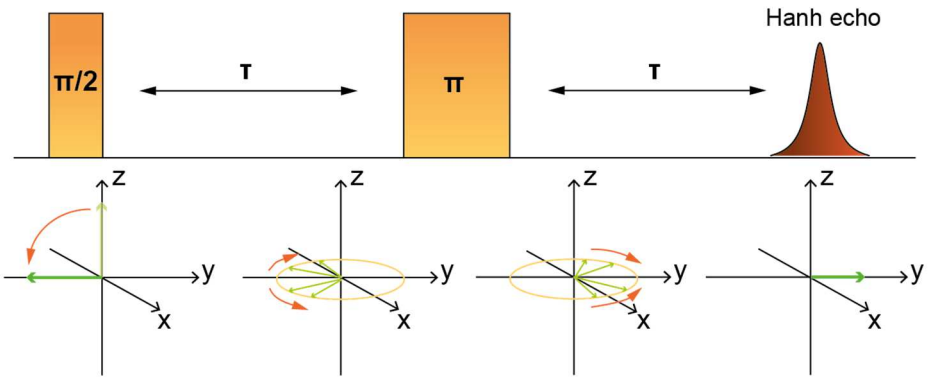

Figure 2.6 Pulse sequence and diagrams describing the motion of the magnetization vector in an Electron Spin Echo experiment.

usually referred as *spin-spin relaxation*. Both the relaxation processes are important when dealing with pulse EPR and their knowledge allows to obtain significant information about the chemical environment and the dynamics of the paramagnetic species.

2.7.3 Electron Spin Echo

Differently from Nuclear Magnetic resonance (NMR), the electron relaxation processes are too fast to allow the use of many pulse sequences used in standard NMR experiments. In particular, due to unavoidable instrumental *dead time* of a tens of nanoseconds the *free induction decay* (FID) detection is often impossible in pulsed EPR. To overcome this limitation, the echo sequence is regularly adopted. In Figure 2.6, the detailed pulse scheme is reported. The first $\pi/2$ pulse along the x direction turns the equilibrium magnetization onto the – y axis. At this point a free evolution period τ starts during which both the spin-lattice and spin-spin relaxation processes take place. In particular, the first mechanism restores the z component, while the second mechanism induces the spread of the individual spins orientation and reduces the xy plane component of **M.** The fanning out of the spins is induced by their slightly different precession frequencies due to their different surroundings. After a time τ, a π pulse is sent to the sample whose effect is to turn all the magnetization vectors by 180° around the x axis. This results into a re-focalization, after a time τ, of all the spins which have been previously dephased by the differences in precession frequencies. Conversely, the in-plane magnetization component that has been lost due to the relaxation processes is

not refocused by the π pulse. The refocused magnetization vectors along the y axis is called *electron spin echo* or *Hanh echo*.

2.8 EPR TECHNIQUES

2.8.1 STEADY STATE EPR

A standard continuous wave (CW) EPR experiment is carried out by sweeping the external magnetic field B_0, to vary the energy level separation of the studied spin system, and keeping the frequency of the monochromatic microwave radiation constant. When at a certain magnetic field, the resonant condition is fulfilled, an EPR signal is recorded. The external magnetic field is usually supplied by an electromagnet which typically can range from 0 1.5 Tesla (15000 Gauss), while the electromagnetic radiation is generated at a fixed monochromatic frequency (typically 9-10 GHz, the *X-band* microwave range) by a microwave source such as a Gunn diode electronic oscillator.

The microwaves travel from the source along a hollow metal waveguide and reach the sample inserted into a microwave resonator. When the resonator is critically coupled with the waveguide, a considerable energy is stored as a standing wave at the microwave frequency. EPR resonators are designed to maximize the amplitude of $\mathbf{B_{MW}}$ and minimize the dielectric losses due to the absorption of the electric field of the electromagnetic radiation which excites the rotational energy levels. At resonance, the sample absorbs the microwaves and the condition of perfect impedance coupling is lost: part of the radiation is reflected by the resonator and directed through a circulator towards a rectifier Schottky diode kept in its linear regime (≈ 200 μA) by an appropriate bias current.

Low-frequency noise reduction is achieved by a special kind of detection called *phase-sensitive detection* that is based on the use of a *lock-in amplifier* and a 100 kHz magnetic field modulation. As a result, the EPR spectra appear as the first derivative of the absorption spectrum.

In Light Induced EPR (LEPR), the sample is exposed to UV or visible illumination in the microwave cavity. Since the illumination is continuous, the LEPR technique is a steady-state technique that requires an appreciable steady state population of transient species: as a consequence, LEPR reveals only those species that possess lifetimes longer

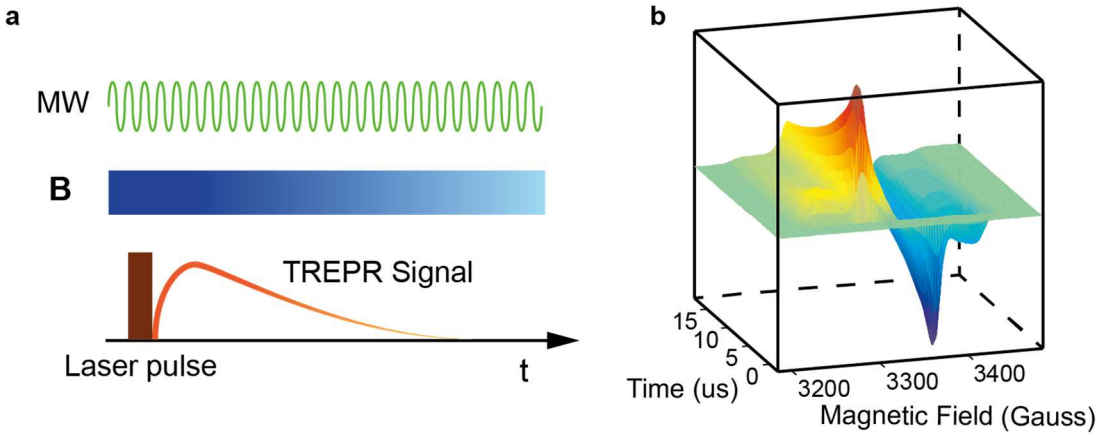

Figure 2.7 (a) Schematic of a typical TREPR experiment. For each value of the external magnetic field, the EPR intensity is recorded as a function of the time after the visible laser pulse. (b) Example of 2-dimensional TREPR spectrum.

than a few milliseconds. Therefore, excited triplet states and SCRP usually cannot be investigated through LEPR technique because of their too short lifetime. Nevertheless, thanks to its high sensitivity and selectivity, LEPR is one of the best technique to study long-living photogenerated radicals and radical ions in photoactive materials that are often trapped in stabilized sites and survive to fast recombination processes.

2.8.2 Time Resolved EPR

Time Resolved EPR (TREPR) is a transient EPR technique that allows to study paramagnetic species generated after a vis laser pulse, with a sub-microsecond time resolution. A standard TREPR experiment is graphically outlined in Figure 2.7. It consists in recording the EPR intensity as a function of time following laser excitation, with constant applied microwave radiation, for each magnetic field position. The detection is carried out without the use of the lock-in amplifier in order to achieve higher time resolution. As a consequence, TREPR spectra do not appear in first derivative. As discussed previously, the initial population of spin sublevels of photogenerated paramagnetic species differs from that of thermal equilibrium (spin polarization). Thus, TREPR spectra may appear both in enhanced absorption or in emission. Through the investigation of the polarization pattern it is possible to infer information about the first stages of the photophysical processes. In addition, spin polarization allows to overcome the problem of low signal to noise ratio due to the small differences in the equilibrium populations of the spin energy levels.

2.8.3 PULSE EPR

Three different pulse EPR experiments were carried out in this work: Echo Detected EPR (EDEPR), T_1 and T_2 measurements.

In a common EDEPR experiment, an echo pulse sequence (usually the Hahn echo sequence: $\pi/2$-τ-π-τ) is applied and the echo intensity is measured at each magnetic field position. The result is an absorption EPR spectrum which is free from lineshape distortions due to the field modulation generally employed in CW EPR. Other differences might occur because of different spin relaxation times in different part of the spectrum. In some cases, this effect can be used to discriminate between overlapping lines by a careful choice of τ.

To measure T_1 relaxation time, the Echo Detected Inversion Recovery sequence is commonly used. The sequence is composed of a π-T-$\pi/2$-τ-π-τ set of pulses and delays. The first pulse brings the magnetization onto the -x axis and afterwards. During the evolution time T, the magnetization tends to restore its equilibrium value along the +z axis with the characteristic relaxation time T_1. After the time T, the standard two-pulse echo sequence is performed. The echo intensity as a function of the time is recorded and the curve obtained can be usually fitted by a mono or multiexponential function. To measure T_2 the standard Hahn echo decay pulse sequence is used, where echo intensity is measured at different τ values. Also in this case, the decay curve can be fitted by a monoexponential decay function from which the characteristic time T_2 in obtained.

2.9 EXPERIMENTAL DETAILS

In this thesis, all the CW EPR spectra (with the exception of those reported in chapter 4) were recorded on an X-band Bruker Elexsys E580 spectrometer equipped with a variable Q resonator for continuous-wave and pulsed experiments. An Oxford ER4112HV cryostat was used to perform measurements at low temperatures. Typical CW EPR experimental parameters were: field modulation amplitude 1 G and microwave power 0.2 mW. For sample illumination, white light from a 300W xenon lamp, IR filtered and focused onto a quartz optical fiber was used. The optical system delivered about 50 mW/cm^2 of light irradiance to the sample.

EPR spectra reported in chapter 4, were recorded on a Bruker ER200D spectrometer equipped with a nitrogen-flow variable temperature system (Bruker BVT2000) for measurements in the temperature range 120K- 350K.

TREPR experiments were performed on the same Bruker ER200D spectrometer slightly modified, recording the EPR signal after a short laser pulse (Nd:YAG, Quantel Brilliant, 532 nm or 355 nm, 5 ns, about 5 mJ/pulse, pulse repetition rate 50 Hz) with a LeCroy LT344 digital oscilloscope. At each magnetic field position, an average of about 200 transient signals was usually recorded.

Finally, pulse EPR experiments were performed using an X-band spectrometer, Bruker Elexsys E580. Hahn echo pulse sequence with $\pi/2$ and π pulse lengths of 16-32 ns and an inter-pulse delay of 200 ns was used in EDEPR experiments. All data were recorded with a quadrature detection, i.e. revealing either the in-phase and the out-of-phase signal from the spin systems. For T_1 and T_2 relaxation time measurements, Hahn echo decay and Inversion Recovery sequences have been used with $\pi/2$ and π pulse lengths of 16-32 ns.

2.10 REFERENCES

(1) Weil, J. A.; Bolton, J. R.; Wertz, J. E.: Electron Paramagnetic Resonance: Elementary Theory and Practical Applications; Wiley, 1994.

(2) Atherton, N. M.: Principles of electron spin resonance; Ellis Horwood, 1993.

(3) Brustolon, M.: Electron Paramagnetic Resonance: A Practitioner's Toolkit; Wiley, 2009.

(4) Hintze, C.; Steiner, U. E.; Drescher, M. Photoexcited Triplet State Kinetics Studied by Electron Paramagnetic Resonance Spectroscopy. *Chemphyschem* **2017**, *18*, 6-16.

(5) Hore, P. J.; Hunter, D. A.; McKie, C. D.; Hoff, A. J. Electron paramagnetic resonance of spin-correlated radical pairs in photosynthetic reactions. *Chem. Phys. Lett.* **1987**, *137*, 495-500.

(6) Hoff, A. J.: Advanced EPR: Applications in Biology and Biochemistry; Elsevier Science, 2012.

(7) Franco, L.; Toffoletti, A.; Ruzzi, M.; Montanari, L.; Carati, C.; Bonoldi, L.; Po', R. Time-Resolved EPR of Photoinduced Excited States in a Semiconducting Polymer/PCBM Blend. *J. Phys. Chem. C* **2013**, *117*, 1554-1560.

(8) Niklas, J.; Beaupré, S.; Leclerc, M.; Xu, T.; Yu, L.; Sperlich, A.; Dyakonov, V.; Poluektov, O. G. Photoinduced Dynamics of Charge Separation: From Photosynthesis to Polymer–Fullerene Bulk Heterojunctions. *J. Phys. Chem. B* **2015**, *119*, 7407-7416.

(9) Niklas, J.; Poluektov, O. G. Charge Transfer Processes in OPV Materials as Revealed by EPR Spectroscopy. *Advanced Energy Materials* **2017**, 1602226.

(10) Schweiger, A.; Jeschke, G.: Principles of Pulse Electron Paramagnetic Resonance; Oxford University Press, 2001.

(11) Poole, C. P.: Electron Spin Resonance: A Comprehensive Treatise on Experimental Techniques; Dover Publications, 1996.

(12) Jeschke, G. Determination of the Nanostructure of Polymer Materials by Electron Paramagnetic Resonance Spectroscopy. *Macromol. Rapid Commun.* **2002**, *23*, 227-246.

PART II

EXPERIMENTAL PART

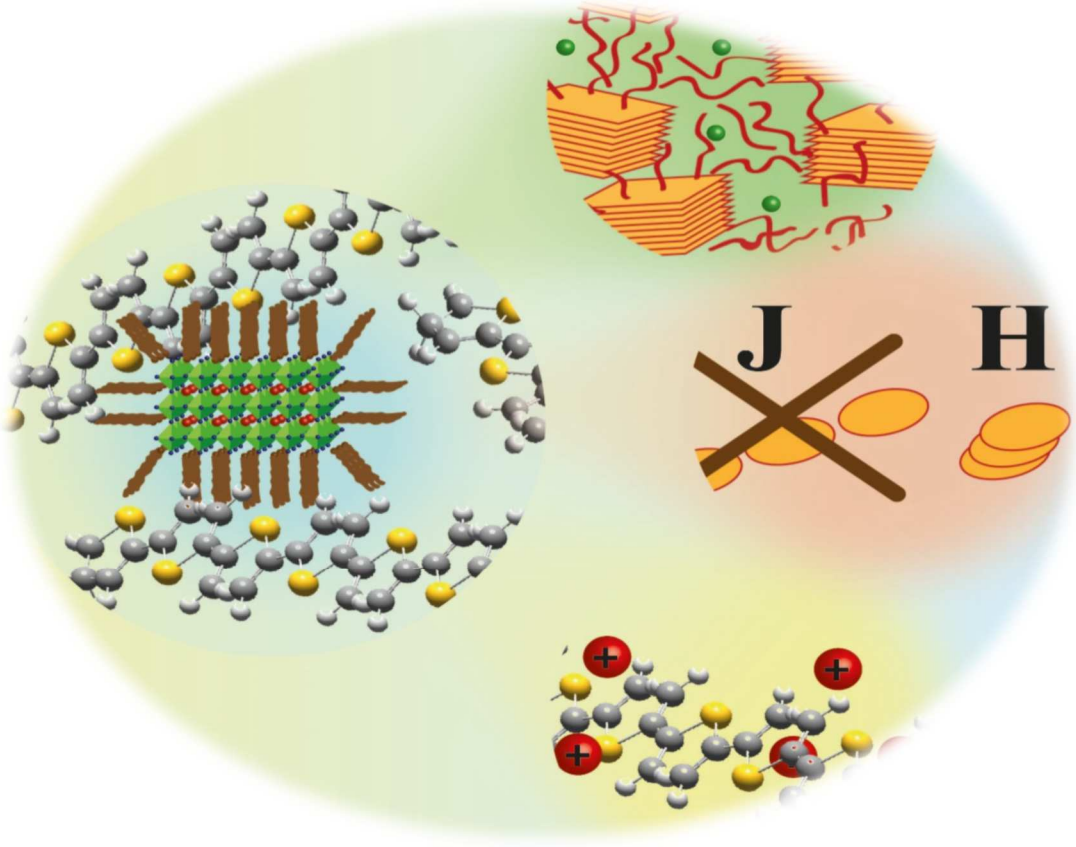

CHAPTER 3.
COLLOIDAL QUANTUM DOTS

Nanostructured architectures play a pivotal role in the evolution of next-generation photovoltaics facilitating new strategies for the design of solar cells.[1-3] In particular, colloidal Quantum Dots (QDs) are promising systems as photovoltaic materials in view of their broadband visible absorption, high extinction coefficients and energy level tunability through size control, facile synthesis and easy solution processability.[4-7] Among different configurations of QD-solar cells (QDSC), an enormous potential was gathered by bulk-heterojunction (BHJ) configurations.[2] Indeed, the combination of solution processable organic semiconductors and QDs have the potential to substantially reduce the costs of the solar cells and to improve the power conversion efficiency (PCE).

The PCE of the best organic photovoltaic systems is limited by many losses processes whose detailed understanding is still under investigation. The main losses mechanisms are basically the following: (1) the non-optimal absorption of the solar spectrum, (2) exciton recombination before diffusing to the donor/acceptor interface, (3) geminate recombination of polarons pair failing to fully dissociate and (4) non-geminate recombination losses occurring during the charge migration to the electrodes.[8,9] Hybrid systems composed of conjugated polymers and QDs are of particular interest for reducing the energetic driving force for charge separation due to the high dielectric permittivity and consequently low electrostatic binding energy within the inorganic phase.[10] First observations of photovoltaic effect in polymer/QDs were reported by Wang and Alivisatos.[11] Despite much effort spent, these solar cells only reached 4%

efficiency.[12] Indeed, one of the intrinsic short comings of this binary nanohybrids is poor, hopping-type electron transport by percolation in the inorganic phase that severely limits the achievement of high PCE. The introduction of ternary hybrid solar cells raised a possible alternative, solving transport limiting factors.[9,13-15]

Among possible acceptors in BHJ, fullerene (C_{60}) derivatives stand out as the most widely employed in binary polymeric solar cells and therefore are obvious candidates for ternary solar cells. Recently, the photoinduced electron transfer (PET) interaction between QDs and fullerenes was investigated in covalently bound dyads by Kamat and Medintz.[16,17] Although the PET within CdSe QDs-C_{60} dyads was studied both theoretically and experimentally, the charge generation at CdSe QDs/C_{60} interface in blended films still lacks a thorough characterization. The extensive understanding of QDs/C_{60} interactions is a crucial step for the comprehension of ternary solar cells operations.[9] In this direction, the scientific research has revealed that charge generation at this hetero-interface results in enhanced photocurrent and power conversion efficiency but only few works focused on the fate of generated charges in these systems.[18,19] Therefore, an in-depth analysis seems to be needed in order to have a complete overview of the main processes occurring in QDs BHJ solar cells and to suggest new possibilities for increasing their PCE.

In this chapter, a detailed photo-physical analysis of the main processes that take place in model fullerene/QDs blends composed of thin shell quasi-type II QDs (CdSe/CdS) and the fullerene derivative PCBM is described. The choice of CdSe QDs with a shell constituted by a CdS monolayer was based on the following points:

i) CdS layer is known to passivate the surface defects of CdSe QDs that can be competitive with the PET process.[20]

ii) the thin monolayer of CdS induces only a limited confinement of the exciton in the QDs core compared to thicker layers, thus enhancing the PET process.[21]

The work described in this chapter was aimed at properly modifying the interactions between QDs and PCBM by exploiting the surface chemistry of QDs and tracking the dynamics of charge generation, separation, and recombination in PCBM/QDs blends.

In section 3.1, the ligand exchange procedure is described. In particular, the ligand exchange process was carried out using three different ligands (oleylamine (N18), octadecanethiol (S18) and propanethiol (S3)) with the aim to rationalize how the length and the different nature of the capping ligands influence the PET process. In section 3.2, the Light Induced EPR measurements performed on the neat PCBM film and the three QDs/PCBM blends are reported. The analysis discloses that a significant electron transfer occurs from QDs to PCBM and that its efficiency strongly depends on the capping ligands. In particular, the thiol functionalization and a shorter length favours the electron transfer process. In section 3.3, the TREPR spectra are reported. The analysis shows that not only the electron transfer but also the following charge separation and recombination processes are strongly influenced by the presence of QDs. In section 3.4, the spin relaxation analysis demonstrates that photogenerated charges, in particular the PCBM anions, are stabilized in proximity of QDs. Finally, in section 3.5, the complete photophysical description PCBM/QDs blends is summarized. The conclusions and the experimental details are reported in sections 3.6 and 3.7, respectively.

3.1 LIGAND EXCHANGE

Starting from as-synthesized CdSe/CdS quantum dots functionalized with oleylamine (details on the synthesis of N18 QDs are reported in section 3.7), the native amine ligands were exchanged with alkanethiol molecules. The ligand exchange procedure takes advantage of different binding ability of thiols and amines to CdS surface, according to HSAB theory for X-type ligands.[28, 29] The purification of ligand-exchanged QDs was carried out by precipitation in an acetone: methanol (1:1) mixture and re-dissolving the precipitate in toluene.

In order to monitor and confirm ligand exchange reaction, we performed both optical and nuclear magnetic resonance analysis.

Absorption and photoluminescence (PL) spectra of CdSe/CdS QDs capped with the three different ligands are reported in Figure 3.1. On the one hand, Figure 3.1.a shows that the absorption spectra are similar for the three ligand-exchanged QDs underlining that the nature of the absorptive states is unvaried in the three samples. On the other hand, PL spectra of CdSe/CdS QDs are extremely sensitive to thiol binding (Figure

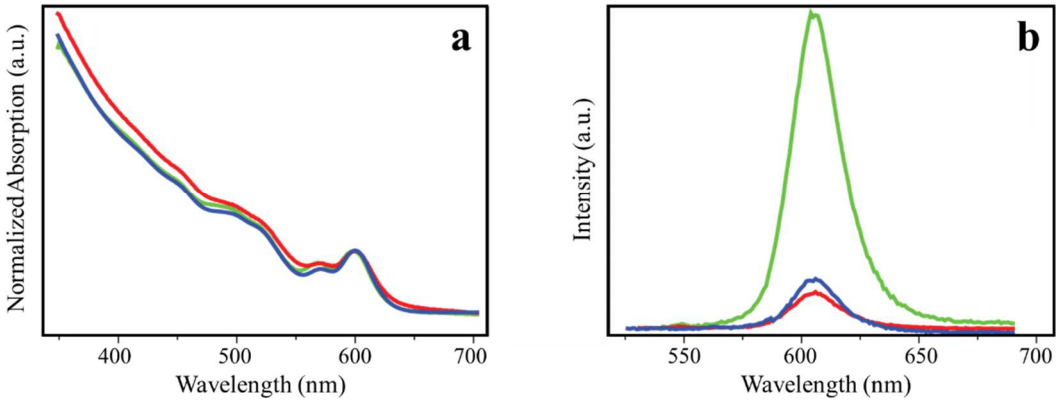

Figure 3.1 Normalized (a) absorption and (b) PL spectra of N18 QDs (green), S3 QDs (red) and S18 QDs (blue).

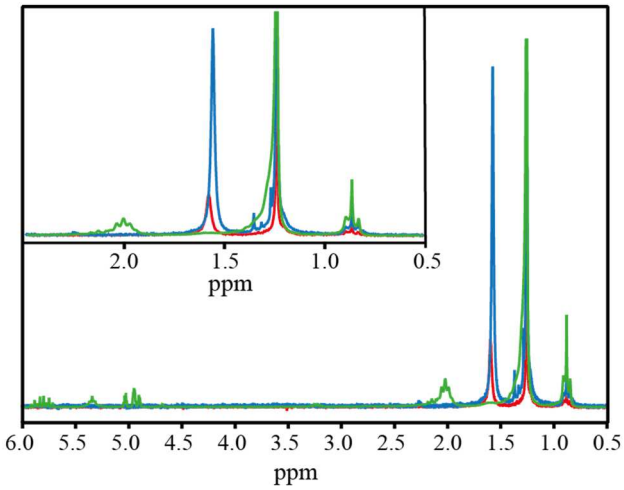

Figure 3.2 ^{1}H-NMR spectra of N18 QDs (green). S3 QDs (red) and S18 QDs (blue) in $CDCl_3$. A zoom in the 2-6 ppm region is shown in the inset.

3.1.b). Actually, PL spectra show a severe quenching in S3 QDs and S18 QDs with respect to N18 QDs. This PL quenching is attributed to thiol-mediated hole trapping process becoming dominant over radiative recombination. Indeed, the redox thiol levels lay above the valence band of CdSe-based QDs. According to Scholes and Minotto, this promotes exciton trapping via band-edge charge transfer process.[20,22] Despite the differences in the PL intensity, the PL band shape is unchanged suggesting that also the nature of emissive states remains unvaried.

Besides optical characterization, which provides an indirect evidence of ligand exchange, a direct evidence was obtained using ^{1}H-NMR spectroscopy (Figure 3.2).

The reported ^{1}H NMR spectra are characterized by large linewidths associated with the reduced conformational motion of the bound ligands.[23] After ligand exchange procedure, the disappearance of peaks at 5.35 ppm and 2.02 ppm ascribed respectively to alkenyl protons and protons attached to carbon atoms adjacent to the double bond of bound oleylamine, is the signature that ligand exchange occurred. A further confirmation is the appearance of a strong peak at 1.60 ppm attributable to bound thiols.

3.2 LIGHT INDUCED EPR

Having verified the success of the ligand exchange procedure, we focused our attention to the study of the photoinduced interactions between our QDs and the fullerene derivative PCBM. We investigated the neat PCBM film and the PCBM/N18, S3 and S18 QDs blends. The experimental details for the film deposition are described in section 3.7.

First, the study of the PET between QDs and PCBM using Light Induced EPR (LEPR) spectroscopy was carried out. LEPR allows to detect long-living paramagnetic species generated after UV-vis light absorption.[24] The LEPR spectra (light ON minus dark) recorded in the neat PCBM film and in the three PCBM/QDs blends at 80K are reported in Figure 3.3. The spectra acquired before light illumination (dark) do not show any appreciable signal. This evidence highlights that no ground state electron transfer occurs. On the other hand, under illumination (light ON) a strong and relatively narrow EPR line (less than 10 Gauss) is detected. In the neat PCBM film, the presence of two weak EPR signals whose g-values and lineshape are reminiscent of stable radicals localized on PCBM can be attributed to a weak PET process.[24-26] This result demonstrates the partial double behaviour (both electron donor and acceptor) of the material. The effect is however small and the donor behaviour of the PCBM is certainly secondary. In the PCBM/QDs blends, a much stronger EPR signal is detected. In particular, from the best-fit spectral simulation the anisotropic g-values (g_1 = 1.9992, g_2=2.0000 and g_3=2.0004) typical of the PCBM anion are found.[27] The presence of the long-living PCBM anion under illumination demonstrates that a PET occurred in the blend between the QDs and the PCBM. The counterpart radical cation localized on the QDs is not detected possibly because of a severe line broadening due to the presence of heavy elements Cd and Se that favour fast spin relaxation times.[9,18,28]

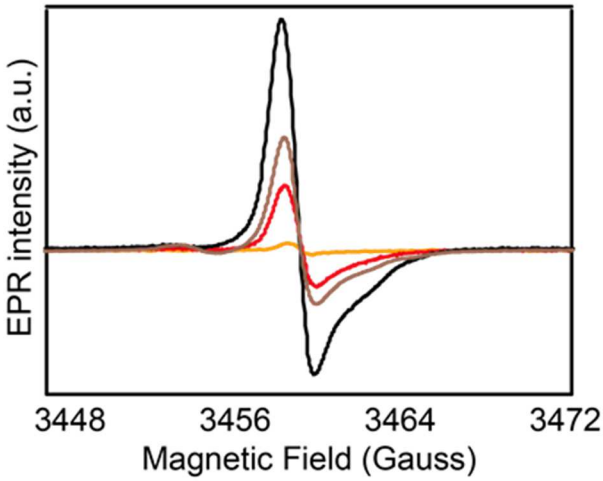

Figure 3.3 LEPR spectra of PCBM film (orange), PCBM/N18 QDs (red), PCBM/S18 QDs (brown) and PCBM/S3 QDs (black) acquired at 80K. The spectra shown are the difference between spectra recorded under illumination of the sample using visible light (light ON) and those recorded before sample illumination (dark).

Moreover, as shown in Figure 3.3, the different EPR intensities of the three blends (respectively, PCBM/S3, S18 and N18 QDs) allow inferring a variable effect of the QDs ligands on charge carrier photogeneration. Indeed, a stronger LEPR signal is shown in PCBM/S3 QDs blend. This observation underlines that both the thiol functionality and the shorter length of ligands promotes the PET process. To rationalize this result two evidences can be considered. First, as previous observed, the thiols favour the hole trapping process over the radiative recombination.[20] The hole stabilization favours the subsequent electron transfer process towards the PCBM. Second, in line with Marcus theory a shorter ligand length implies a stronger electronic coupling of the QDs to the PCBM favouring the PET.[29]

Further insights into the fate of photo-generated carriers are provided by temperature resolved LEPR spectra of the four samples. We recorded the spectra at three different temperatures: 130K, 160K, and 190K (Figure 3.4). The spectra show the same EPR signal previously attributed to the long-living PCBM anion[24-26] and a common trend in the EPR intensities can be observed by increasing the temperature. The LEPR spectral intensities decrease with increasing temperatures, until almost disappear at 190 K. This result is rationalized on account of the Curie law and a shorter lifetime of the photo-generated charge carriers. At increasing temperatures, the thermal activated de-trapping of the charge carriers increases and more efficient non-geminate recombination of the

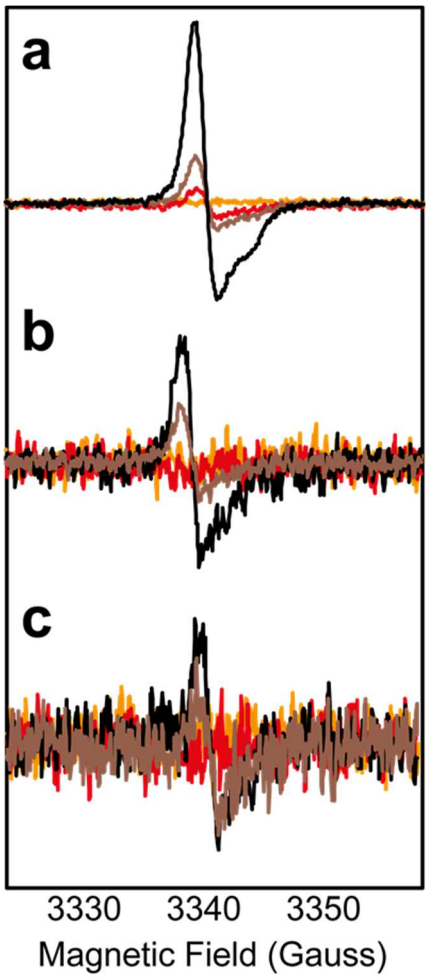

Figure 3.4 LEPR spectra of PCBM film (orange), PCBM/N18 QDs (red), PCBM/S18 QDs (brown) and PCBM/S3 QDs (black) blends recorded at (a) 130K, (b) 160 and (c) 190K. The spectra shown are the difference between the spectrum recorded under illumination of the sample using vis light (light ON) and that recorded before sample illumination (dark).

charge carriers occurs.[30] A higher charge carrier recombination results in a lower EPR intensity. This result is further corroborated by the light OFF measurements (spectra acquired after the light is turned off). Indeed, when the light illumination of the samples is turned off at 80K, the EPR spectra maintain the same shape, field position and intensity. This observation suggests that the photogenerated species are stable at 80K and charge recombination is negligible. However, at higher temperatures, after switching off the illumination, the EPR spectra decay faster and at room temperature the dark spectrum, with no EPR signal, is quickly restored. This observation indicates that a thermally activated process is dominating the charge lifetime: it could be the charge de-trapping, the charge mobility, the charge recombination rate or all of them.[30]

3.3 TIME RESOLVED EPR

Different photo-physical processes, such as charge separation and recombination, compete in determining the fate of photo-generated carriers. TREPR with microsecond time resolution gives access to useful information on these processes.[31]

The TREPR spectra of PCBM/S3 QDs blend recorded at 80K (a) and 130K (b) and their simulations are reported in Figure 3.5. These spectra are composed of a broad band extending for about 200 Gauss, in emission at lower fields and in enhanced absorption at higher fields, and a sharp central peak in absorption. As for the second component, the peak position, the linewidth and the absorption polarization are reminiscent of PCBM radicals. Their presence is in accordance with LEPR spectra reported in Figure 3.4 and further corroborates the occurrence of photoinduced electron transfer. As for the first component, the broad linewidth, the peculiar emissive/absorptive character and the field position are features commonly observed in TREPR spectra of photoexcited triplet states. From best-fit spectral simulations, we obtained the zero-field splitting (ZFS) parameters, D and E, which define the magnetic dipolar interaction between the two unpaired electrons of the triplet state. For both spectra in Figure 3.5 the typical ZFS parameters of PCBM excited triplet state are obtained and reported in Table 1.[31,32]

The emissive/absorption character of triplet state results from non-equilibrium population of excited triplet state spin sublevels and contains the information on which process is generating the triplet state. From the simulation, we observe that two main

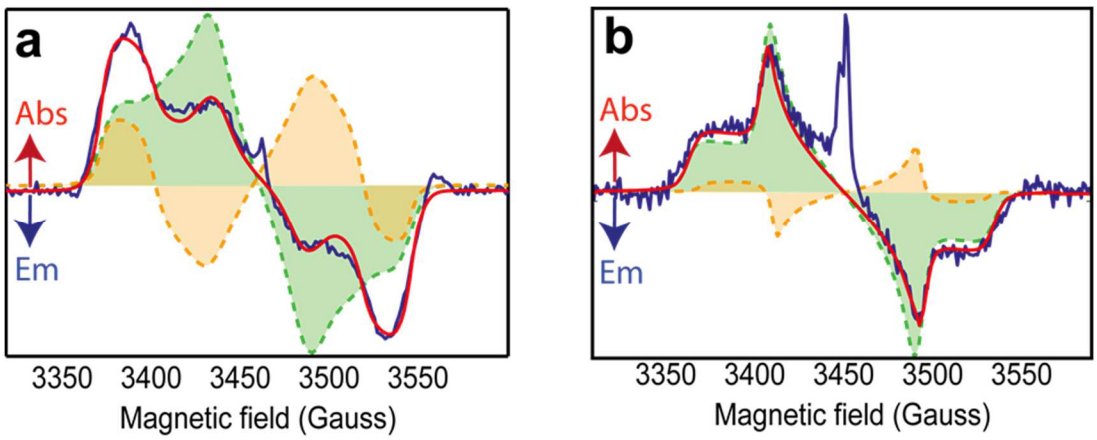

Figure 3.5 TREPR spectra of PCBM/S3 recorded 1 μs after a 532nm laser pulse (dark line) and best fit spectra (red line) at (a) 80K and (b) 130K. ISC triplet (green line) and Recombination Triplet (orange line) fit contributions (dashed lines and areas) are also reported. Abs=Absorption, Em=Emission.

contributions must be taken into account to simulate the TREPR spectra: (a) Intersystem Crossing (ISC) from the excited singlet state and (b) geminate recombination of the charge carriers (CT state recombination).

The component of the triplet simulated by a ISC population underlies the presence of excited states of PCBM generated by direct light excitation that undergo singlet to triplet conversion. For a correct simulation of this component, the relative values of the three zero field triplet spin sublevels population (P_x, P_y, P_z) were considered, from which the population at high field were computed using the same mixing coefficients that transform the zero field states into the high field ones.[33]

On the other hand, recombination component indicates the possibility for the photo-generated charge transfer (CT) state to recombine in a short time before charge separation (CS) occurs (geminate recombination). To simulate this component an excess population in the triplet states T_{+1} and T_{-1} must be used.[31] The excess population on these states can be explained in the frame of the SCRP theory. The pair (CT state) composed of the interacting photo-generated QDs cation and PCBM anion can exist in four spin states, which in general are linear combinations of one singlet state and three triplet states. The normal recombination pathway of charge carriers starts from the radical ion pair in singlet state, which decays to the singlet ground state by a spin-allowed back-electron transfer. The singlet-state recombination eliminates all the pairs which possess $m_s = 0$ spin components. According SCRP model, the singlet state of the pair is partially admixed with the T_0 triplet state of the pair. Thus, also the population of the triplet T_0 state is depleted by the singlet recombination process leaving an excess of population on T_{+1} and T_{-1} states of the pair. If charge recombination happens from the radical ion pairs in triplet state, a lower energy neutral triplet state is populated transferring the excess population of T_{+1} and T_{-1} states of the pair into the spin states of the lowest energy neutral triplet state, whose polarization pattern is the one we observed.

From simulation, we obtained the relative weight of the two contributions revealing a different behaviour at 80K and 130K. At 80K the recombination mechanism is more pronounced with respect to 130K. From this evidence, we conclude that after the generation of the CT state the charge separation process, competitive with geminate recombination, is a thermally activated process and at lower temperature fewer charge

carriers manage to overcome the Coulomb attraction barrier, therefore favouring the geminate recombination. The same analysis was carried out for the other three samples to confirm the result. The TREPR spectra recorded at 80K and 130K for the neat PCBM film, the PCBM/N18 QDs and PCBM/S18 QDs blends, together with the respective simulations are reported in Figure 3.6. In Table 3.1, the best-fit spectral simulation parameters for all the studied samples are listed. Clearly, all the TREPR spectra show PCBM triplet states that are the result of the sum of the ISC contribution and the geminate recombination contribution, similarly to Figure 3.5. In all the blends, the recombination contribution is significant at 80K, but markedly decreases at 130K. Conversely, the neat PCBM film shows a substantial recombination contribution even at 130K. This evidence demonstrates that the QDs influence not only the electron transfer process but also the charge recombination and separation mechanisms. In particular, the presence of QDs favours the charge separation thus lowering the efficiency of charge recombination from the geminate CT state. A further discussion on this point is given in section 3.5.

3.4 Spin Relaxation Processes

To complete the photophysical scenario and investigate the chemical environment of long-living PCBM anion, we performed pulsed EPR experiments for the determination of the spin relaxation times of the photogenerated charges in the three blends and in the neat PCBM film. The pulse sequences used were Inversion Recovery for spin-lattice relaxation time (T_1) and Hahn Echo Decay for spin-spin relaxation time (T_2), both performed under continuous white light illumination of the samples.[34]

Figure 3.7 shows an example (for the PCBM/S3 QDs blend) of the experimental curves (echo intensity recovery and echo intensity decay) for the determination of T_1 and T_2, recorded at magnetic field position corresponding to the maximum of the EPR spectrum, i.e. the PCBM anion. In the same figure the multi-exponential best-fit curves are also shown. The same experimental and fitting procedure was carried out for all the samples. From the best fits of the curves, the spin relaxation times were determined and reported in Table 3.2. Clearly, a significant decrease of T_1 and T_2 for the three blends in comparison with the neat PCBM film is observed. The faster electron spin relaxation rate in the blends can be explained by a variety of reasons.[34] First, the increased

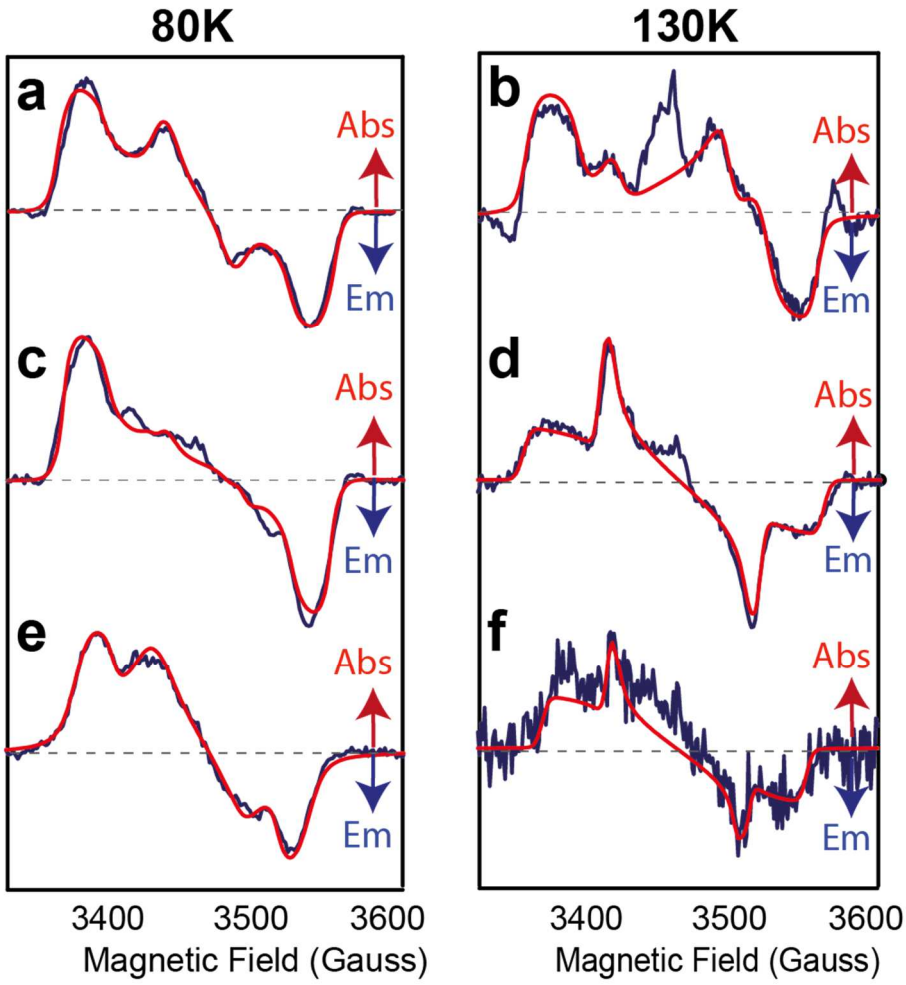

Figure 3.6 TREPR spectra of (a,b) PCBM film, (c,d) PCBM/N18 QDs and (e,f) PCBM/S18 QDs blends recorded 1 μs after a 532nm laser pulse (dark line) and best fit spectra (red line) at (a,c,e) 80K and (b,d,f) 130K. Abs=absorption, Em=Emission.

		ISC			Recombination				
		D(Gauss)	E(Gauss)	(Px,Py,Pz)	D(Gauss)	E(Gauss)	($P_+ - P_0$, $P_0 - P_-$)	ISC %	Rec. %
80K	PCBM	-87	13	(0.4, 0.6, 0)	-90	-10	(1, -1.14)	61	39
	PCBM/N18 QDs	-87	11	(0.4, 0.6, 0)	-87	11	(1, -1.12)	53	47
	PCBM/S18 QDs	-85	8	(0.4, 0.6, 0)	-89	-11	(1, -1.23)	61	39
	PCBM/S3 QDs	-87	11	(0.4, 0.6, 0)	-87	-10	(1, 1.1)	61	39
130K	PCBM/N18 QDs	-91	6	(0.4, 0.6, 0)	-89	-9	(1, -1.3)	38	62
	PCBM/S18 QDs	-92	0	(0.4, 0.6, 0)	-90	0	(1, -1)	84	16
	PCBM/S3 QDs	-92	0	(0.4, 0.6, 0)	-90	0	(1, -1)	73	27
	PCBM/N18 QDs	-91	0	(0.4, 0.6, 0)	-85	0	(1, -1)	80	20

Table 3.1 Best fit zero-field spitting values (D, E) and populations (Px, Py, Pz and $P_+ - P_0$, $P_0 - P_-$) for the simulation of triplet states in TREPR spectra reported in Figure 3.5 and Figure 3.6.

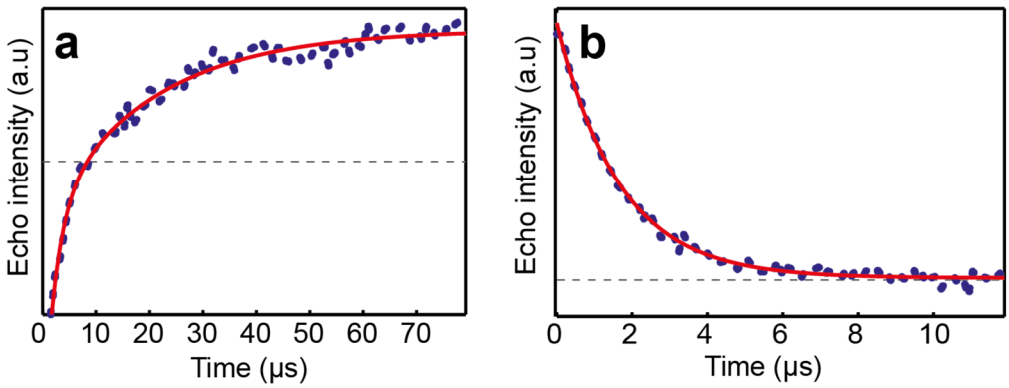

Figure 3.7 (a) T_1 Inversion Recovery and (b) T_2 Hahn Echo Decay experiments performed at 80K (blue dots) and exponential best fitting (red lines) for PCBM/S3 QDs blend. Similar curves were obtained also for the other blends.

Sample	T_1 (μs)	T_2 (μs)
PCBM	6.3 (0.9)	5.4 (1.5)
	57.0 (0.7)	
PCBM/N18	2.5 (0.3)	2.3 (0.2)
	16.0 (0.3)	
PCBM/S18	2.1 (0.1)	1.74 (0.07)
	11 (0.1)	
PCBM/S3	2.4 (0.2)	1.66 (0.06)
	20.0 (0.2)	

Table 3.2 Electron Spin Relaxation Times T_1 and T_2 calculated respectively through the bi-exponential and mono-exponential fitting of Echo Detected Inversion Recovery and Hahn Echo Decay experiments performed at 80K.

magnetic dipolar interaction between the PCBM unpaired electron and the hydrogen nuclei of the ligand shell can increase the relaxation rate of the PCBM radical anion. Second, the spin-orbit interaction in the heavy atoms of the QDs (Cd, Se) is known to drastically influence the spin relaxation times if the unpaired spin density of the anion partially overlaps with the QDs electronic states. Other mechanisms could be envisaged, but regardless the specific process contributing to the electron spin relaxation, all mechanisms must assume a non-vanishing interaction between the PCBM anion and the QDs or their ligand shells. Therefore, this result suggests that long-living PCBM anions within the blends are localized in short proximity (<1 nm) of the QDs, close enough to sense the presence of the ligand shell and/or of the inorganic core.

3.5 COMPLETE PHOTOPHYSICAL PICTURE

In order to rationalize our observations and get a complete picture of the PCBM/QDs blends photophysics, the multitude of paramagnetic species that can be produced upon light excitation should be discussed.[35]

3.5.1 CHARGE TRANSFER

After the primary absorption process, a singlet excited state (S = 0) is produced in the fullerene derivative and/or in the QDs. The main decay pathways of the excited state are (1) the decay to the ground state (via radiative emission or nonradiative deactivation processes), (2) the conversion to the excited triplet state (S = 1) via ISC promoted by spin−orbit interaction and (3) the electron transfer processes. In PCBM/QDs blends, the high electron affinity of PCBM (-3.9eV)[36] is compatible with electron transfer process at interface with QDs (-3.1eV, energy of the conduction band edge estimated for 2.1 nm radius from literature[37]). In addition, a peculiar electron transfer mechanism was recently proposed for QDs.[38] Auger-assisted electron transfer allows to circumvent the typical Marcus inverted region, thanks to assistance of Auger processes in storing energy exceeding the reorganization energy. Consistently with estimated energy levels, we found our QDs-PCBM couple to be in Auger-assisted regime, being ($-\Delta G$ [800meV]>λ[~400meV]).

Using surface chemistry, we aimed to tune the interaction between CdSe/CdS QDs and PCBM enhancing the electron transfer process. Ligand exchange procedure acts on two basic factors determining charge generation: (1) the distance between QDs electron-donor and PCBM electron-acceptor, (2) the nature of excitons in QDs. The length of ligand alkyl chain determines the donor-acceptor distance, within blends. According to Marcus theory a shorter donor-acceptor distance favours the electron transfer.[29] Moreover, the presence of redox levels above valence band gives rise to a Type-II hetero-interface.[39] The drastic decrease of PL efficiency, according to the literature[37-39], suggests the presence of hole trapping. Therefore, thiols ligands are able to reduce the exciton binding energetic barrier and therefore can promote charge transfer.[20] These observations are in line with the LEPR analysis (Figure 3.3 and Figure 3.4). Indeed, from the EPR intensities at different temperatures the increased electron transfer efficiency in PCBM/S3 QDs blends is observed.

3.5.2 Charge Separation vs. Geminate Recombination

Following electron transfer, a large variety of processes can occur within photoactive blends.[24,35] Electron transfer from QDs to PCBM (or alternatively between two PCBM molecules) generates a Charge Transfer state (CT state) whose charges are localized on adjacent species (cation on QDs and anion on PCBM molecule). The CT complex can either dissociate into free charges (Charge Separated state, CS state), where the Coulomb attraction between the charges is significantly lower than k_BT, or it can geminately recombine to the ground state following many roads, such as the direct transition to the ground singlet state or the back-electron transfer to the donor (acceptor) triplet excited state. The generation of a CS state requires the overcoming of the Coulomb attraction between cations and anions. We performed a rough estimate of Coulomb binding energy (BE) of CT state considering the dielectric constants of the various blends and the distances between the charge carriers. In the PCBM/QDs blends, Maxwell-Garnett approximation can be used to estimate the effective dielectric constant of the mixture.[42] We estimate that the ratio $BE_{PCBM}/BE_{QDs:PCBM}$ can range from 2.5 to 4. Uncertainty stems from difficulties in precise evaluation of size dependent dielectric constant of the QDs and not clearly defined distance between the charges in the CT state. Nevertheless, an evident reduction of the Coulomb attraction contribution in the binding energy of CT states of PCBM/QDs blends compared to PCBM neat film is expected. This result, despite the severe approximations of the calculation, explains the partial suppression of geminate recombination process observed from the best-fit spectral simulation of TREPR spectra of PCBM/QDs blends at 130K reported in Figure 3.5 and Figure 3.6 and the enhanced charge separation observed in LEPR spectra in Figure 3.3. For a more precise evaluation of the charge separation efficiency from the CT state, the combined effect of other contributions to the binding energy of the CT state should be evaluated, such as surface multipoles, dark dipole, entropy effect, hot CT state mechanism and local charge carrier dynamics.[43]

3.5.3 Trapping and De-trapping

Trap states, defined as spatially localized states within the energy gap, generated by the system inhomogeneity, play a remarkable role in photovoltaic material performances.[44,45] Trapping of separated charge carriers is a mechanism, which results

in considerable space charge generation. Temperature plays a pivotal role in determining trap dynamics. Indeed, if the thermal energy is sufficient, a trapped charge can be de-trapped into a free charge.[46] In particular, at increasing temperatures both mobility of the charges and charge de-trapping mechanism are enhanced (as they are thermally activated) and the encounter and recombination probability for two opposite charge carriers increases. LEPR spectra at various temperatures reported in Figure 3.4 are in accordance with this model. Indeed, the EPR signal that is generated by long-living radicals (trapped charges) decreases and nearly disappears at higher temperatures where the activation barrier for the de-trapping process can be overcome more easily and the non-geminate recombination is enhanced.

Spin relaxation times are influenced by trap dynamics as well. In particular, since T_1 and T_2 relaxation times are affected by many contributions, such as magnetic dipole and hyperfine interactions, their measurement gives insight into the dynamics and the chemical environment of the paramagnetic species. In our case, QDs can be considered as inhomogeneity sites in the PCBM phase. Therefore, energetically deeper trap states are probably localized in proximity of QDs. Following this picture, the most stable electron traps are expected to be found sufficiently close to QDs (less than few nanometers) to strongly affect T_1 and T_2 relaxation times of the PCBM anion. This simple and qualitative model is well in accordance with the data reported in Table 3.2 in which a shortening in spin relaxation times of PCBM anion for all the blends compared to the neat PCBM film is observed.

In Figure 3.8, the main photophysical processes taking place in PCBM/QDs blends and in PCBM neat film are compared. Following an electron transfer event, charge transfer (CT) state is generated. CT state behaves differently if QDs are present in the material. In the PCBM film, the CT state mainly recombines by geminate recombination to the PCBM triplet, while in the blends charge separation is favoured by the reduced binding energy. Photo-generated free charges can be trapped, generating stable long living species that can be detected through EPR, or can encounter opposite charges producing non-geminate recombination. In case of trapping, the proximity of the charge traps to QDs domains induces much shorter T_1 and T_2 spin relaxation times compared to the neat PCBM film, as revealed by pulsed EPR measurements.

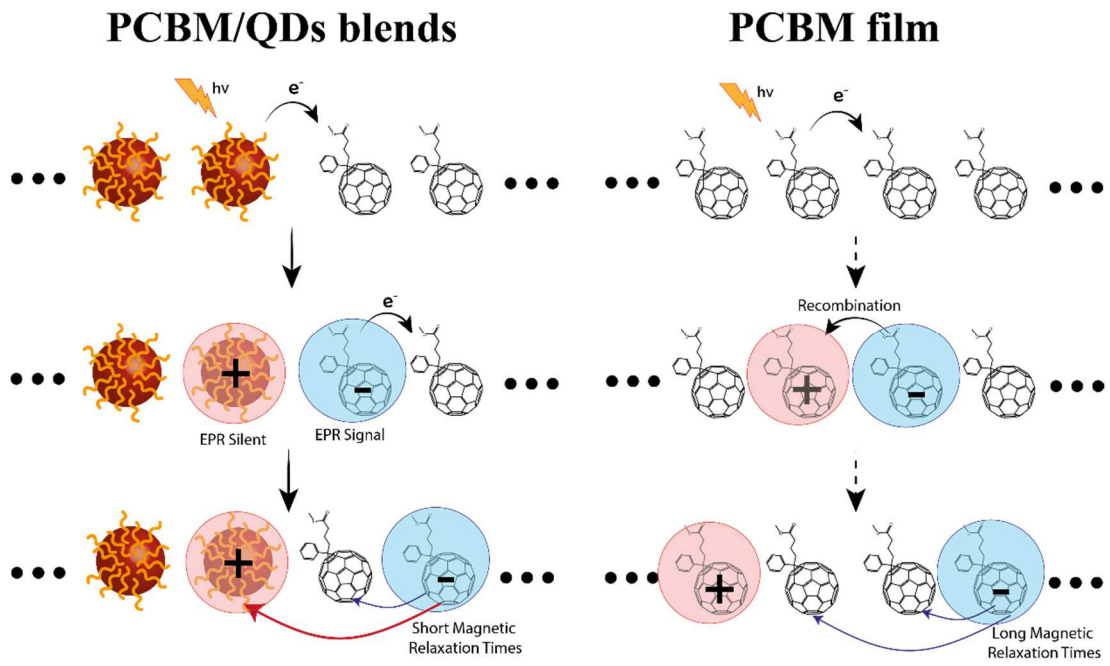

Figure 3.8 On the left, the photophysical processes occurring in the PCBM/QDs blends are depicted. After light absorption, a strong photoinduced electron transfer occurs from QDs to PCBM. The electron transfer generates a CT state that either dissociates into free charges (CS state). PCBM anions are stabilized in proximity of QDs. Conversely, on the right, the photophysics of the neat PCBM film is represented. In this case, after light absorption a weak electron transfer between PCBM molecules occurs and the generated CT state mainly recombines into the low-lying PCBM triplet state.

3.6 CONCLUSIONS

In this chapter, the investigation of the photophysical processes occurring in PCBM/QDs blends was described. QDs capped with three different ligands (namely, oleylamine N18, octadecanthiol S18, and propanethiol S3) were prepared and subsequently blended with the fullerene derivative PCBM.

By using a variety of EPR methods, the influence of QDs on the main processes taking place in organic active layer and the possibility of finely tune QDs interactions with PCBM by acting on their surface chemistry was demonstrated.

Light Induced EPR (LEPR) investigation performed on PCBM/N18, S18 and S3 QDs blends and in PCBM neat film showed the presence of a significant electron transfer from QDs to PCBM. This process is particularly favoured in PCBM/S3 QDs blend and the result was attributed to the hole scavenging effect promoted by thiol and to the lower distance between the electron-donor and electron-acceptor species, in line with Marcus

theory. In addition, LEPR measurements performed at different temperatures suggested a thermally activated recombination mechanism of the photogenerated charges.

Time-resolved (TREPR) analysis showed that the presence of QDs not only affects the efficiency of electron transfer but also charge separation and recombination processes. Notably, QDs decrease the Coulomb binding energy of the charge transfer state favouring the charge separation process and preventing geminate charge recombination.

Finally, pulsed EPR measurements of PCBM anion spin relaxation times suggested the stabilization of photogenerated charge carriers, in particular the PCBM anion, in proximity of QDs.

In conclusion, the incorporation of QDs into photovoltaic technology appears to be extremely interesting, as long as surface chemistry of QDs is properly developed. The tailoring of QDs interactions in photovoltaic blends can be a fundamental step toward their effective integration into efficient devices.

3.7 EXPERIMENTAL

3.7.1 QDS SYNTHESIS

CdSe cores were prepared following a slightly modified procedure described by van Embden et al.[47] Shell growth and consequent core-shell QDs synthesis, was based on a modified SILAR protocol reported in ref.[48,49] Multiple solvent extractions were used to purify QDs (cyclohexane, methanol and acetone).

Thereafter, the as-synthesized CdSe/CdS core-shell QDs functionalized with the native amine ligands (N18) were ligand-exchanged using two different alkanethiol molecules: propanethiol (S3) and octadecanethiol (S 18). The ligand exchange process was performed by adding an excess quantity of alkanethiol molecules to the pristine solution of N18 QDs. Subsequently, the ligand-exchanged QDs were purified by precipitating them with an acetone:methanol (1:1) mixture and re-dispersing them in toluene. Ligand exchange process was carried by Marcello Righetto in collaboration with the Laser Spectroscopy and Photonics group of the Chemical Department of the University of Padova.

3.7.2 Optical Spectroscopy

UV-vis spectra were recorded by using a Cary 5 spectrometer (Varian), in the range 200–800 nm. The PL spectra were measured using a FluoroMax-P (Jobin-Yvon) fluorimeter.

The UV-vis and PL spectra were performed on QDs toluene dispersions in optical quartz cuvettes with 1 mm optical path. The concentration was chosen to keep the absorbance in the range 0.5 – 1.5. The measurements were carried out in collaboration with the Laser Spectroscopy and Photonics group of the Chemical Department of the University of Padova.

3.7.3 NMR Analysis

The NMR spectra of the pristine QDs and the ligand exchanged QDs were carried out in $CDCl_3$ solutions, obtained by evaporating the toluene solutions and dissolving the QDs in the deuterated solvent. The spectra were recorded on a Bruker AVANCE 200 MHz spectrometer at 298K.

3.7.4 EPR Spectroscopy

The description of the spectroscopical apparatus is reported in chapter 2. The preparation of the samples and their EPR measurements were carried out on PCBM neat films and PCBM/S3 QDs, PCBM/S18 QDs and PCBM/N18 QDs blends. For the PCBM neat film, a 1 mg/mL solution of PCBM in oDCB was prepared and for the blends, a PCBM solution in oDCB (2mg/mL) was prepared and mixed with an equal volume of a quantum dots solution in toluene (100 μM). The final solutions were poured inside EPR quarts tubes and the solvent thoroughly removed by evaporation under vacuum. The EPR tubes were successively sealed under vacuum.

3.8 References

(1) Semonin, O. E.; Luther, J. M.; Beard, M. C. Quantum dots for next-generation photovoltaics. *Mater. Today* **2012**, *15*, 508-515.

(2) Carey, G. H.; Abdelhady, A. L.; Ning, Z.; Thon, S. M.; Bakr, O. M.; Sargent, E. H. Colloidal Quantum Dot Solar Cells. *Chem. Rev.* **2015**, *115*, 12732-12763.

(3) Jasim, K. E.: Quantum Dots Solar Cells. In *Solar Cells - New Approaches and Reviews*; InTech, 2015.

(4) Chuang, C.-H. M.; Brown, P. R.; Bulović, V.; Bawendi, M. G. Improved performance and stability in quantum dot solar cells through band alignment engineering. *Nat. mater.* **2014**, *13*, 796-801.

(5) Emin, S.; Singh, S. P.; Han, L.; Satoh, N.; Islam, A. Colloidal quantum dot solar cells. *Sol. Energy* **2011**, *85*, 1264-1282.

(6) Sargent, E. H. Colloidal quantum dot solar cells. *Nat Photon* **2012**, *6*, 133-135.

(7) Yuan, M.; Liu, M.; Sargent, E. H. Colloidal quantum dot solids for solution-processed solar cells. *Nature*, **2016**, *1*, 16016.

(8) Laquai, F.; Andrienko, D.; Deibel, C.; Neher, D.: Charge Carrier Generation, Recombination, and Extraction in Polymer–Fullerene Bulk Heterojunction Organic Solar Cells. In *Elementary Processes in Organic Photovoltaics*; Springer, 2017; pp 267-291.

(9) Lefrançois, A.; Luszczynska, B.; Pepin-Donat, B.; Lombard, C.; Bouthinon, B.; Verilhac, J.-M.; Gromova, M.; Faure-Vincent, J.; Pouget, S.; Chandezon, F.; Sadki, S.; Reiss, P. Enhanced Charge Separation in Ternary P3HT/PCBM/CuInS2 Nanocrystals Hybrid Solar Cells. *Sci. Rep.* **2015**, *5*, 7768.

(10) Borchert, H.: *Solar Cells Based on Colloidal Nanocrystals*; Springer International Publishing: Cham, 2014.

(11) Huynh, W. U.; Dittmer, J. J.; Alivisatos, A. P. Hybrid Nanorod-Polymer Solar Cells. *Science* **2002**, *295*, 2425.

(12) Mastria, R.; Rizzo, A.; Giansante, C.; Ballarini, D.; Dominici, L.; Inganäs, O.; Gigli, G. Role of Polymer in Hybrid Polymer/PbS Quantum Dot Solar Cells. *J. Phys. Chem. C* **2015**, *119*, 14972-14979.

(13) Lu, L.; Kelly, M. A.; You, W.; Yu, L. Status and prospects for ternary organic photovoltaics. *Nat Photon* **2015**, *9*, 491-500.

(14) Liao, H.-C.; Tsao, C.-S.; Lin, T.-H.; Jao, M.-H.; Chuang, C.-M.; Chang, S.-Y.; Huang, Y.-C.; Shao, Y.-T.; Chen, C.-Y.; Su, C.-J.; Jeng, U. S.; Chen, Y.-F.; Su, W.-F. Nanoparticle-Tuned Self-Organization of a Bulk Heterojunction Hybrid Solar Cell with Enhanced Performance. *ACS Nano* **2012**, *6*, 1657-1666.

(15) Martínez-Ferrero, E.; Albero, J.; Palomares, E. Materials, Nanomorphology, and Interfacial Charge Transfer Reactions in Quantum Dot/Polymer Solar Cell Devices. *JPCL* **2010**, *1*, 3039-3045.

(16) Bang, J. H.; Kamat, P. V. CdSe Quantum Dot–Fullerene Hybrid Nanocomposite for Solar Energy Conversion: Electron Transfer and Photoelectrochemistry. *ACS Nano* **2011**, *5*, 9421-9427.

(17) Stewart, M. H.; Huston, A. L.; Scott, A. M.; Oh, E.; Algar, W. R.; Deschamps, J. R.; Susumu, K.; Jain, V.; Prasuhn, D. E.; Blanco-Canosa, J.; Dawson, P. E.; Medintz, I. L. Competition between Förster Resonance Energy Transfer and Electron Transfer in Stoichiometrically Assembled Semiconductor Quantum Dot–Fullerene Conjugates. *ACS Nano* **2013**, *7*, 9489-9505.

(18) Pientka, M.; Wisch, J.; Böger, S.; Parisi, J.; Dyakonov, V.; Rogach, A.; Talapin, D.; Weller, H. Photogeneration of charge carriers in blends of conjugated polymers and semiconducting nanoparticles. *Thin Solid Films* **2004**, *451–452*, 48-53.

(19) Heinemann, M. D.; von Maydell, K.; Zutz, F.; Kolny-Olesiak, J.; Borchert, H.; Riedel, I.; Parisi, J. Photo-induced Charge Transfer and Relaxation of Persistent Charge Carriers in Polymer/Nanocrystal Composites for Applications in Hybrid Solar Cells. *Adv. Funct. Mater.* **2009**, *19*, 3788-3795.

(20) Minotto, A.; Todescato, F.; Fortunati, I.; Signorini, R.; Jasieniak, J. J.; Bozio, R. Role of Core–Shell Interfaces on Exciton Recombination in CdSe–CdxZn1–xS Quantum Dots. *J. Phys. Chem. C* **2014**, *118*, 24117-24126.

(21) Todescato, F.; Minotto, A.; Signorini, R.; Jasieniak, J. J.; Bozio, R. Investigation into the Heterostructure Interface of CdSe-Based Core–Shell Quantum Dots Using Surface-Enhanced Raman Spectroscopy. *ACS Nano* **2013**, *7*, 6649-6657.

(22) Jones, M.; Lo, S. S.; Scholes, G. D. Quantitative modeling of the role of surface traps in CdSe/CdS/ZnS nanocrystal photoluminescence decay dynamics. *Proc Natl Acad Sci* **2009**, *106*, 3011-3016.

(23) Boles, M. A.; Ling, D.; Hyeon, T.; Talapin, D. V. The surface science of nanocrystals. *Nat Mater* **2016**, *15*, 141-153.

(24) Niklas, J.; Beaupré, S.; Leclerc, M.; Xu, T.; Yu, L.; Sperlich, A.; Dyakonov, V.; Poluektov, O. G. Photoinduced Dynamics of Charge Separation: From Photosynthesis to Polymer–Fullerene Bulk Heterojunctions. *J. Phys. Chem. B* **2015**, *119*, 7407-7416.

(25) Li, C.-Z.; Chueh, C.-C.; Ding, F.; Yip, H.-L.; Liang, P.-W.; Li, X.; Jen, A. K. Y. Doping of Fullerenes via Anion-Induced Electron Transfer and Its Implication for Surfactant Facilitated High Performance Polymer Solar Cells. *Adv. Mater.* **2013**, *25*, 4425-4430.

(26) Mardis, K. L.; Webb, J. N.; Holloway, T.; Niklas, J.; Poluektov, O. G. Electronic Structure of Fullerene Acceptors in Organic Bulk-Heterojunctions: A Combined EPR and DFT Study. *JPCL* **2015**, *6*, 4730-4735.

(27) Ceuster, J. D.; Goovaerts, E.; Bouwen, A.; Hummelen, J. C.; Dyakonov, V. High-frequency (95 GHz) electron paramagnetic resonance study of the photoinduced charge transfer in conjugated polymer-fullerene composites. *Phys. Rev. B* **2001**, *64*, 195206.

(28) Witt, F.; Kruszynska, M.; Borchert, H.; Parisi, J. Charge Transfer Complexes in Organic−Inorganic Hybrid Blends for Photovoltaic Applications Investigated by Light-Induced Electron Spin Resonance Spectroscopy. *JPCL* **2010**, *1*, 2999-3003.

(29) Marcus, R. A. On the theory of oxidation-reduction reactions involving electron transfer. I. *J. Chem. Phys.* **1956**, *24*, 966-978.

(30) Nelson, J. Diffusion-limited recombination in polymer-fullerene blends and its influence on photocurrent collection. *Phys. Rev. B* **2003**, *67*, 155209.

(31) Franco, L.; Toffoletti, A.; Ruzzi, M.; Montanari, L.; Carati, C.; Bonoldi, L.; Po', R. Time-Resolved EPR of Photoinduced Excited States in a Semiconducting Polymer/PCBM Blend. *J. Phys. Chem. C* **2013**, *117*, 1554-1560.

(32) Franco, L.; Toffoletti, A.; Maggini, M. Time resolved EPR of [70]fullerene monoadducts in the photoexcited triplet state. *PCCP* **2012**, *14*, 14358-14364.

(33) Atherton, N. M.: *Principles of electron spin resonance*; Ellis Horwood, 1993.

(34) Schweiger, A.; Jeschke, G.: Principles of Pulse Electron Paramagnetic Resonance; Oxford University Press, 2001.

(35) Lanzani, G.: The Photophysics behind Photovoltaics and Photonics; Wiley, 2012.

(36) Larson, B. W.; Whitaker, J. B.; Wang, X.-B.; Popov, A. A.; Rumbles, G.; Kopidakis, N.; Strauss, S. H.; Boltalina, O. V. Electron Affinity of Phenyl–C61–Butyric Acid Methyl Ester (PCBM). *J. Phys. Chem C* **2013**, *117*, 14958-14964.

(37) Jasieniak, J.; Califano, M.; Watkins, S. E. Size-Dependent Valence and Conduction Band-Edge Energies of Semiconductor Nanocrystals. *ACS Nano* **2011**, *5*, 5888-5902.

(38) Zhu, H.; Yang, Y.; Hyeon-Deuk, K.; Califano, M.; Song, N.; Wang, Y.; Zhang, W.; Prezhdo, O. V.; Lian, T. Auger-Assisted Electron Transfer from Photoexcited Semiconductor Quantum Dots. *Nano Lett.* **2014**, *14*, 1263-1269.

(39) Wuister, S. F.; de Mello Donegá, C.; Meijerink, A. Influence of Thiol Capping on the Exciton Luminescence and Decay Kinetics of CdTe and CdSe Quantum Dots. *J. Phys. Chem. B* **2004**, *108*, 17393-17397.

(40) Chakrapani, V.; Baker, D.; Kamat, P. V. Understanding the Role of the Sulfide Redox Couple (S2–/Sn2–) in Quantum Dot-Sensitized Solar Cells. *J. Am. Chem. Soc.* **2011**, *133*, 9607-9615.

(41) Righetto, M.; Minotto, A.; Bozio, R. Bridging Energetics and Dynamics of Exciton Trapping in Core-Shell Quantum Dots. *J. Phys. Chem. C* **2016**.

(42) Choy, T. C.: *Effective Medium Theory: Principles and Applications*; Clarendon Press, 1999.

(43) Deibel, C.; Strobel, T.; Dyakonov, V. Role of the Charge Transfer State in Organic Donor–Acceptor Solar Cells. *Adv. Mater.* **2010**, *22*, 4097-4111.

(44) Shuttle, C. G.; Treat, N. D.; Douglas, J. D.; Fréchet, J. M. J.; Chabinyc, M. L. Deep Energetic Trap States in Organic Photovoltaic Devices. *Adv. Energy Mater.* **2012**, *2*, 111-119.

(45) Brabec, C. J.; Dyakonov, V.; Parisi, J.; Sariciftci, N. S.: *Organic Photovoltaics: Concepts and Realization*; Springer Berlin Heidelberg, 2003.

(46) Coropceanu, V.; Cornil, J.; da Silva Filho, D. A.; Olivier, Y.; Silbey, R.; Brédas, J.-L. Charge Transport in Organic Semiconductors. *Chem. Rev.* **2007**, *107*, 926-952.

(47) van Embden, J.; Mulvaney, P. Nucleation and Growth of CdSe Nanocrystals in a Binary Ligand System. *Langmuir* **2005**, *21*, 10226-10233.

(48) van Embden, J.; Jasieniak, J.; Mulvaney, P. Mapping the Optical Properties of CdSe/CdS Heterostructure Nanocrystals: The Effects of Core Size and Shell Thickness. *J. Am. Chem. Soc.* **2009**, *131*, 14299-14309.

(49) Fortunati, I.; Signorini, R.; Bozio, R.; Jasieniak, J. J.; Antonello, A.; Martucci, A.; Giustina, G. D.; Brusatin, G.; Guglielmi, M. CdSe Core−Shell Nanoparticles as Active Materials for Up-Converted Emission. *J. Phys. Chem. C* **2011**, *115*, 3840-3846.

CHAPTER 4.
CARBON DOTS

Carbon-based nanomaterials are currently the centre of much of the discussion in nanotechnology.[1] Among the large variety of carbon nanomaterials, Carbon Dots (CDs) received increasing interest in the last few years due to their stability, biocompatibility and remarkable photo-physical properties.[2,3] Carbon Dots are characterized by discrete, quasi-circular shapes with diameter up to 10 nm. Their structure is mainly composed by extended conjugated graphene-like domains connected together by sp^3 hybridized carbon domains. Their edges usually consist of functional groups that contain heteroatoms and that confer to CDs their optical, electronical and solubility properties. Thanks to their versatility, CDs have been considered for a lot of applications and one of the most appealing is the photovoltaics.[4] Few examples are already reported in literature.[5]

In the case of a polymer/fullerene bulk heterojunction solar cell (BHJSC) Huang et al. demonstrated that the luminescent down-shifting properties of the CD-doped polysiloxane composite raised the performance of a P3HT:PCBM cell by about 12%.[6] Liu et al. inserting a small amount of CDs in the active layer of BHJSCs demonstrated that, in addition to the luminescent down-shifting properties, CDs provide an effective interface for charge separation and efficient channels for charge transport, thus increasing solar cell photocurrent.[7] The use of CDs as active materials for organic solar cells (OSCs), particularly as electron-acceptors, was demonstrated by Gupta et al. who fabricated a P3HT/CDs device whose performances were significantly enhanced compared to the previously reported polymer/graphene cells.[8] Moreover, the electron-

accepting properties of CDs have been studied both optically, by coupling CDs with various aniline derivatives to probe the photoinduced electron transfer (PET), and computationally, by analysing the effect of porphyrin functionalization on the energy levels of CDs with the aim of developing a suitable material for the Dye Sensitized Solar Cell applications.[9,10]

Even though the electron-acceptor properties of CDs were largely studied, there are only few works in which CDs have been proposed as suitable electron-donor (ED) materials.[11,12] This property is useful for the replacement in OSCs of the semiconducting polymers. Even though the still relatively high cost of OSCs is determined both by semiconducting polymers and fullerene derivatives, the substitution of the semiconducting polymers with CDs would provide an ‘‘all-carbon’’ solar cell and a step towards the reduction of the material costs and an increase of the stability of the photovoltaic devices.

To obtain this goal it is essential to design a material whose energy levels suitably match the energy levels of the electron acceptor, the most common being the fullerene derivative PCBM.[13] Moreover, it is important to endow the CDs with a good solubility in organic solvents in order to make a more efficient film deposition step. This can be achieved thanks to the versatile CDs functionalization that allows a fine tuning of the electronic, optical, magnetic and solubility properties.[4] In particular, we decided to exploit the versatile surface chemistry of the N-doped CDs. Indeed, the amine and carboxylic surface functionalities of these materials allowed us to use a “molecular” approach to perform chemical reactions and functionalize the surface with suitable groups.[14]

In this chapter, the functionalization of N-doped CDs is reported with the aim of obtaining a material with improved solubility in organic solvents and endowed with stronger electron-donating properties. In section 4.1, the procedure for the synthesis of N-doped CDs and their functionalization with two thiophene-acetic acids (CDs-1 and CDs-2) is shown. In section 4.2, the photo-physical properties of the synthesized CDs are described. In section 4.3 the enhancement of the electron-donating properties of the CDs after the functionalization is investigated. Finally, in section 4.4 the photophysical characterization of CDs/PCBM blends regarding the photoinduced electron transfer process from CDs to PCBM is given.

4.1 SYNTHESIS

The synthesis of N-doped CDs (CDs) was performed via microwave-assisted hydrothermal protocol according to literature.[14] The details on synthesis are reported in section 4.6.1. The structure of CDs shown in Figure 4.1 was suggested by the combined use of Transmission Electron Microscopy (TEM), X-Ray Photoemission Spectroscopy (XPS), mass spectrometry and elemental analysis.[14,15] The obtained CDs are a distribution of differently sized N-doped CDs that possess different compositions and whose mean diameter is 2.4 nm.[14] The presence of amine moieties on the surface ensures an excellent solubility in water and other polar solvents. This affinity for polar solvents was a significant issue for the fabrication of PCBM/CDs films. Indeed, the active compound PCBM is soluble only in orthogonal organic less-polar solvents and the deposition of the PCBM/CDs blends combining directly N-doped CDs is hampered. To overcome this solubility issue, the chemical functionalization of the surface of N-doped CDs was carried out with the purpose of increasing CDs solubility in solvent suitable to cast PCBM films. In addition, it is well-known that functional groups on the CDs surface tend to affect also their electronical and photophysical properties. We decided to carry out the functionalization covalently linking thiophene moieties with the purpose of improving at the same time the solubility of N-doped CDs in non-polar

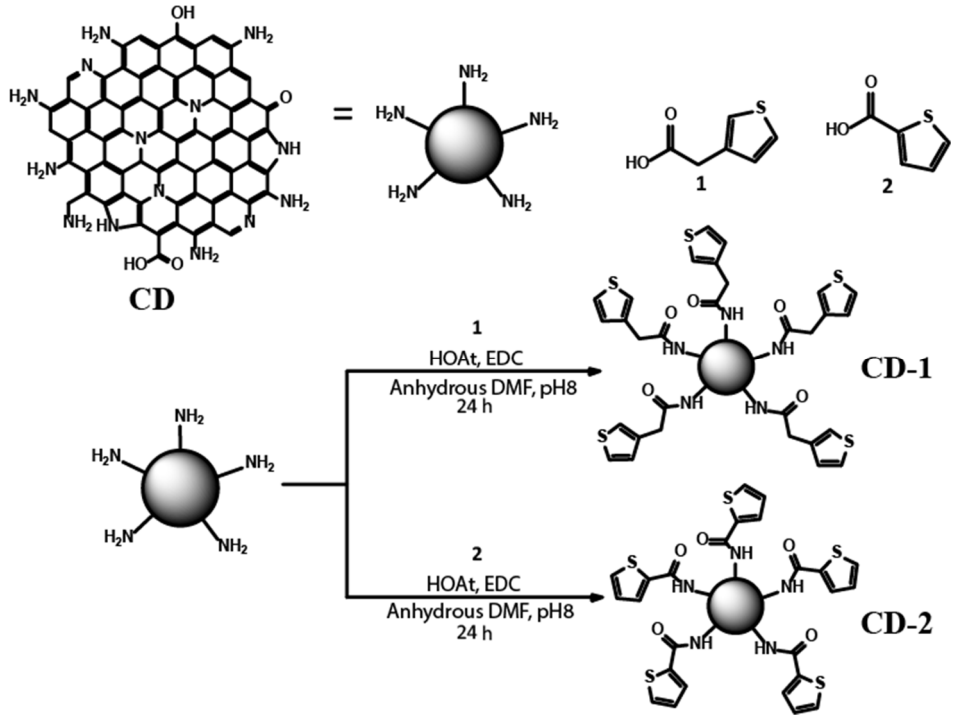

Figure 4.1 Reaction scheme of the two thiophene-functionalized N-doped CDs.

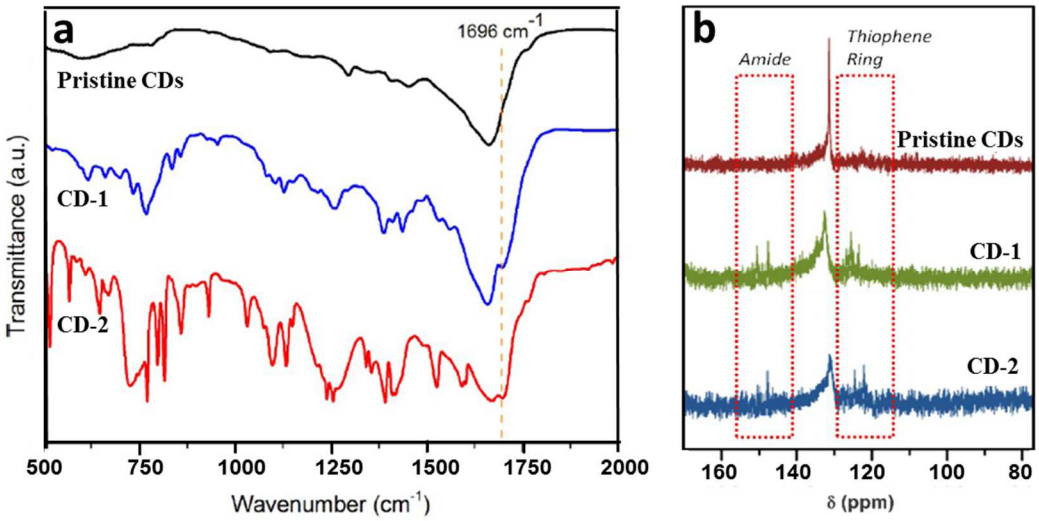

Figure 4.2 (a) FTIR spectra of pristine and functionalized CDs, (b) ^{13}C NMR spectra (DMSO) of pristine and functionalized CDs. Highlighted regions represent the amide and aromatic carbons. The main peak at 130 ppm, present in all NMR traces, is related to sp^2 carbons.

solvents and their electron-donor capabilities. Two different thiophene-derivative carboxylic acids were used (see Figure 4.1) to investigate the influence of the length of the carbon chain that separates the thiophene from the CDs on the electron transfer process from CDs to PCBM.

The confirmation of the obtained products (CDs-1 and CDs-2) came from the change in the solubility after the reaction occurred. Indeed, after the functionalization a marked enhancement in the solubility of carbon dots in oDCB was observed. At the same time the solubility in water decreased. Moreover, from the comparison of the IR spectra (Figure 4.2.a) of the functionalized CDs and the pristine ones, a significant difference was revealed. In CDs-1 and CDs-2 the presence of a band at 1696 cm^{-1}, corresponding to a carbonyl stretching, further confirms the formation of the amide bond. In addition, bands associated with thiophene ring stretching modes are visible for CDs-1 (1387 cm^{-1} and 1436 cm^{-1}) and for CDs-2 (1392 cm^{-1} and 1416 cm^{-1}). As additional structural characterization, we compared the results from elemental analysis and ^{13}C-NMR for the three carbon dots. Elemental analysis shows the presence of sulfur in CDs-1 and CDs-2 confirming the addition of thiophene moieties in these nanostructures. Finally, although these large nanosystems show very broad NMR spectra, we menaged to obtain ^{13}C-NMR of pristine CDs, CDs-1 and CDs-2. From the ^{13}C- NMR spectra (Figure 4.2.b)

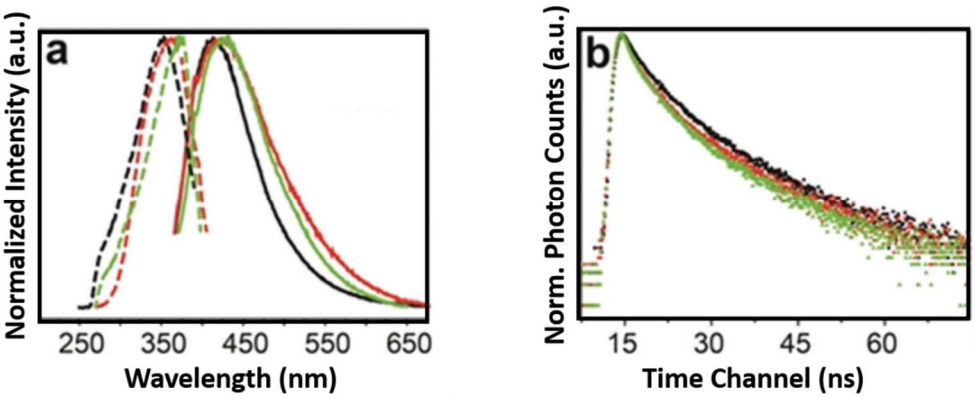

Figure 4.3 (a) Excitation spectra (dashed lines) recorded at λ_{em} = 420 nm and emission spectra (solid lines) excited at λ_{em} = 350 nm of pristine CDs (black), CDs-1 (red) and CDs-2 (green) in DMF solution. (b) Photoluminescence decay curves recorded at 450 nm under 370 nm excitation of pristine CDs (black), CDs-1 (red) and CDs-2 (green) in DMF solution.

it is possible to identify new aromatic carbons and amide carbons in the CDs-1 and CDs-2 samples.

4.2 Photophysics of Carbon Dots in solution

4.2.1 Optical Measurements

After the confirmation of the successful derivatization of N-doped CDs and the improved solubility of the functionalized CDs in low-polarity solvents, we firstly focused on the study of the photophysics of the pristine and functionalized CDs in solution with the aim of elucidating the effect of the functionalization on the electronic properties of the studied materials.

Since the absorption spectra of the three materials show broad and poorly structured bands extending into the visible region and we were mainly interested in the photoluminescence properties of CDs, we addressed our attention towards the excitation and emission spectra of pristine CDs, CDs-1 and CDs-2 in DMF (Figure 4.3). Noteworthily, the functionalization preserves the optical properties of the CDs. Both the excitation and the emission spectra and the photoluminescence decay curves of all the studied CDs are similar. According to literature and previous studies on CDs, we ascribe the excitation band peaked at 350 nm to localized surface states.[14,16,17] In particular, absorption peaks in this range are attributable to n → π* transitions of

carbonyl bonds.[18,19] This optical absorption is related to the broad and intense PL band centred at 450 nm as confirmed by the excitation spectra.

In most cases, the optical properties of carbon dots strongly depend on the solvent in which carbon dots are dispersed and on the excitation wavelength.[19,20] This behaviour is observed also in our CDs. The origin of the CDs photoluminescence is still under debate and a thorough picture is still missing.[20-23] In general, the peak photoluminescence of conventional fluorophores, such as organic dyes, is independent on the excitation wavelength since the excited states relax to the band edge state before fluorescence begins, regardless of their initial excitation energy.[24] In contrast, the photoluminescence of CDs exhibits a large red-shift with the increase of the excitation wavelength.[19] A "multi-chromophoric scaffold" architecture is widely used as a model to account for the optical properties of many CDs.[22,23] This model proposes that the absorption features of the CDs are related to their cores whereas the emission features are ascribed to the presence of many different surface states. Within this model, excitation dependent emission is attributed to exciton self-trapping in aromatic network or to surface chemical moieties. Another model associates the CDs emission properties to the broad dimensional distribution of the carbon dots generated during their synthesis.[25] Finally, a further model describes the wavelength dependence photoluminescence in the frame of the slow solvent relaxation processes that occur on the same time scales as the fluorescent emission.[19] In general, a unanimous agreement in the scientific community is still lacking.

4.2.2 Time Resolved EPR

In order to further investigate the structure and the photophysics of the synthesized CDs in solution we applied TREPR technique. Since TREPR is sensitive to paramagnetic species that are photogenerated following light absorption, we managed to probe the excited-state dynamics of those species that can hardly be investigated using photoluminescence measurements, such as triplet states.[26,27] The TREPR spectra of pristine CDs in DMF acquired using two different laser wavelengths (532 nm and 355 nm) are reported in Figure 4.4. The spectra show broad bands (about 100 mT) with an absorption-emissive character and a decay time of about 20 μs. These features are typical of molecular excited triplet states generated by Intersystem Crossing (ISC)

mechanism.[25,28,29] From best-fit spectral simulation of the TREPR spectrum acquired using 532 nm radiation (Figure 4.4.c) we obtained the zero-field splitting parameters D and E, which define the magnetic dipolar interaction between the two unpaired electrons of the triplet state.[30] The D value, related to the mean distance between the two electrons, is 1380 MHz, while E, related to the deviation of the triplet wavefunction from the axial symmetry, is 250 MHz. To have a hint of the spatial delocalization of the wavefunction of the triplet state, the D values were compared with those of aromatic or aza-aromatic systems with 4-5 condensed rings (e.g., pentacene, D=1390 MHz; porphyrin, D=1310 MHz).[31] This comparison suggests that the CDs excited triplet state is confined in only a small part of the extended CDs structure. From the size distribution of our pristine CDs, we found an average diameter of 2.4 nm. This value approximately corresponds to a mean surface area of 452.4 $Å^2$ per pristine CDs (considering a circular ring approximation). The area of an aromatic system with 5 rings is approximately 25,1 $Å^2$ which corresponds to the 5,6% of the total area of the pristine CDs. The identification of aromatic fragments within the pristine CDs is in agreement with the description of

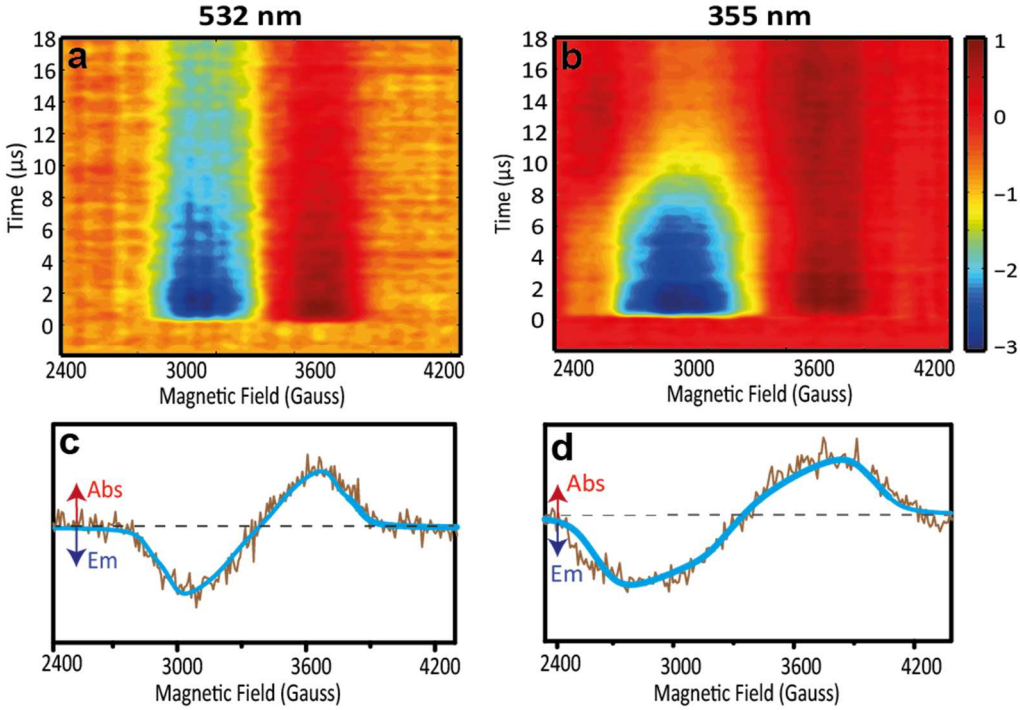

Figure 4.4 (a,b) Two dimensional TREPR spectra of pristine CDs acquired after 532 nm and 355 nm laser pulses respectively. (c,d) One dimensional TREPR spectra (brown lines) taken at 1 us after a 532 and 355 nm laser pulse respectively and best fit spectral simulations (blue lines). The measurements were performed in DMF at 130 K. Abs, absorption; Em, emission.

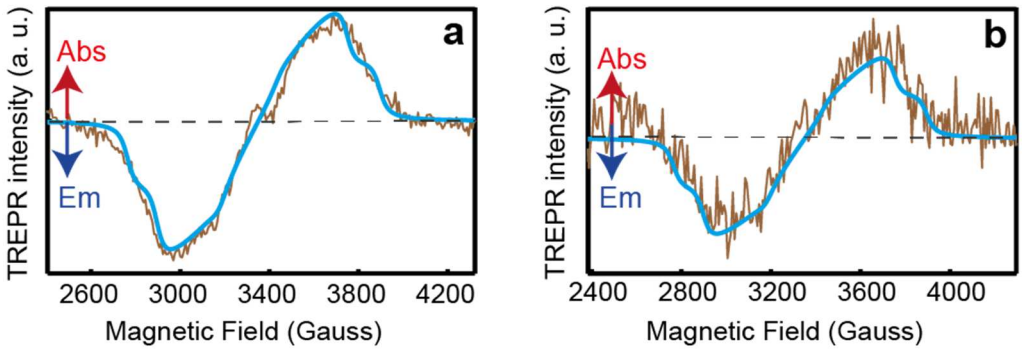

Figure 4.5 One dimensional TREPR spectra (brown lines) taken at 1 us after a 532 nm laser pulse and best fit spectral simulations (blue lines) od CDs-1 and CDs-2, respectively. The measurements were performed at 130 K. Abs, absorption; Em, emission.

CDs carbon cores suggested by Feldmann and co-workers who demonstrated the presence of polyaromatic hydrocarbon (PAH) domains embedded in a sp^3-hybridized carbon matrix.[22] The large inhomogeneous broadening observed in TREPR spectra is a possible consequence of the size and local environment heterogeneity of aromatic domains.

Remarkably, TREPR spectrum acquired using 355 nm radiation shows a photoexcited triplet signal much broader than triplet generated using 532 nm excitation (Figure 4.4.d). The simulation yields D = 2100 MHz and E = 500 MHz. These values are compatible with aromatic domains extending for about 3 unit rings. This result is compatible with the Feldmann picture and indicates that different excitation wavelengths excite different domains within the carbon dots cores.[22]

In Figure 4.5 the TREPR spectra of functionalized CDs in oDCB (a much better solvent compared to DMF) acquired after 532 nm radiation are reported. Analogously to N-doped CDs, we attribute the TREPR spectra of functionalized CDs to excited triplet states generated by ISC mechanism. From the best-fit spectral simulation, we obtained the same D and E values for both the functionalized CDs (D = 1600 MHz and E = 270 MHz). Therefore, we conclude that the different lengths of the thiopheneacetic acid moieties do not affect the triplet wavefunction. This result can be understood considering that the wavefunction of the triplet state is localized within the carbon cores of the CDs. As a consequence, slight modifications of the CDs edge affect only marginally the photophysics of the inner core. Comparing the ZFS parameters of the

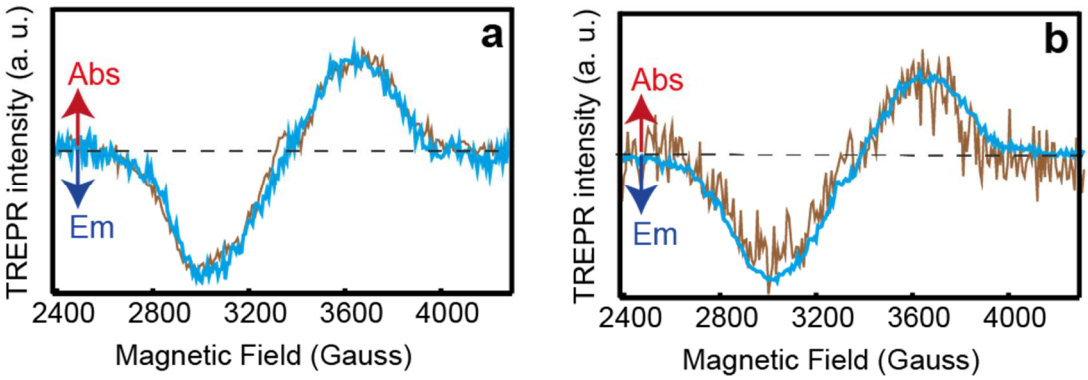

Figure 4.6 Comparison between the one dimensional TREPR spectra acquired in oDCB (brown lines) and DMF (blue lines) taken at 1 us after a 532 nm laser pulse for (a) CDs-1 and (b) CDs-2, respectively. The measurements were performed at 130 K. Abs, absorption; Em, emission.

pristine and functionalized CDs, however, an increase of the D value in CDs-1 and CDs-2 is observed. A higher D value suggests a smaller delocalization of the triplet wavefunction in the functionalized CDs and a confinement effect of the functionalization. However, the variation of the D and E values can also be attributed to the different solvents in which the measurements are carried out. In order to investigate more deeply this issue and to confirm the role of the functionalization in the excited triplet state, we recorded the TREPR spectra of CDs-1 and CDs-2 also in DMF. In Figure 4.6, the comparison between the TREPR spectra performed in oDCB (brown lines) and in DMF (blue lines) is reported. Clearly, TREPR spectra acquired in oDCB and in DMF do not show any significant difference. This result leads us to conclude that: (1) the different ZFS values of pristine CDs compared to functionalized ones must be ascribed to the functionalization effect and not to the different solvent and (2) the solvent does not influence the excited triplet state structure. In particular, the last observation further corroborates the idea that the triplet wavefunction is localized within the carbon cores.

Considering the complete picture emerging from the investigation of CDs in solution, we can conclude that TREPR spectroscopy allows to delve more deeply into the excited state structure of CDs and to unambiguously corroborate the presence of aromatic domains within an sp^3 hybridized carbon cores.

4.3 IMPROVED ELECTRON-DONOR CAPABILITIES

In order to use the thiophene-modified CDs as suitable electron donor materials towards the fullerene derivative PCBM, the energy levels of the functionalized CDs have to be suitably aligned with the energy levels of the PCBM. To probe this, the effect of the functionalization on the redox properties of CDs was investigated by cyclic voltammetry.

In Figure 4.7, the voltammetric behaviour of pristine CDs, CDs-1 and CDs-2 in DMF is reported. Cyclic voltammetry shows that the oxidation and reduction are irreversible and can be described as multielectron transfer process followed by chemical reactions.[32] Notably, the functionalization of pristine CDs results in a strong modification of their redox properties. In particular, the oxidation potentials of CDs-1 and CDs-2 are shifted to less positive potentials with respect to pristine CDs. HOMO and LUMO energy levels (E_{HOMO} and E_{LUMO}) can be estimated by CV on the basis of empirical equations derived from correlations between theoretical ionization potentials and electron affinities, and experimental redox potentials.[33] To calculate E_{HOMO} and E_{LUMO}, we relate the measured oxidation and reduction potentials to the vacuum energy level, which is assumed to be zero.

Redox potentials in non-acqueous solvents are often measured versus ferrocene/ferrocenium (Fc^+/Fc) couple and converted to E_{HOMO} and E_{LUMO} by using the following equations:[34]

$$\boldsymbol{E_{HOMO}(eV) = -e(E_{ox\ vs.Fc^+/Fc} + E^\circ{}_{Fc^+/Fc}(abs)} \qquad (1)$$

$$E_{LUMO}(eV) = -e(E_{red\ vs.Fc^+/Fc} + E^\circ{}_{Fc^+/Fc}(abs) \qquad (2)$$

where $E_{ox\ vs.Fc^+/Fc}$ and $E_{red\ vs.Fc^+/Fc}$ are the oxidation and reduction potentials of Fc^+/Fc, and $E^\circ_{Fc+/Fc}(abs)$ is the standard absolute potential (value referred to zero in a vacuum) of the Fc^+/Fc couple in DMF. E_{HOMO} and E_{LUMO} were calculated from eqn. (1) and (2) using $E^\circ_{Fc+/Fc}(abs) = 5{,}15$ V and onset potentials, $E_{on,ox}$ and $E_{on,red}$, obtained from the intersection of two tangents drawn at the rising oxidation (or reduction) current and the baseline current of the CV curves. The results are reported in Table 4.1, together with the energy levels of the pristine CDs, measured under the same conditions. The data for PCBM are reported, for comparison.[35]

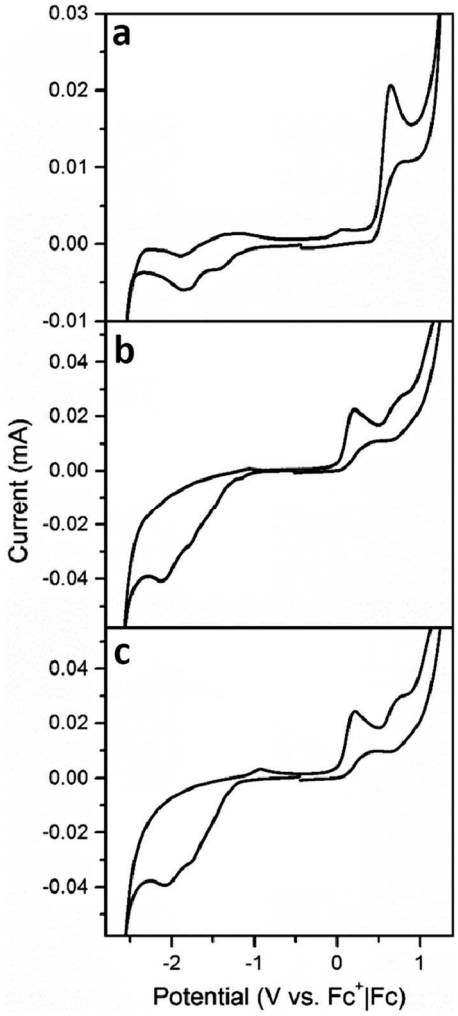

Figure 4.7 Cyclic voltammetry of (a) pristine CDs, (b) CDs-1 and (2) CDs-2 recorded on a Pt electrode at v = 0,02 Vs^{-1}, in DMF with 0,1 M Et_4NBF_4 at T = 25°C. The dotted lines show the shift of the oxidation peak towards lower oxidation potentials.

The HOMO and LUMO energy levels of CDs-1 and CDs-2 are similar and significantly differ from the energy levels of the pristine CDs. The presence of thiophene-containing groups on CDs moves up the HOMO energy level by 0.43–0.44 eV, while the LUMO level is less affected with an upward shift of 0.09–0.11 eV. Notably, LUMO energies of the functionalized CDs are higher than the LUMO energies of the fullerene derivative PCBM. This energy level matching can favour the photoinduced electron transfer from CDs to PCBM after the photoexcitation of CDs in a blend of the two materials. Alternatively, if the absorbing species is the PCBM, also a HOMO-HOMO hole transfer can occur, since the HOMO energies of the CDs are higher than the corresponding orbital energy in PCBM.

	Eon,ox (V vs. Fc+|Fc)	E_{HOMO} (eV)	Eon,red (V vs. Fc+|Fc)	E_{LUMO} (eV)	Eg (eV)
Pristine CD	0.47	-5.67	-1.16	-4.04	1.63
CD-1	0.03	-5.23	-1.25	-3.95	1.28
CD-2	0.04	-5.24	-1.27	-3.93	1.31
PCBM		-6		-4.2	1.8

Table 4.1 HOMO and LUMO energy levels derived from CV for pristine CDs, CDs-1 and CDs-2 and the calculated bandgaps.

To sum up, after the functionalization the electron-donor capabilities of the pristine CDs are increased. In addition, our CDs are expected to act as good electron donors towards the PCBM acceptor. The confirmation of this property is described in detail in the following section.

4.4 PHOTOINDUCED ELECTRON TRANSFER TO PCBM

4.4.1 PHOTOLUMINESCENCE QUENCHING

First, the interaction between the functionalized CDs and PCBM was studied in solution by means of fluorescence quenching experiments.

The results from Stern-Volmer experiments carried out using increasing PCBM concentration in toluene solution are shown in Figure 4.8. The photoluminescence intensity of CDs strongly decreases at high PCBM concentrations whereas the peak position and the shape are not affected. CDs were recently found to interact in a similar way with multi-walled carbon nanotubes (MWNTs) and graphene oxide (GO).[36] The interaction is ascribed to charge transfer process, after ruling out other possible quenching mechanisms. The Stern–Volmer analysis provides a quantitative estimation of the quenching efficiency and give some insights into the mechanism. Both CDs-1 and CDs-2 show a linear behaviour of PL quenching from PCBM at low concentrations of fullerene, and a super linear trend at higher concentrations. Typical quenching mechanisms involving the formation of ground state non-fluorescent complexes are referred to as *static*, while *dynamic* ones are those involving collisions of excited molecules.[37] However, neither the static nor the dynamic quenching mechanism allows to describe the observed super linear trend shown in Figure 4.8. Therefore, we used the "*sphere of action*'' model, which consists in an instantaneous fluorescence quenching

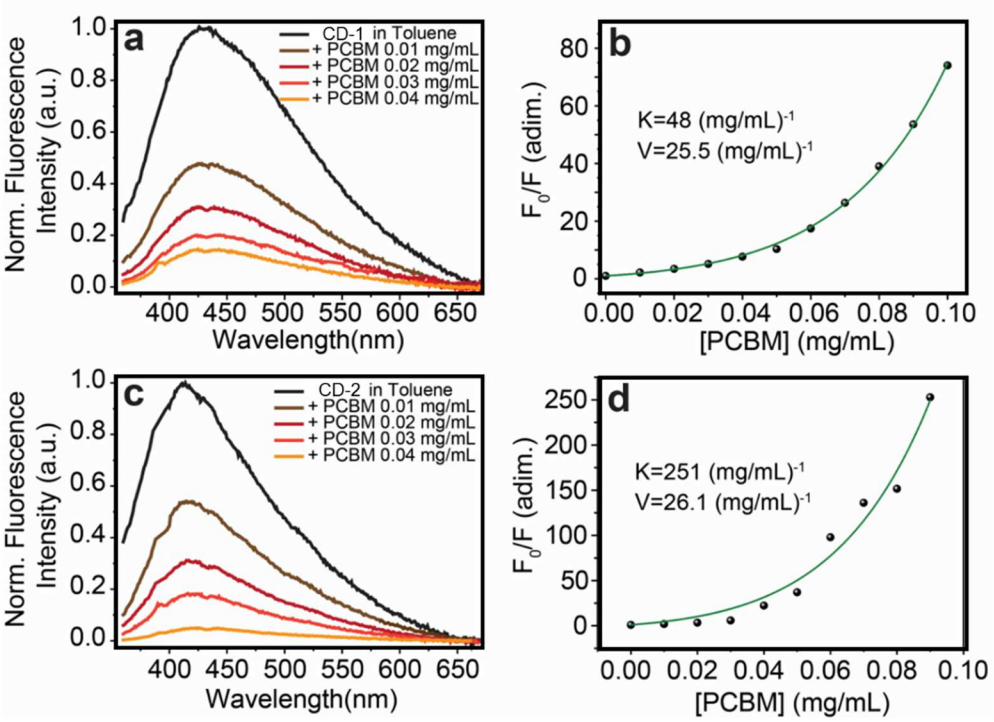

Figure 4.8 Stern-Volmer CDs fluorescence quenching experiment using PCBM as a quencher in toluene solution. (a,c) Fluorescence spectra of CDs-1 and CDs-2 in toluene solution at different PCBM concentrations and (b,d) Stern-Volmer analysis: experimental data (dots) and "sphere of action" fitting of experimental data (line). F is the integrated fluorescence intensity.

of the excited fluorophore by interaction with a sufficiently close quencher without the formation of a ground state complex.[38] Referring to literature,[37,38] the data were fitted with the following function:

$$\frac{F_0}{F} = (1 + K[PCBM])e^{V[PCBM]} \quad (3)$$

Where F_0 and F are the fluorescence intensities in the absence and in the presence of the quencher, respectively, K is the dynamic quenching constant and V is the "false" static quenching constant. The obtained V constants are similar for CDs-1 (V = 25.5 $mL \cdot mg^{-1}$) and CDs-2 (V = 26.1 $mL \cdot mg^{-1}$), indicating a similar volume of interaction with near PCBM molecules. On the other hand, a higher K constant was obtained for CDs-2 (K = 251 $mL \cdot mg^{-1}$) with respect to CDs-1 (K = 48 $mL \cdot mg^{-1}$). This result suggests that the different chain length of the thiophene-acetic groups plays an important role in determining the charge transfer interaction, perhaps by modulating the accessibility of electronic states and the wavefunction overlap.

The fluorescence quenching of CDs was observed also in PCBM/CDs blends. In this case, a complete quenching of the CDs photoluminescence was observed both in CDs-1/PCBM and CDs-2/PCBM blends. This behaviour can be considered as the extreme case for high concentrations in Stern-Volmer fluorescence quenching experiments.

4.4.2 Light Induced EPR

A further, more direct confirmation of the electron transfer interaction (ET) between CDs to PCBM comes from the Light Induced EPR (LEPR) measurements. We carried out the Light Induced EPR measurements in three different samples: CDs-1 and CDs-2 (1) in oDCB solution, (2) in film, and (3) in blend with PCBM. We chose oDCB as solvent because of the low solubility of PCBM in other solvents (e.g. DMF).

Figure 4.9 shows the LEPR spectra of CDs-1 and CDs-2 in frozen solution of oDCB at 130 K. Before light illumination no EPR signal is detected, indicating that no radical species are present in the materials. Upon light illumination, a strong light induced EPR signal appears in both the samples. The g-value, the linewidth and the microwave power saturation behaviour are typical of organic radicals. The formation of radicals after light absorption can be due to photoinduced electron transfer from the CDs to the oDCB solvent. The lineshape of both the EPR signal is reminiscent of hyperfine coupling with magnetic nuclei such as the nitrogen. The possible presence of nitrogen hyperfine couplings suggests that the observed signal can be attributed to paramagnetic species in proximity of N atoms, and therefore localized in the CDs. However, the identification of the CDs cation radical and of the oDCB anion radical is not straightforward. Indeed,

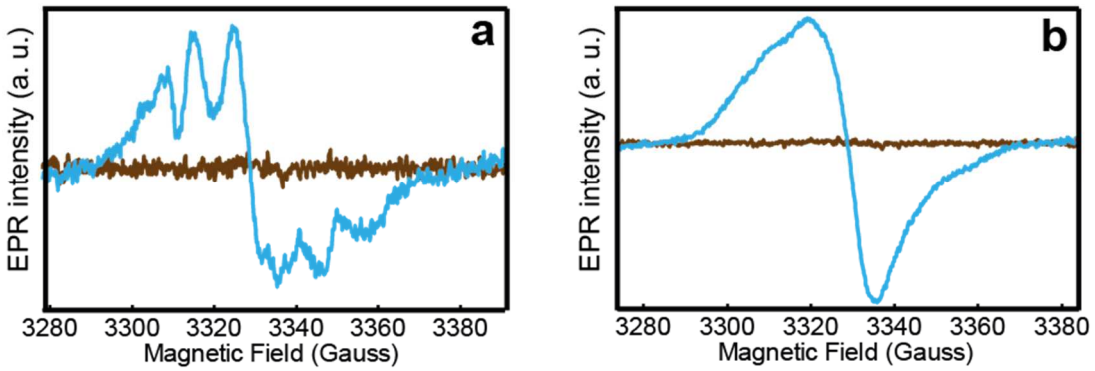

Figure 4.9 EPR spectra of (a) CDs-1 and (b) CDs-2, respectively, in oDCB acquired at 130 K. Brown lines: spectra recorded before illumination of the samples. Blue lines: spectra recorded under illumination of the samples.

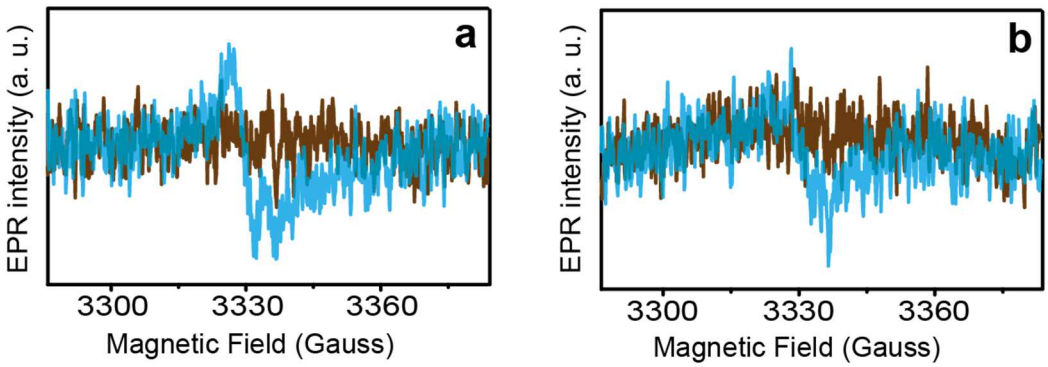

Figure 4.10 EPR spectra of (a) CDs-1 and (b) CDs-2 films, respectively, acquired at 130 K. Brown lines: spectra recorded before illumination of the samples. Blue lines: spectra recorded under white light illumination of the samples.

because of the inhomogeneity and the size distribution of CDs, the observed EPR signals could be the sum of spectra from a large variety of radical species. The observation of a photoinduced electron transfer from the CDs to the solvent molecules appear remarkable and evidences the strong electron donor capabilities of the functionalized CDs. In addition, from the EPR intensity comparison is evident that the photoinduced electron transfer is more favoured in CDs-2. This result agrees with the Stern-Volmer fitting. In particular, a shorter chain length favours the contact between the electron-donating CDs and the electron-acceptor oDCB.

In Figure 4.10, LEPR spectra of CDs-1 and CDs-2 neat films, recorded at 130 K, are reported. Also in this case, EPR spectra recorded before light illumination do not show any EPR signal. This observation demonstrates the absence of any significant paramagnetic impurity in the sample.[39] Conversely, under white light illumination of the samples, a weak EPR line, whose g value (g=2.0035±0.0005) is typical of organic radicals, is detected. We attribute this signal to long-living radicals generated by photo-induced electron transfer.[40] The linewidths are approximately 10 Gauss and the lineshapes inhomogeneously broadened possibly because of the size distribution of the CDs.[4] The detection of a small amount of photogenerated radicals in the neat CDs films demonstrates a partial double behaviour (both the electron and acceptor) of the functionalized CDs. The effect is however small and the donor type behaviour is certainly prevalent, as demonstrated in the following.

A stronger charge photogeneration is observed in the Light Induced EPR spectra of the blends of carbon dots with PCBM. In CDs-1/PCBM blends, before light illumination

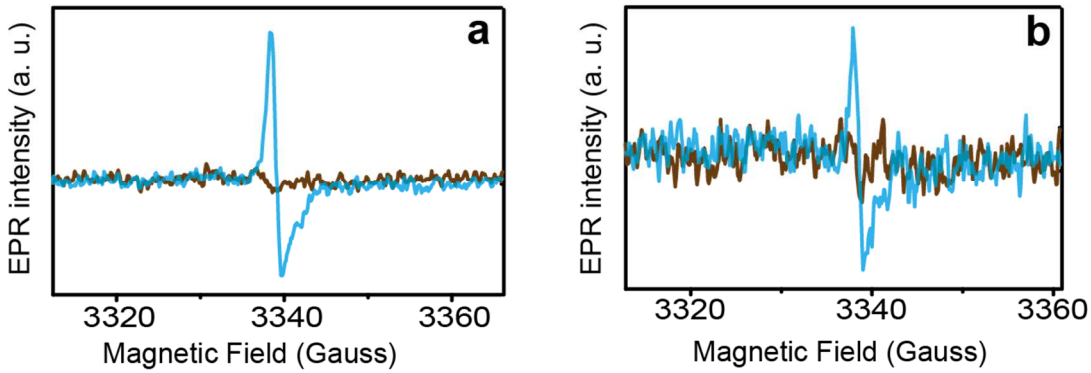

Figure 4.11 EPR spectra of (a) CDs-1/PCBM blend and (b) CDs-2/PCBM blend, respectively acquired at 130 K. Brown lines: spectra recorded before illumination of the samples. Blue lines: spectra recorded under illumination of the samples.

no EPR signal is detected (Figure 4.11.a), while under illumination a relatively strong and sharp EPR line is observed. The presence of a significant EPR signal indicates that an effective photogeneration of radicals in the blend occurs.[40] The sharp line (about 2 Gauss wide) in the spectrum is characterized by an average g-factor g = 1.9998 ± 0.0005 and an anisotropic lineshape typical of PCBM radical anion. We rationalize the presence of the PCBM anion in the blend under illumination as the result of a photoinduced electron transfer from the CDs, that behave as electron donor materials. The counterpart EPR line of the CDs-1 cation (positive polaron) is not clearly visible in the spectrum and is located at lower field with respect to the PCBM anion, at a g factor of 2.0027 ± 0.0005. There are several reasons for the low intensity of the EPR lines of CDs cation. In other donor/acceptor blends, the low intensity of the EPR signal of the radical cation was attributed to its low stability, its larger linewidth and the partial microwave saturation of the spin sublevels under the adopted experimental conditions.[28] Analogous explanations can be adopted to describe our result.

The Light Induced EPR spectrum of CDs-2/PCBM blend is shown in Figure 4.11.b. Notably, a much weaker EPR signal of the PCBM anion is observed in this blend. To rationalize this observation, either an inefficient photo-induced electron transfer or a fast recombination of the photogenerated charges can be considered. The latter explanation is supported by the fast decay (within fraction of a second) of the EPR line after switching off the illumination of the sample even at low temperatures (130 K). Conversely, in the CDs-1/PCBM blend, the decay of the strong Light Induced EPR signal is much longer, being in the order of hours at low temperatures (130 K). The

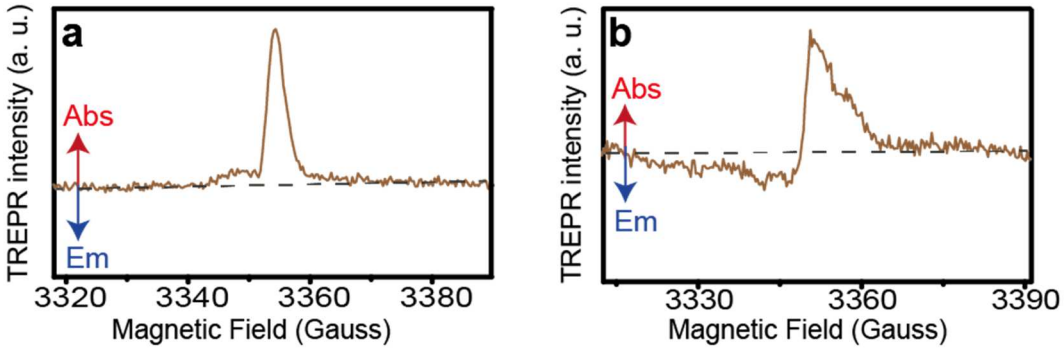

Figure 4.12 TREPR spectra recorded at 1 µs after a 532 nm, 5 ns laser pulse of (a) CDs-1/PCBM and (b) CDs-2/PCBM blends. Abs = absorption, Em = emission

faster decay in CDs-2 is possibly related to a more efficient charge recombination process, as suggested also by time-resolved experiments discussed in the following.

4.4.3 Time Resolved EPR

Having demonstrated that the CDs are acting as efficient electron-donor materials towards the PCBM, we investigated the dynamics of this process in deeper detail using time-resolved EPR (TREPR) with a sub-microsecond time resolution.

In Figure 4.12.a, the TREPR spectrum of CDs-1/PCBM blend is reported. The spectrum is composed of two peaks both in absorption. The most intense one, at higher field, possesses the same g-value and the same lineshape of the PCBM radical anion, while the less intense one, at lower field, possesses a g-value approximately similar to CDs radical cations, observed in Figure 4.10. The coincidence of the TREPR lines with the LEPR lines of CDs cation and PCBM anion leads us to conclude that no magnetic interactions between the two opposite charge carriers take place. Indeed, magnetic interactions should affect both the spectral shape and the relative intensity of the TREPR spectrum. Generally, immediately after the electron transfer the spin sublevel populations deviate from the Boltzmann equilibrium and the TREPR lines appear with a modified intensity, either in enhanced absorption or in emission. In our case, the absorptive signal of both the charge carriers suggests that a fast thermalization of the spin sublevel populations occurs after the photoinduced electron transfer probably due to a fast migration of the charge carriers.

The TREPR spectrum of CDs-2/PCBM is reported in Figure 4.12.b. In contrast with the result of CDs-1/PCBM blend, the TREPR spectrum of CDs-2/PCBM is complex and

shows peaks both in emission and in absorption. Since the overall spectral pattern is reminiscent of SCRP spectra, we attribute the TREPR spectrum to interacting charge carriers. For further details about SCRP theory, refer to Chapter 2 and literature.[41] The observation of interacting charge carriers implies a distance of less than a few nanometers between the two charges that corresponds to the distance typical of a loosely bound charge transfer (CT) state.

To sum up, generally, after the photoinduced electron transfer, a charge transfer state (interacting radicals) is generated. If the CT state lasts for a sufficiently long time, TREPR allows to detect it (Figure 4.12.b). In turn, a CT state can either recombine or separate to produce a charge separated (CS) state (distant, non-interacting radicals), as shown in Figure 4.12.a.

The different behaviour of the two blends can be rationalized in terms of a faster separation of the initial photogenerated CT state in the CDs-1/PCBM material compared to CDs-2/PCBM blend. In CDs-1/PCBM blend, we attribute the faster charge separation to a lower charge diffusion barrier due to a more favourable morphology in the material. The lower barrier of charge diffusion by hopping motion promotes the charge separation after the initial electron transfer. In CDs-2/PCBM, conversely, the initial CT state is long-living probably because of a too high barrier for charge separation. As a consequence, in CDs-2/PCBM the prolonged persistence of the two charge at a short distance is inevitably linked to a more effective geminate charge recombination which is further confirmed by the low intensity of the LEPR spectra.

4.5 CONCLUSIONS

In this chapter, the synthesis and the photophysical characterization of N-doped carbon dots (CDs) functionalized with two different thiophene-acetic acids (CDs-1 and CDs-2) was carried out. The aim of the functionalization was to increase both the electron donor capabilities of CDs and their solubility in low-polarity aromatic solvents in order to facilitate the formation of homogeneous blends with electron acceptors such as the PCBM.

The optical absorption and emission spectroscopy demonstrated that the CDs functionalization does not critically modify the absorption and emission properties of

CDs that show optical properties similar to those already reported in literature. Conversely, TREPR spectroscopy showed that aromatic domains embedded within the carbon cores are responsible for the generation of long-lived excited triplet states. In addition, the triplet state wavefunction is influenced by the presence of the functionalization that promotes a confinement effect.

The carbon dots functionalized with the thiophene units markedly change their electron donor properties. The Cyclic Voltammetry measurements demonstrated a shift of the oxidation potential after the CDs functionalization allowing a better electron donating capability towards the electron acceptor PCBM.

The PL quenching measurements in solution showed a higher quenching efficiency of PCBM towards CDs-2 with respect to CDs-1 and this effect was attributed to the less hindered contact of PCBM to CDs-2 due to the shorter chain linking the thiophene units to the carbon dots.

EPR spectroscopy, unequivocally showed an efficient photoinduced electron transfer from CDs-1 or CDs-2 to PCBM. Furthermore, using Time-Resolved EPR techniques, a different behavior was observed in the dynamics of the photogenerated charges in the two blends CDs-1/PCBM and CDs-2/PCBM. In the latter, relatively long-living charge pairs were detected whereas in the former only free charges were detected. The longer living charge pair states were suggested to be responsible for an increased charge recombination in the CDs-2/PCBM blend with respect to CDs-1/PCBM, causing a reduced yield of photoinduced free charge carriers.

4.6 EXPERIMENTAL

4.6.1 SYNTHESIS OF N-DOPED CDS

Chlorohydrated Arginine (10.2 g, 48.4 mmol) and ethylendiamine (3.56 ml, 53.3 mmol) were introduced in a 100 or 250 mL beaker containing 26.6 mL of ultrapure water. The solution was stirred at r.t. until complete dissolution of reactants and then it was irradiated in a domestic microwave oven for 4 minutes at 1000 W. During this lapse of time, white-gray aqueous vapor came out from the vents of the oven. A porous black-reddish solid was obtained and it was washed in a gooch filter with 4x20 mL aliquots of hot acetonitrile, 4x20 mL of toluene and finally 4x20 mL of diethyl ether. The solid

was dried for several minutes in air and dissolved in the minimum volume of ultrapure water to obtain a dark and turbid solution, which was filtered through a cellulose syringe filter (0.45 μm cut-off). The purified solution was freezed using a bath of acetone and solid carbon dioxide (T ≈ -78 °C) and then dried under vacuum through a lyophilization process, which brought to a brownish final compound. The synthesis was carried out by Dario Mosconi in collaboration with the Bio Organic Chemistry group of the Department of Chemical Sciences of the University of Padova.

4.6.2 Synthesis of Functionalized CDs

Anhydrous Dimethylformamide (DMF, 2 ml) was poured into a 100 mL flask equipped with a $CaCl_2$ tube. Thiophene-derived carboxylic acid (2.6 mmol) was dispersed in DMF under vigorous stirring. The mixture was cooled at 0 °C in an ice bath and 1-Hydroxy-7-azabenzotriazole (HOAt, 0.389 g, 2.86 mmol) was added. After 10 minutes that HOAt dissolved, N-(3-Dimethylaminopropyl)-N′-ethylcarbodiimide hydrochloride (EDC, 0.548 g, 2.86 mmol) was poured into the solution. Afterwards, CDs (0.150 g, corresponding to about 2.6 mmol of $–NH_2$ reactive sites) were added and the pH was adjusted to 8 using triethylamine (TEA, 0.440 ml). After 10 minutes, the ice bath was removed and the reaction was carried on at r.t. for 8 h. An additional quantity of EDC (0.274 g, 1.43 mmol) and TEA (0.440 ml) was dispersed and stirred overnight. The solvent was removed at 60°C under reduced pressure and the reaction crude was redissolved in dichloromethane. The organic phase was washed with $KHSO_4$ 10% wt/V (3 x 50 mL), deionized water (2 x 50 mL) and $NaHCO_3$ 5% wt/V (3 x 50 mL). The solution was dehydrated using Na_2SO_4 and, subsequently, dichloromethane was removed under reduced pressure. The product was dried overnight under vacuo. Elemental analysis: pristine CDs C=71.47%, H=5.05%, N=17.09% and 5.39% for residual elements, CDs-1 C=68.15%, H=3.65%, N=11.13% S=9.06 % and 8.01% for residual elements, CDs-2 C=66.05% H=3.16%, N=10.14%, S=11.47% and 9.18% for residual elements. The synthesis was carried out by Dario Mosconi in collaboration with the Bio Organic Chemistry group of the Department of Chemical Sciences of the University of Padova.

4.6.3 CYCLIC VOLTAMMETRY

CV measurements were conducted in a three-electrode cell thermostated at 25°C, using a Pt disk (2 mm diameter) and a Pt ring as working and counter electrodes, respectively, and Ag|AgI|0.1 M n-Bu_4NI as a reference electrode. The samples for CV analysis were prepared by dissolving 10 mg of CDs in 15 mL of the electrolyte solution. At the end of each experiment, ferrocene was added to the solution in order to refer the potential scale to the ferrocenium/ferrocene (Fc^+/Fc) couple. Measurements were performed using an Autolab PGSTAT 30 potentiostat/galvanostat (EcoChemie, The Netherlands) run by a PC with GPES software. CV measurements were performed by Francesca Lorandi in collaboration with the electrocatalysis and applied electrochemistry group of the Department of Chemical Sciences of the University of Padova.

4.6.4 OPTICAL SPECTROSCOPY

UV-vis absorption spectra were recorded by using a Cary 5 spectrometer (Varian), in the range 200–800 nm.

The PL spectra were measured using a FluoroMax-P (Jobin-Yvon) fluorimeter. Minimization of the scattered light was achieved by collecting the PL spectra in 90° geometry, for solution samples, and choosing the appropriate angle (30°) on the goniometer of the solid sample holder, for film samples.

Time-resolved photoluminescence (TRPL) measurements were carried out using the time-correlated single-photon counting (TCSPC) technique. The experimental apparatus is based on the Fluoromax-P detection unit (grating monochromator and photomultiplier tube), powered by the FluoroHub Single Photon Counting unit.

As for the preparation of the samples in solution, solutions were prepared keeping optical absorbance at 350 nm below 0.1 in 1 cm path quartz cuvettes. CDs films and CDs/PCBM blends were prepared by spin-coating on soda-lime (SL) microscope glass slides. SL slides were treated in basic KOH solution to improve wettability and obtain homogeneous samples.

Optical measurements were performed by Marcello Righetto in collaboration with the Laser Spectroscopy and Nanophotonics group of the Department of Chemical Sciences of the University of Padova.

4.6.5 ELECTRON PARAMAGNETIC RESONANCE

The description of EPR experimental apparatus is reported in Chapter 2. All EPR samples were examined in quartz tubes (3 mm inner diameter, 4 mm outer diameter). Three kinds of samples were studied: CDs solutions, CDs films and PCBM/CDs.

The solutions (10 mg/mL of CDs in oDCB or in DMF) were degassed in the quartz tubes through several freeze-and-pump cycles. CDs films were deposited inside the EPR tube evaporating from the above solution the solvent under vacuum. Finally, CDs/PCBM blends were prepared either by evaporating a mixed solution of the two materials (both 10 mg/mL in oDCB) inside the quartz tube under vacuum or by spin-coating a 20 mg/mL solution on a PET substrate that was cut and inserted into the EPR tube successively sealed under a N_2 atmosphere.

4.7 REFERENCES

(1) Balasubramanian, K.; Kern, K. 25th Anniversary Article: Label-Free Electrical Biodetection Using Carbon Nanostructures. *Adv. Mater.* **2014**, *26*, 1154-1175.

(2) Li, H.; Kang, Z.; Liu, Y.; Lee, S.-T. Carbon nanodots: synthesis, properties and applications. *J. Mater. Chem.* **2012**, *22*, 24230-24253.

(3) Lim, S. Y.; Shen, W.; Gao, Z. Carbon quantum dots and their applications. *Chem. Soc. Rev.* **2015**, *44*, 362-381.

(4) Wang, Y.; Hu, A. Carbon quantum dots: synthesis, properties and applications. *J. Mater. Chem. C* **2014**, *2*, 6921-6939.

(5) Essner, J. B.; Baker, G. A. The emerging roles of carbon dots in solar photovoltaics: a critical review. *Environ Sci Nano* **2017**, *4*, 1216-1263.

(6) Huang, J. J.; Zhong, Z. F.; Rong, M. Z.; Zhou, X.; Chen, X. D.; Zhang, M. Q. An easy approach of preparing strongly luminescent carbon dots and their polymer based composites for enhancing solar cell efficiency. *Carbon* **2014**, *70*, 190-198.

(7) Liu, C.; Chang, K.; Guo, W.; Li, H.; Shen, L.; Chen, W.; Yan, D. Improving charge transport property and energy transfer with carbon quantum dots in inverted polymer solar cells. *Appl. Phys. Lett.* **2014**, *105*, 073306.

(8) Gupta, V.; Chaudhary, N.; Srivastava, R.; Sharma, G. D.; Bhardwaj, R.; Chand, S. Luminscent graphene quantum dots for organic photovoltaic devices. *J. Am. Chem. Soc.* **2011**, *133*, 9960-9963.

(9) Ghosh, T.; Chatterjee, S.; Prasad, E. Photoinduced Electron Transfer from Various Aniline Derivatives to Graphene Quantum Dots. *J. Phys. Chem. A* **2015**, *119*, 11783-11790.

(10) Mandal, B.; Sarkar, S.; Sarkar, P. Theoretical Studies on Understanding the Feasibility of Porphyrin-Sensitized Graphene Quantum Dot Solar Cell. *J. Phys. Chem. C* **2015**, *119*, 3400-3407.

(11) Yu, P.; Wen, X.; Toh, Y.-R.; Lee, Y.-C.; Huang, K.-Y.; Huang, S.; Shrestha, S.; Conibeer, G.; Tang, J. Efficient electron transfer in carbon nanodot–graphene oxide nanocomposites. *J. Mater. Chem. C* **2014**, *2*, 2894.

(12) Mondal, S.; Seth, S. K.; Gupta, P.; Purkayastha, P. Ultrafast Photoinduced Electron Transfer between Carbon Nanoparticles and Cyclometalated Rhodium and Iridium Complexes. *J. Phys. Chem. C* **2015**, *119*, 25122-25128.

(13) Li, G.; Zhu, R.; Yang, Y. Polymer solar cells. *Nat Photon* **2012**, *6*, 153-161.

(14) Mosconi, D.; Mazzier, D.; Silvestrini, S.; Privitera, A.; Marega, C.; Franco, L.; Moretto, A. Synthesis and Photochemical Applications of Processable Polymers Enclosing Photoluminescent Carbon Quantum Dots. *ACS Nano* **2015**, *9*, 4156-4164.

(15) Mazzier, D.; Favaro, M.; Agnoli, S.; Silvestrini, S.; Granozzi, G.; Maggini, M.; Moretto, A. Synthesis of luminescent 3D microstructures formed by carbon quantum dots and their self-assembly properties. *Chem. Commun.* **2014**, *50*, 6592-6595.

(16) Pan, D.; Zhang, J.; Li, Z.; Wu, C.; Yan, X.; Wu, M. Observation of pH-, solvent-, spin-, and excitation-dependent blue photoluminescence from carbon nanoparticles. *Chem. Commun.* **2010**, *46*, 3681-3683.

(17) Dekaliuk, M. O.; Viagin, O.; Malyukin, Y. V.; Demchenko, A. P. Fluorescent carbon nanomaterials: "quantum dots" or nanoclusters? *PCCP* **2014**, *16*, 16075-16084.

(18) Li, B.; Guo, Y.; Iqbal, A.; Dong, Y.; Li, W.; Liu, W.; Qin, W.; Wang, Y. Insight into excitation-related luminescence properties of carbon dots: synergistic effect from photoluminescence centers in the carbon core and on the surface. *RSC Advances* **2016**, *6*, 107263-107269.

(19) Cushing, S. K.; Li, M.; Huang, F.; Wu, N. Origin of Strong Excitation Wavelength Dependent Fluorescence of Graphene Oxide. *ACS Nano* **2014**, *8*, 1002-1013.

(20) Zhu, S.; Song, Y.; Zhao, X.; Shao, J.; Zhang, J.; Yang, B. The photoluminescence mechanism in carbon dots (graphene quantum dots, carbon nanodots, and polymer dots): current state and future perspective. *Nano Res.* **2015**, *8*, 355-381.

(21) Strauss, V.; Margraf, J. T.; Dolle, C.; Butz, B.; Nacken, T. J.; Walter, J.; Bauer, W.; Peukert, W.; Spiecker, E.; Clark, T.; Guldi, D. M. Carbon Nanodots: Toward a Comprehensive Understanding of Their Photoluminescence. *J. Am. Chem. Soc.* **2014**, *136*, 17308-17316.

(22) Fu, M.; Ehrat, F.; Wang, Y.; Milowska, K. Z.; Reckmeier, C.; Rogach, A. L.; Stolarczyk, J. K.; Urban, A. S.; Feldmann, J. Carbon Dots: A Unique Fluorescent Cocktail of Polycyclic Aromatic Hydrocarbons. *Nano Lett.* **2015**, *15*, 6030-6035.

(23) Demchenko, A. P.; Dekaliuk, M. O. The origin of emissive states of carbon nanoparticles derived from ensemble-averaged and single-molecular studies. *Nanoscale* **2016**, *8*, 14057-14069.

(24) Lanzani, G.: *The Photophysics behind Photovoltaics and Photonics*; Wiley, 2012.

(25) Righetto, M.; Privitera, A.; Fortunati, I.; Mosconi, D.; Zerbetto, M.; Curri, M. L.; Corricelli, M.; Moretto, A.; Agnoli, S.; Franco, L.; Bozio, R.; Ferrante, C. Spectroscopic Insights into Carbon Dot Systems. *JPCL* **2017**, *8*, 2236-2242.

(26) Behrends, J.; Sperlich, A.; Schnegg, A.; Biskup, T.; Teutloff, C.; Lips, K.; Dyakonov, V.; Bittl, R. Direct detection of photoinduced charge transfer complexes in polymer fullerene blends. *Phys. Rev. B* **2012**, *85*, 125206.

(27) Niklas, J.; Poluektov, O. G. Charge Transfer Processes in OPV Materials as Revealed by EPR Spectroscopy. *Adv. Energy Mater.* **2017**, 1602226-n/a.

(28) Franco, L.; Toffoletti, A.; Maggini, M. Time resolved EPR of [70]fullerene monoadducts in the photoexcited triplet state. *PCCP* **2012**, *14*, 14358-14364.

(29) Franco, L.; Toffoletti, A.; Ruzzi, M.; Montanari, L.; Carati, C.; Bonoldi, L.; Po', R. Time-Resolved EPR of Photoinduced Excited States in a Semiconducting Polymer/PCBM Blend. *J. Phys. Chem. C* **2013**, *117*, 1554-1560.

(30) Hintze, C.; Steiner, U. E.; Drescher, M. Photoexcited Triplet State Kinetics Studied by Electron Paramagnetic Resonance Spectroscopy. *Chemphyschem* **2017**, *18*, 6-16.

(31) Montalti, M.; Credi, A.; Prodi, L.; Gandolfi, M. T.: *Handbook of Photochemistry, Third Edition*; CRC Press, 2006.

(32) Haram, S. K.; Quinn, B. M.; Bard, A. J. Electrochemistry of CdS Nanoparticles: A Correlation between Optical and Electrochemical Band Gaps. *J. Am. Chem. Soc.* **2001**, *123*, 8860-8861.

(33) Bredas, J. L.; Silbey, R.; Boudreaux, D. S.; Chance, R. R. Chain-length dependence of electronic and electrochemical properties of conjugated systems: polyacetylene, polyphenylene, polythiophene, and polypyrrole. *J. Am. Chem. Soc.* **1983**, *105*, 6555-6559.

(34) Cardona, C. M.; Li, W.; Kaifer, A. E.; Stockdale, D.; Bazan, G. C. Electrochemical Considerations for Determining Absolute Frontier Orbital Energy Levels of Conjugated Polymers for Solar Cell Applications. *Adv. Mater.* **2011**, *23*, 2367-2371.

(35) Thompson, B. C.; Fréchet, J. M. J. Polymer–Fullerene Composite Solar Cells. *Angew. Chem. Int. Ed.* **2008**, *47*, 58-77.

(36) Yu, P.; Wen, X.; Toh, Y.-R.; Lee, Y.-C.; Huang, K.-Y.; Huang, S.; Shrestha, S.; Conibeer, G.; Tang, J. Efficient electron transfer in carbon nanodot-graphene oxide nanocomposites. *J. Mater. Chem. C* **2014**, *2*, 2894-2901.

(37) Lakowicz, J. R.: *Principles of Fluorescence Spectroscopy*; Springer, 2007.

(38) Chris, D. G. Optical halide sensing using fluorescence quenching: theory, simulations and applications - a review. *Meas. Sci. Technol.* **2001**, *12*, R53.

(39) Camaioni, N.; Tinti, F.; Franco, L.; Fabris, M.; Toffoletti, A.; Ruzzi, M.; Montanari, L.; Bonoldi, L.; Pellegrino, A.; Calabrese, A.; Po, R. Effect of residual catalyst on solar cells made of a fluorene-thiophene-benzothiadiazole copolymer as

electron-donor: A combined electrical and photophysical study. *Org. Electron.* **2012**, *13*, 550-559.

(40) Poluektov, O. G.; Filippone, S.; Martín, N.; Sperlich, A.; Deibel, C.; Dyakonov, V. Spin Signatures of Photogenerated Radical Anions in Polymer−[70]Fullerene Bulk Heterojunctions: High Frequency Pulsed EPR Spectroscopy. *J. Phys. Chem. B* **2010**, *114*, 14426-14429.

(41) Buckley, C. D.; Hunter, D. A.; Hore, P. J.; McLauchlan, K. A. Electron spin resonance of spin-correlated radical pairs. *Chem. Phys. Lett.* **1987**, *135*, 307-312.

CHAPTER 5.

HYBRID PEROVSKITE NANOPARTICLES

Hybrid organic/inorganic perovskites have recently received a huge increase of interest due to the outstanding upsurge of their photovoltaic performances in a remarkably short time frame.[1-4] The key of this success is due to the combination of the advantages coming from the organic and the inorganic constituents. On the one hand, the organic part confers to perovskites flexibility, ease in solution processability and low-cost. On the other hand, the inorganic counterpart allows to have an excellent charge carrier mobility, a small exciton binding energy and a large absorption coefficient. In analogy with conventional semiconducting materials, the miniaturization of hybrid perovskites up to the nanometric dimension gave rise to new properties such as a higher oscillator strength, size tunability, and a high photoluminescence quantum yield (over 90%).[5-10] In addition, the synthesis of perovskite nanoparticles (PNPs) enabled additional degrees of freedom.[11,12] The control of the shape, ligands, and of the composition of the nanoparticles allows to accurately and systematically control their photophysical properties. The versatility of PNPs properties made them really promising for a lot of applications.

As demonstrated in conventional semiconductors, further properties can be triggered by coupling nanoparticles (NPs) with other organic semiconducting materials.[13] Among the various examples, nanostructured composites found a promising application in organic solar cells, where blending NPs with conducting polymers contributed toward

the enhancement of light absorption, fast exciton diffusion and dissociation as well as balanced electron/hole transport.[14-17] In addition, the knowledge of the charge photogeneration processes in solar cells allowed to optimize the photovoltaic device performances.

Despite the promising response in optoelectronic devices of inorganic NPs/organic semiconductors nanocomposites, there are only few cases of scientific reports investigating the benefits conferred by hybrid perovskite nanoparticles to the opto-electronic performances of organic semiconductors. Furthermore, in order to unravel new functionalities and new applications, it is important not only to focus the attention on the synthesis and the technological development of these materials, but also on the basic processes and interactions that take place in the mixed materials.

To reach this goal, PNPs were blended with two different organic photovoltaic materials: the fullerene derivative PCBM and the semiconducting polymer P3HT. We chose these two materials with several purposes. For the PCBM, the main purpose was to investigate the charge transfer process occurring after photoexcitation of a mixed PCBM/nanoparticle blend. In particular, following the results already described in chapter 3, the goal was to investigate the role of the ligands in the interfacial charge transfer dynamics from PNPs to PCBM. As for the P3HT, we explored the effects of PNPs on the morphology of P3HT with the aim to rationalize the peculiar interactions that occur between PNPs and the semiconducting polymer.

In section 5.1, the synthesis and the basic characterization of the $CH_3NH_3PbBr_3$ nanoparticles is shown. In section 5.2, the spectroscopic analysis carried out in PCBM/PNPs blends using both magnetic and optical spectroscopies is reported. In particular, PNPs functionalized with two different ligands, octylamine (N8) and oleylamine (N18), are examined to study the effect of the ligands on the photoinduced electron transfer (PET) process. The analysis revealed a more efficient electron transfer when a shorter ligand is used. In section 5.3, the morphological and photophysical investigation of P3HT/N8 blend is illustrated. This work demonstrated a triple influence of PNPs on the P3HT properties. First, the P3HT crystalline domains are notably increased in dimensions when blended with PNPs respect to the pristine condition. Second, a strong p-doping of the P3HT is induced by the PNPs. Third, a large area of

π-stacking between adjacent monomers of P3HT, forming H-aggregates, is generated by the presence of PNPs.

5.1 PEROVSKITE NPS SYNTHESIS AND CHARACTERIZATION

The synthesis of PNPs was performed following the ligand assisted reprecipitation (LARP) method already reported in literature.[18] Two different ligands, n-octylamine and oleylamine, were used to probe the effect of the length of the ligand on the interfacial properties of PNPs. In the following the synthesis for the PNPs with octylamine is reported (N8). An analogous procedure was carried out for N18 (nanoparticles with oleylamine) replacing n-octylamine with oleylamine.

A mixture of 0.16 mmol (8.7 mg) CH_3NH_3Br and 0.2 mmol (14.7 mg) $PbBr_2$ was dissolved in 1 mL of DMF with 4 μL of n-octylamine and 0.1 mL of oleic acid to form a clear precursor solution. DMF acts as a good solvent to dissolve the inorganic salts and organic small molecules while n-octylamine and oleic acid as co-ligands of the nanoparticles. Then, 1 mL of precursor solution was dropped under vigorous stirring into 5 mL of thermostated toluene. Different toluene temperatures were used to probe the best synthetic conditions. It turned out that a toluene temperature of 40°C allows to obtain the most stable nanoparticles. Instantaneously, after the dropping of the precursor solution into the toluene, the transparent solution turned into a yellow-green turbid solution with a blue-green photoluminescence, indicating the formation of small-sized nanoparticles but also the presence of micrometre-sized particles that confer a turbid appearance. The final solution was centrifugated at 10000 rpm for 5 min to discard the precipitates and a bright and limpid yellow solution with a strong PL was obtained.

Based on literature observations,[18] the crystallization process of the nanoparticles is controlled by the supersaturation induced by the change in solubility upon the solvent mixing. Oleic acid plays a fundamental role in suppressing the PNPs aggregation and contributes to the stability of the final solution through a charge equilibrium.

In Figure1.1.a we report the absorption and photoluminescence (PL) spectra of the as-synthesised N8 (similar spectra were obtained for N18). The PL spectrum shows a narrow-band (about 25 nm) with an emission at 520 nm. Both the absorption and the emission spectra are blue-shifted compared to that of bulk $CH_3NH_3PbBr_3$. This

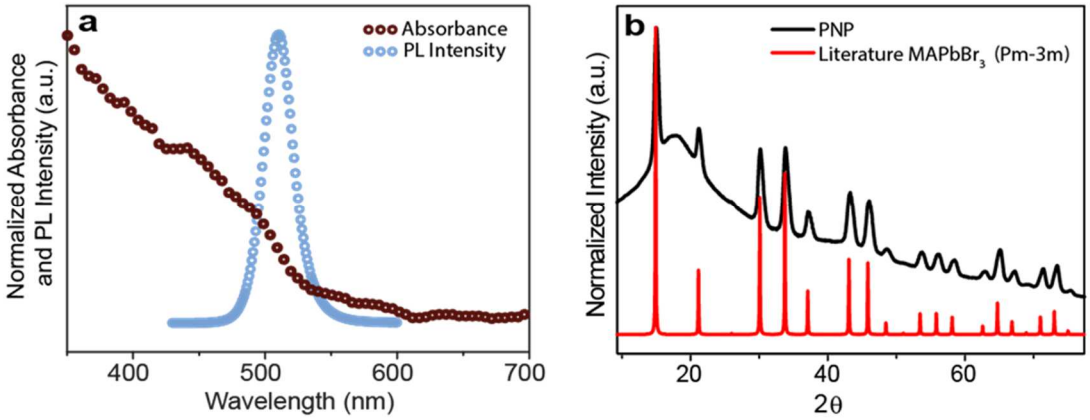

Figure 5.1 (a) Absorption (brown circles) and PL (blue circles) spectra of N8 nanoparticles in toluene solution. (b) powder XRD spectrum of N8 nanoparticles (black line) and $MAPbBr_3$ reference spectrum (red line).

evidence is a consequence of the quantum confinement effect. In addition, the sample show a small Stokes shift. According to literature,[18] this observation indicates that the PL emission of our nanoparticles originates from direct exciton recombination. Finally, the intense PL of the PNPs can be attributed both the increased binding energy of the exciton compared to bulk material and to the reduced density of defect states in the surface as a result of their good passivation due to the ligands.

In order to analyse the phase structure of PNPs, we performed the powder XRD on a drop-casted film of N8 (Figure 5.1.b). The XRD analysis shows that the sample has a well-defined three-dimensional structure that well-matches the phase (*Pm*-3*m*) of bulk $CH_3NH_3PbBr_3$.[18] The absence of broad XRD peaks typical of XRD spectra of nanoparticles can be due to the aggregation of the PNPs during the deposition process. The aggregate domains predominate in the XRD spectrum since their peaks are much sharper compared to the XRD peaks of the nanoparticles.

The surface chemical composition of the N8 was determined by X-ray Photoemission Spectroscopy (Figure 5.2). The Pb 4f photoemission line (Figure 5.2.a) shows two symmetric peaks attributed to Pb 4f7/2 and Pb 4f5/2 levels at binding energies (BE) of ca. 138.5 eV and 143.4, respectively. The deconvolution of the Pb 4f confirms that no undesired Pb oxides phases were formed.[19] A part from a negligible amount of metallic Pb (less than 2%) at 136.8 eV,[19] only one component of Pb^{2+}, which is associated to the Pb in the perovskite structure, is present. The Br 3d BE of the samples is 68.4 eV (Figure 5.2.b). Binding energies of both photoemission lines agree with the value reported in

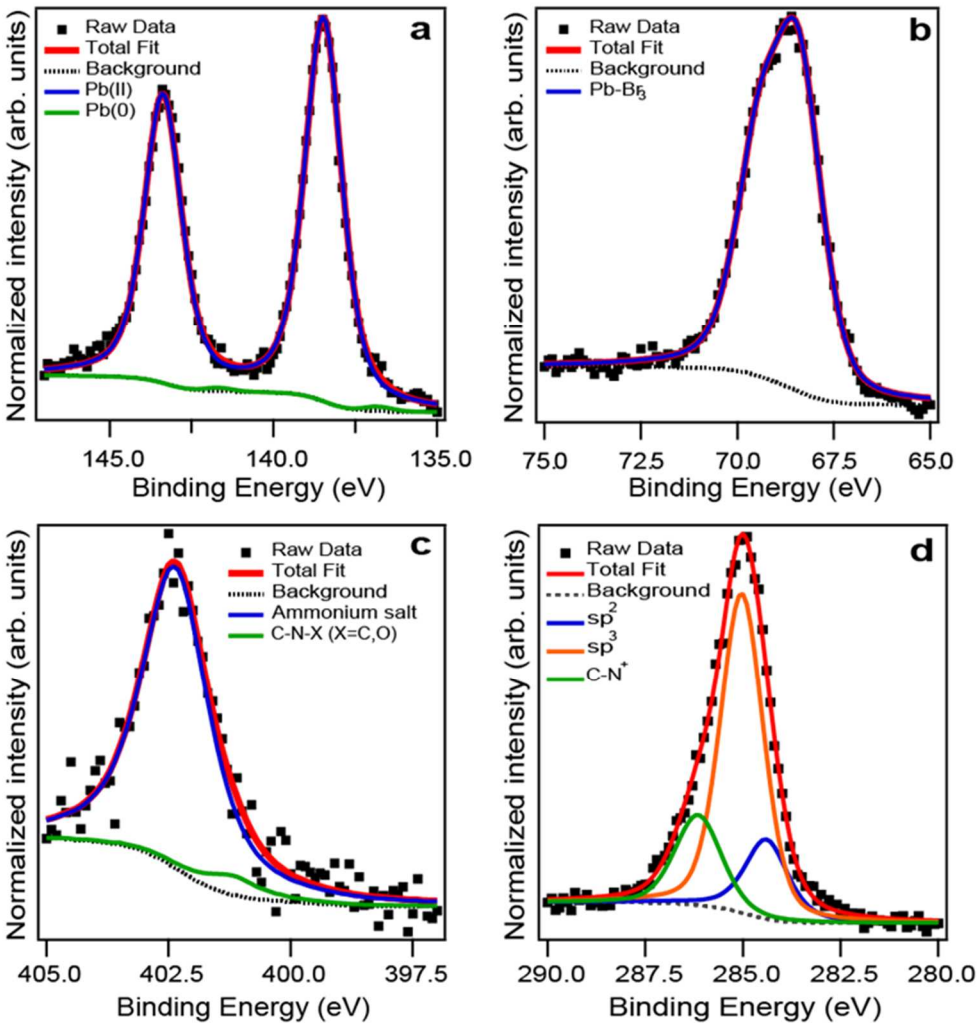

Figure 5.2 (a) Pb 4f, (b) Br 3d, (c) N 1s and (d) C 1s photoemission lines of N8 nanoparticles.

the literature.[19,20] The N 1s XPS spectra (Figure 5.2.c) show the presence of one peak at 402.3 eV corresponding to the nitrogen of the ammonium salts.[21] The main contributions to the deconvolution of the C 1s XPS spectra (Figure 5.2.d) are attributed to sp^2 and sp^3 C of the co-ligands (284.4 and 285 eV, respectively) and to C-N ligands of the ammonium salt (286.15 eV).

Finally, we performed ICP-MS analysis to measure the nanoparticles concentration in the centrifugated final N8 solution. To carry out the measurement, we poured 500 µL of the centrifugated N8 solution in a vial. After solvent evaporation, we decomposed the nanoparticles in a heated (60°C) acqueous solution (5% of HNO3 in weight). The ICP-MS analysis detected 0.733 ppm of Pb^{2+} in 500 µL of the centrifugated N8 solution. From this value, it is possible to have an estimate of the PNPs concentration.

Nevertheless, some assumptions should be taken to perform the calculation. We approximated the N8 to cubes with a side of 3.3 nm, in accordance with the literature.[18] From the calculation, we estimated a concentration of PNPs in solution of $1.66 \cdot 10^{-5}$ mol/L. Because of the rough approximations, this value allows to have only an order of magnitude estimate of the real PNPs concentration.

5.2 Perovskite Nanoparticles/PCBM Blend: Tailoring Photoinduced Electron Transfer through the Ligands

5.2.1 Optical Measurements

First, we investigated the photo-induced interactions of the synthesized PNPs with the fullerene derivative PCBM. Fluorescence spectroscopy is a well-suited technique to provide a direct evidence of this interaction. In particular, we performed Stern-Volmer analysis and time-resolved photoluminescence (TRPL) for N18 and N8 in solution, with the aim of studying the role of the ligands. In Figure 5.3.a/b we report the steady state photoluminescence (PL) quenching of N18 and N8 fluorescence by PCBM, in toluene solution. PL is progressively quenched with increasing PCBM concentrations (from 0 µM to 220 µM). N8 nanoparticles show a stronger PL quenching compared to N18. Since the literature energy level for the LUMO of PNPs ($E_{LUMO} \approx -3$ eV) is higher in energy than the LUMO of PCBM ($E_{LUMO} = -3.7$ eV), we ascribe the observed quenching to a charge transfer interaction.[22,23]

A more quantitative inspection of the quenching efficiency can be carried out through the Stern-Volmer analysis. As reported in Figure 5.3.d, the quenching ratio is reported as a function of PCBM concentration. The deviation from the linear behaviour is a signature for a complex quenching mechanism.[24] In addition, the analysis confirms that the quenching efficiency is nearly doubled passing from the long-chain capping amine (N18) to the short-chain capping one (N8).

In Figure 5.3.c we compare the PL decay in presence and in absence of PCBM quencher for both N18 and N8. PL decays are fitted with a bi-exponential model, where the short time is assigned to carrier trapping whereas the longer time to radiative recombination.[25] Remarkably, PL lifetimes for both the PNPs are nearly unchanged in presence and absence of the PCBM. This observation implies the presence of a static quenching

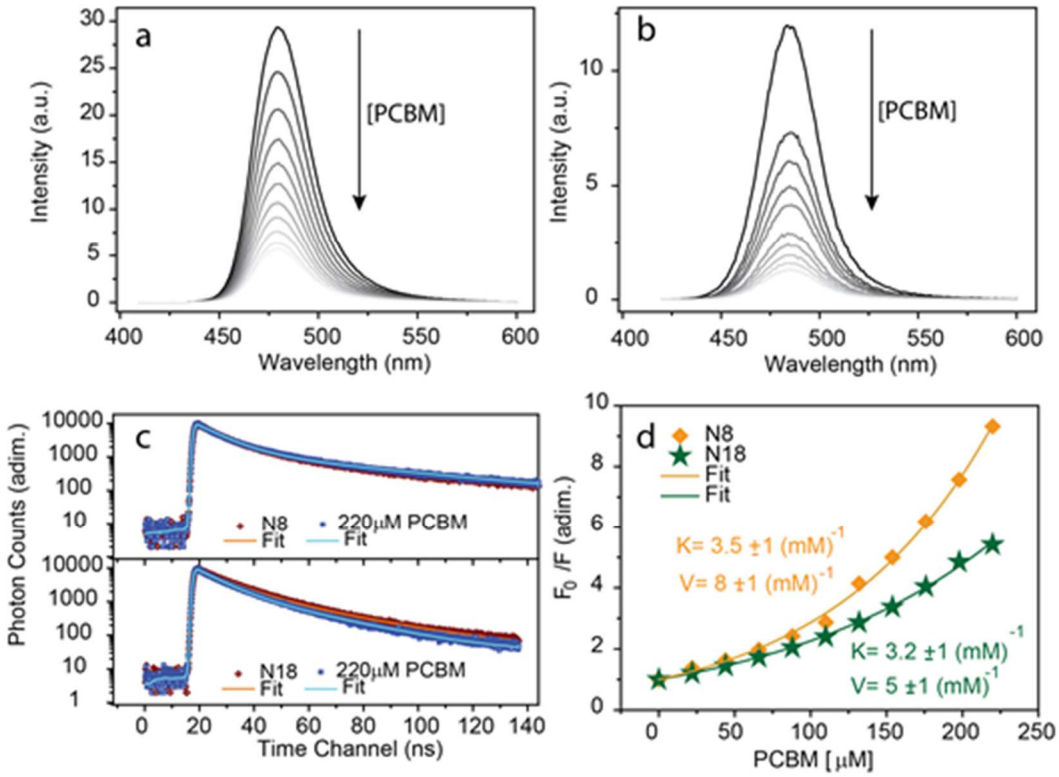

Figure 5.3 (a) Fluorescence spectra of N18 nanoparticles, under 400nm excitation, at increasing concentrations of PCBM (from 0 μM to 220 μM) (b) Fluorescence spectra of N8 nanoparticles, under 400nm excitation, at increasing concentrations of PCBM (from 0 μM to 220 μM) (c) Time resolved photoluminescence measurements of N8 and N18 nanoparticles at zero and maximum PCBM concentration, respectively. Solid lines indicate bi-exponential fitting curve. (d) Stern-Volmer plot (diamond and stars) and "sphere of action" model fitting.

mechanism or alternatively the absence of any PL quenching dynamical process operating on nanosecond timescales. In other words, PL is originated only by those nanoparticles that do not interact with PCBM, whereas the others do not emit. Ahmed recently reported a static quenching mechanism for perovskite nanospheres and TCNE.[23]

The "sphere-of-action" model coherently explains all these observations.[26] The underlying hypothesis is that proximity between donor and acceptor produces a quasi-instantaneous quenching (on observed timescales), without necessarily implying a ground-state complex formation. As Ahmed proposed, acceptor molecules are adsorbed on the nanocrystals and this explains saturation at high concentrations.

Referring to literature,[26] we fitted the Stern-Volmer points with the following function:

$$\frac{F_0}{F} = (1 + K[PCBM])e^{V[PCBM]} \quad (1)$$

Where F_0/F is the quenching ratio, K is the quenching constant and V is the "sphere-of-action" volume. The obtained quenching constants are similar in both the PNPs (see Figure 5.3.d), while the "sphere-of-action" volume appears to be higher in N8 (V_{N8}=8±1 mM^{-1}) than in N18 (V_{N18}=5±1 mM^{-1}).

Clearly, the choice of the ligand chain has a valuable effect on PL quenching of PNPs in solution. In particular, the magnitude of the net interaction in N8 increases because of the easier accessibility to the nanocrystals for the PCBM, as the increasing "sphere-of-action" volume suggests.

5.2.2 EPR MEASUREMENTS

A more direct confirmation that a photoinduced electron transfer (PET) occurs from PNPs to PCBM comes from Light Induced EPR (LEPR). The high sensitivity and selectivity of LEPR allows to study paramagnetic species (such as radical anions and cations) generated after light absorption and charge-transfer processes.[27]

We performed LEPR measurements both on the neat PCBM film, and the two PCBM/PNPs blends (PCBM/N18 and PCBM/N8). In Figure 5.4 the LEPR spectra of the studied samples are reported. Before visible light illumination, no EPR signal is revealed in all samples. This is an indication that no ground state charge transfer occurs in the blends. On the other hand, upon illumination, a sharp EPR line is detected with g factor of g=1.9997 ± 0.0005, a linewidth of $\Delta B_{pp} \approx 1$ G, and an anisotropic lineshape typical of the PCBM radical anion.[28] Therefore, we assign the acquired LEPR spectra to long-living PCBM anions formed by photoinduced electron transfer (PET).

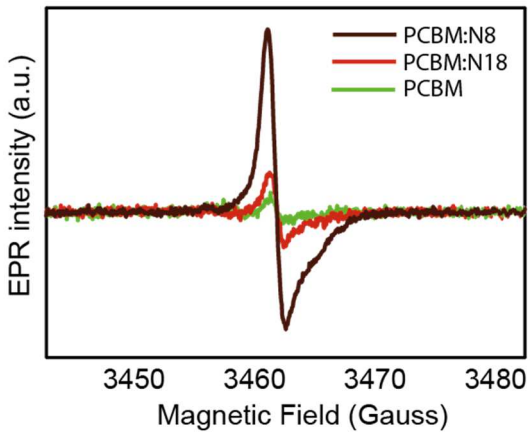

Figure 5.4 Light induced EPR spectra of the neat PCBM film and the PCBM/N18 and N8 blends acquired at 80 K.

Comparing the EPR intensities of the three PCBM anion lines, the strong photoinduced EPR signal (and therefore an efficient PET) is observed only in the PCBM/PNPs blends. We conclude that in the blends the PNPs act as effective electron donors, whereas PCBM behaves as a good electron acceptor material. On the other hand, in the neat PCBM film, the detection of only a weak PET underlines a partial double behaviour of PCBM, which acts both as electron donor and as electron acceptor. Clearly, in the blends the electron transfer is strongly promoted by the favourable energy level matching in accordance with the energy level diagram of PNPs calculated by Nair.[22] Curiously, although the PET process generates a PCBM anion and should leave a hole in the perovskite NP, in our EPR spectra we observed only the PCBM anion. This evidence was already observed in semiconducting polymer/inorganic QDs blends and was attributed to a huge EPR signal broadening due to fast electron spin relaxation times.[29,30]

In addition, the comparison of the EPR intensities of the two PNPs blends is informative of the effect of the ligand chain length on the PET process. A more intense PET in the N8 blend is observed. We explain this result, according to the Marcus theory, with a stronger electronic coupling of the nanoparticles with the PCBM.[31] Quite predictably, a shorter ligand causes a shorter average distance between the electron donor and the electron acceptor species and therefore a more favourable condition for ET process.[32] The EPR results further corroborate the proposed quenching mechanism and the increased magnitude of quenching interaction observed in Stern-Volmer analysis for N8 compared to N18.

Turning off the light illumination at 80 K, the EPR spectra do not vary significantly. This observation evidences that the photogenerated species are stable at 80K and charge recombination is hampered. At higher temperatures, after switching off the illumination, the EPR spectra decay faster and at room temperature the dark spectrum, with no EPR signal, is quickly restored. This observation indicates that a thermally activated process is dominating the charge recombination rate.[33]

Further dynamical processes of the photogenerated charges, in particular the PCBM anion, can be investigated by means of pulsed EPR measurements. Pulsed EPR techniques allows to measure T_1 and T_2 spin relaxation times from which additional information about motional dynamics and local environment of paramagnetic species can be obtained.[34] In Figure 5.5.a/b/c, we report respectively the echo detected EPR (EDEPR), and T_1 and T_2 measurements for both the neat PCBM film and the two PCBM/PNPs blends. The EDEPR spectra in Figure 5.5.b correspond to the integral of the cw EPR spectra in Figure 5.4. This evidence underlines that once again the observed

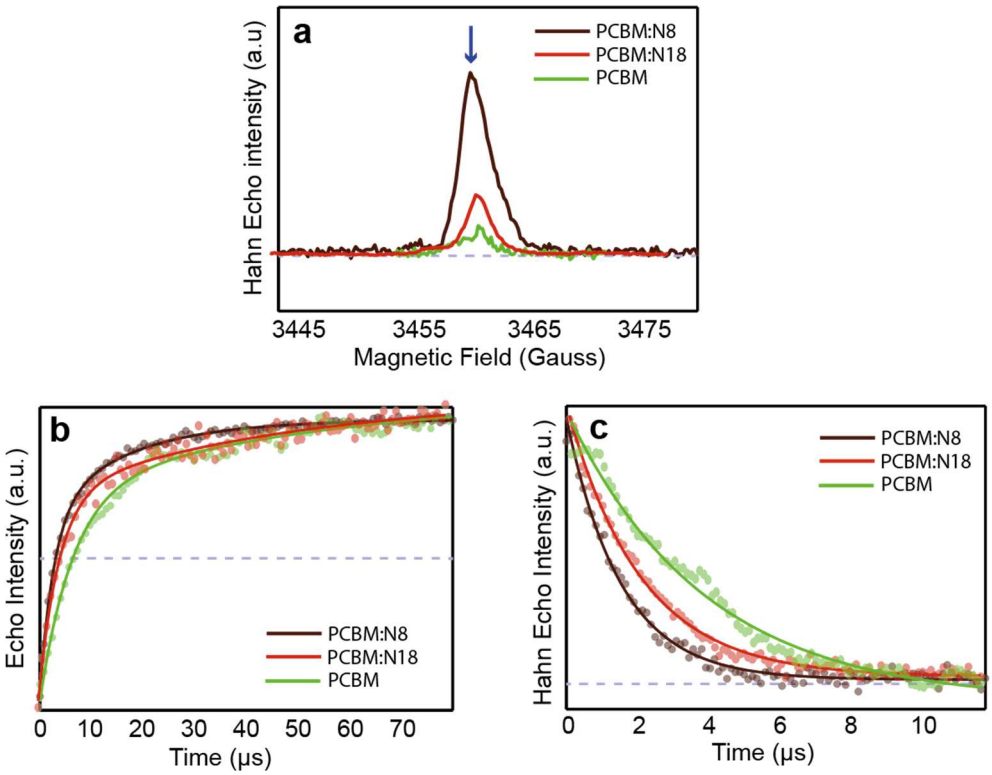

Figure 5.5 (a) Echo Detected EPR spectra of the neat PCBM film and the PCBM/N18 and N8 blends. (b,c) Inversion Recovery and Hahn echo decay experiments, for T_1 and T_2 spin relaxation times measurements (dots) and best fit curves (continuous line) of the neat PCBM film and the PCBM/N18 and N8 blends. Data are recorded at 80K under continuous white-light illumination.

	T_1 (µs)	T_2 (µs)
PCBM	6.3 (0.9) 57.0 (0.7)	5.4 (1.5)
PCBM/N18	4.0 (0.1) 50.0 (0.1)	2.14 (0.08)
PCBM/N8	2.7 (0.1) 16.0 (0.1)	1.55 (0.08)

Table 5.1 T_1 and T_2 spin relaxation times calculated from exponential best-fit of T_1 and T_2 curves in Figure 1.4.

species is the long-living anion of the PCBM. We carried out spin relaxation times measurements in correspondence of the maximum of the EDEPR spectrum, i.e. on the PCBM anion line. We performed the best fits of T_1 and T_2 curves from which the spin relaxation times have been obtained for all the samples (Table 5.1). In particular, we adopted a bi-exponential model to fit the T_1 curve and a mono-exponential one to fit the T_2 curve. Clearly, a significant decrease in the spin relaxation times of the PCBM anion in the blends with respect to the PCBM anion in the neat PCBM film is observed. Several reasons can explain the faster electron spin relaxation in the blends.[34,35] First, the increased magnetic dipolar interaction between the unpaired electron and the hydrogen nuclei of the ligand shell strongly influence the T_1 and T_2 relaxation times. Second, the spin-orbit interaction in the heavy atoms of the PNPs (Pb, Br) can play a role if the unpaired spin density of the PCBM anion partially overlaps with the PNPs electronic states. Other mechanisms could be envisaged, but regardless the specific process contributing to the electron spin relaxation, all mechanisms must assume a non-vanishing interaction between the PCBM anion and the nanoparticles or their ligand shells. This is possible only in case of a short distance between the fullerene anions and the PNPs cores and implies that the shorter the distance the faster the spin relaxation rates. These observations agree with our results since the comparison between N8 and N18 blends clearly indicates that shorter spin relaxation times are recorded at shorter ligand chain lengths. We therefore conclude that after charge photogeneration, the negative charges (PCBM anions) are trapped on average in close proximity to the nanoparticles, possibly because of electrostatic interaction with the positively charged nanoparticles.

5.3 PEROVSKITE NANOPARTICLES/P3HT BLEND: ENHANCING THE ELECTRICAL AND STRUCTURAL PROPERTIES

5.3.1 MORPHOLOGY AND ELEMENTAL ANALYSIS

Being interested not only in the interactions of the PNPs with electron acceptor molecules but also with electron donor species, we blended the PNPs with the most common photovoltaic semiconducting polymer, the P3HT. We focused our attention towards P3HT/N8 nanocomposite, elucidating both the photophysical properties and the morphology of the blend with the aim of understanding how the presence of PNPs influence the P3HT characteristics.

First, we investigated the homogeneity of the blends using SEM (Figure 5.6.a). Notably, SEM micrograph of the P3HT/N8 nanocomposite shows a uniform dispersion of the N8 in the polymer matrix with no relevant aggregation. This evidence confirms the homogeneous mixing of the composite material. In addition, the uniformity of the N8 is confirmed also by Energy Dispersive X-ray Spectroscopy (EDS). As shown in Figure 5.6.b, the distribution of Br and Pb in the sample is pretty uniform. From the EDS analysis, we obtained the Br/Pb ratio (Br/Pb = 3.5). According to the structural formula, $CH_3NH_3PbBr_3$ should have an ideal Pb/Br ratio close to 3.0.[1] However, going to the nanometric dimension the stoichiometry is modified due to the anion- or cation-rich surface. Since surface atoms occupy a large ratio in PNPs, decreasing PNPs dimensions could strongly modify the Br/Pb ratio. Following the simple model proposed in literature,[18] if the as-synthesized PNPs consist of $[PbBr6]^{4-}$ octahedron unit cells, the Br

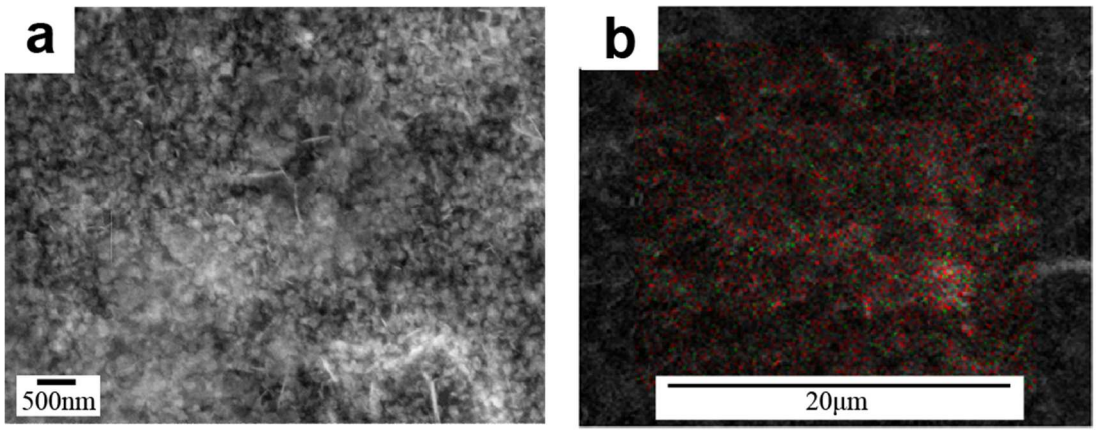

Figure 5.6 (a) SEM micrograph of a thin film of the P3HT/N8 blend drop-casted on a Si(100) wafer. (b) EDS elemental maps of an area of 20x20 µm of a thin film of the P3HT/N8 blend drop-casted on Si(100): (b) Br Lα (red) and Pb Mα (green).

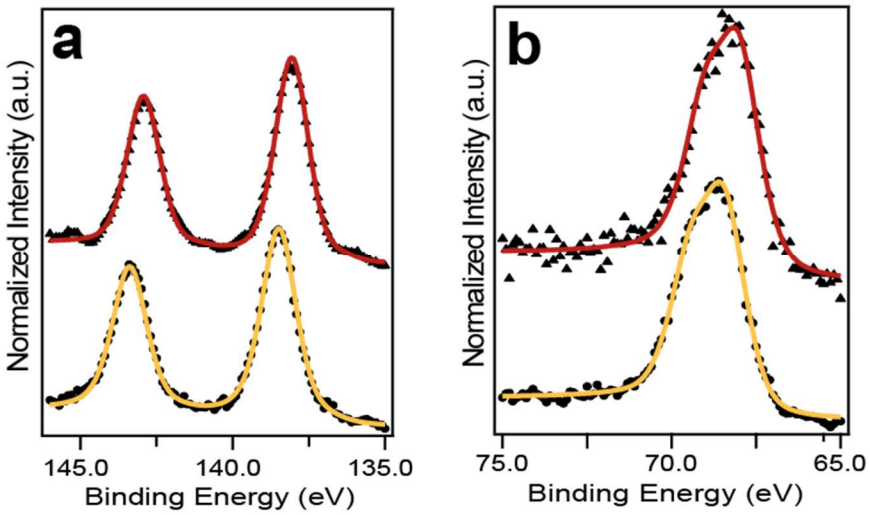

Figure 5.7 (a) Pb 4f and (b) Br 3d photoemission raw spectra and total fit of N8 (black circles, orange line) and P3HT/N8 (black triangles, red line) samples, respectively.

atoms should account for a large percentage on the surface compared with the corresponding bulk material. Notably, in the frame of this model the 3.3 nm PNPs are predicted to have a Br/Pb ratio of 3.55. This value is a further confirmation of the nanometric dimension of our N8 and allows, together with the optical absorption and PL spectra, to further corroborate the estimate of the N8 dimension.

In addition, we determined the chemical composition of the P3HT/PNPs composite by X-ray Photoemission Spectroscopy (XPS). In Figure 5.7, there is a comparison between the Pb 4f and Br 3d XPS spectra of the N8 film and the P3HT/N8 blend deposited by drop-casting on a stainless-steel substrate. Notably, from the comparison, it is evident a shift towards lower binding energies of the photoemission lines of the N8 blend: Pb 4f7/2 shift to 138.1 eV, Br 3d shift to 68 eV. An analogous shift was observed also for N 1s peak (not reported). This shift can be induced by the presence of an electronic interaction between the PNPs and the P3HT which prompted a more detailed investigation of this effect.

5.3.2 XRD DIFFRACTION

To further characterize the effect of the interaction between PNPs and the polymer, we recorded the powder X-Ray Diffraction (PXRD) patterns of the pristine P3HT and P3HT/N8 blend (Figure 5.8). The pristine P3HT shows an intense reflection at 5.4° (100) and two smaller ones at 10.6° (200) and 16.0° (300) (Figure 5.8.a). These reflections are commonly attributed to the lamellar ordering of the polymer chains induced by the π-stacking of the aromatic rings and the zipper-like connection of the alkyl side chains. Conversely, the P3HT/N8 composite shows a clearly different diffraction pattern with respect to the pristine polymer. In particular, two important differences can be noted: first, the full width at half maximum (FWHM) of the XRD peaks of the blend markedly decreases, and second, the main reflection, attributed to the P3HT matrix, shifts at lower angles, while two smaller reflections appeared at 3.3° and 8.4°. The lowering of the FWHM implies a presence of much larger crystal domains of P3HT in the blend. On the other hand, the shift of the main reflection and the appearance of other reflections in the XRD spectrum of the blend suggest a structural rearrangement of the polymer. A similar behaviour has been already reported in literature as a result of the positive doping (p-doping) of the polymer.[36,37] Indeed, a p-doping shifts the main reflection at 5.4° (corresponding to the distance between the interdigitated chains) to lower values (larger distances). This phenomenon is the effect of the oxidation: as the polymer chains get positively charged, Coulomb repulsion favours larger interchain distances. Moreover, it was also demonstrated that when the

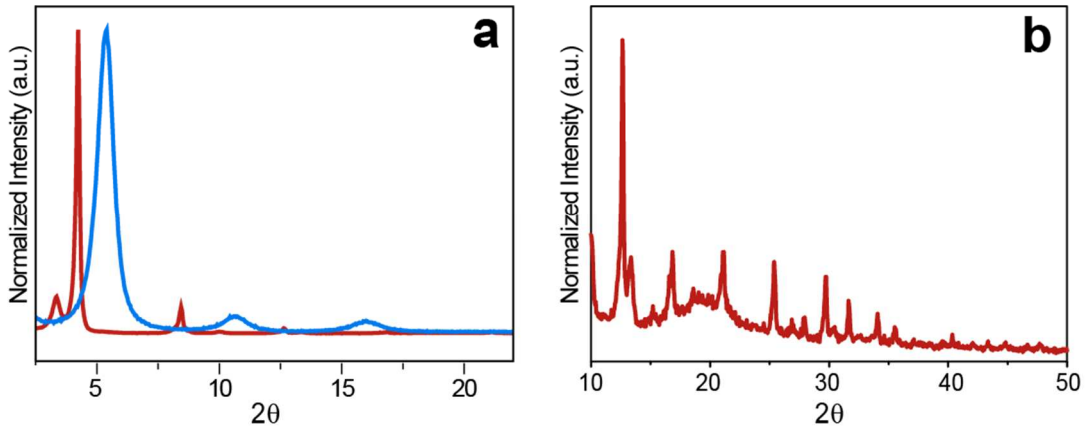

Figure 5.8 (a) Powder XRD spectra of pristine P3HT film (blue line) and P3HT/PNPs blend (red line). (b) Magnification of the 10°-50° region of the powder XRD spectrum of P3HT/PNP blend.

doping overcomes a critical threshold, P3HT can undergo a deep structural rearrangement.[38]

Magnifying the region between 10° - 50°, a series of low intense peaks is visible in the XRD spectrum of the blend (Figure 5.8.b). These low intensity peaks are associated to the dopant PNPs. Indeed, similar features for PNPs were observed in the presence of perovskite nanoplatelets.[12] Perovskite nanoplatelets are nanoparticles consisting of small stacks of perovskite layers. Analogously to PNPs, perovskite nanoplatelets are dimensionally confined and show spectrally narrow absorption features and strongly confined excitonic states. Because of their unambiguous fingerprints, we demonstrated their presence also by optical spectroscopy (described in the following). We suggest that their presence originates from the exfoliation of PNPs during the deposition process which results in the formation of mono- and bi-layered perovskite nanoplatelets in agreement with the layered nature of perovskite materials.[12]

5.3.3 CW EPR MEASUREMENTS AT 130 K

Thanks to its capability of providing structural information about the P3HT and probing the presence of paramagnetic species, such as polarons,[27,39] EPR spectroscopy was carried out with the aim of further investigating the increased crystallinity of the P3HT in blend with N8 and rationalizing the observed shift of the XPS peaks in the blend.

The normalized EPR spectra of the neat P3HT film and the P3HT/N8 blend are shown in Figure 5.9. In the neat P3HT film (Figure 5.9.a) a weak EPR peak is detected. From the spectral best-fit simulation (dotted red line) the g-tensor typical of spin 1/2 positive charge carriers (polarons) in P3HT is obtained ([2.001, 2.002, 2.003]).[39] We attribute the presence of this signal to a partial intrinsic oxidation of the polymer in air.[40] On the other hand, the EPR spectrum of P3HT/N8 blend (Figure 5.9.b) shows an intense EPR line with the same g-tensor indicating that a much stronger oxidation, i.e. a p-doping, occurred in the polymer. The p-doping of P3HT in the blend is consistent with the observed XPS shift previously discussed. We explain the excess of positive polarons on the P3HT as the result of either a thermal or a light-induced electron transfer from the P3HT to the perovskite nanoparticles. Despite the lack of a favourable alignment of the energy levels between the P3HT and the energy bands of PNPs for an efficient ground state electron transfer,[22] the pivotal role of the trap states must be considered. Indeed,

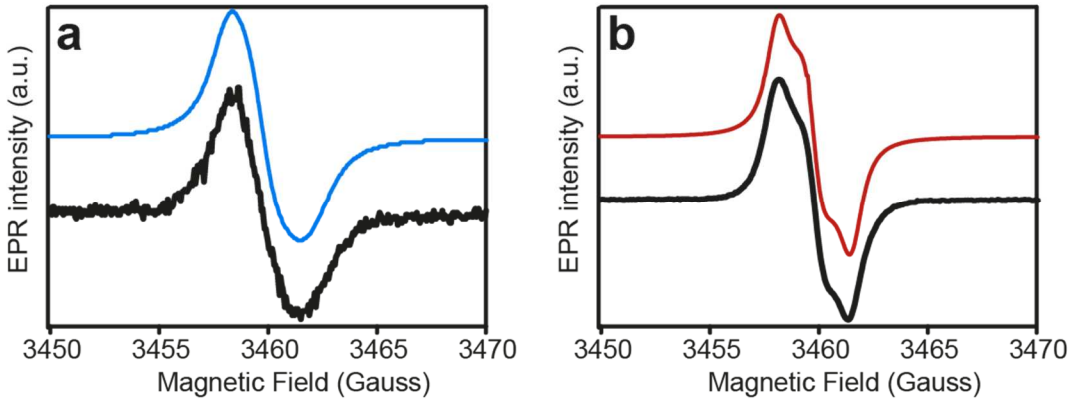

Figure 5.9 Experimental EPR spectra of (a) neat P3HT film and (b) P3HT/N8 blend (black lines) acquired at 80K and best fit spectral simulations (respectively, blue and red lines).

trap states induced by surface defects in PNPs are reported to notably affect the photophysical properties,[41,42] therefore they presence can contribute to stabilize the generated polarons In addition, the generated polarons can be stabilized by the high dielectric permittivity of the perovskite that reduces the electrostatic interactions and probably hinders the back-electron transfer process.

As well as the increased number of polarons, we observed a secondary effect induced by the presence of N8. Indeed, an anomalous EPR lineshape of the P3HT polaron, appearing much more resolved in the g-anisotropic components, can be observed in Figure 5.9.b. Two main explanations can be considered to describe this observation: first, an enhanced order degree of the P3HT chains induced by the PNPs presence, and second, a motional narrowing regime of the polarons in the blend which reduces the intrinsic linewidth.

5.3.4 CW EPR Measurements at Different Orientations

With the aim of clarifying the order degree of the polymer chains in the neat P3HT film and the P3HT/N8 blend, we performed the EPR measurements of spin-coated films at two different angles between the film plane and the magnetic field (parallel and perpendicular to the plane of the glass substrate).

In Figure 5.10, the normalized EPR spectra of the neat P3HT and P3HT/N8 films recorded at the two different orientations of the films with respect to the spectrometer magnetic field, are reported. In both the samples it was possible to observe the EPR signal of the P3HT polaron. Notably, the EPR spectra show a strong dependence on the

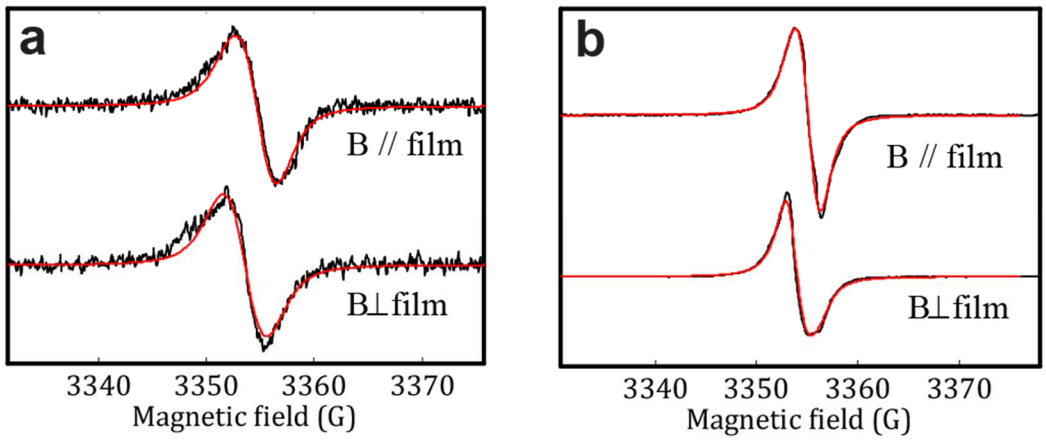

Figure 5.10 EPR spectra (black lines) of spin-coated films of (a) the neat P3HT and (b) the P3HT/N8 blend acquired at 130 K and best-fit spectral simulations (red lines). The spectra were acquired with two different orientations of the glass substrates compared to the external magnetic field. On the top, the spectra with external magnetic field parallel to the substrate plane are reported. On the bottom, the spectra with external magnetic field perpendicular to the substrate plane are reported.

film orientation. This dependence is the effect of the preferential orientation of the P3HT chains deposited on the glass substrate.

Many studies devoted to the study of P3HT morphology through EPR spectroscopy are reported in literature.[39,43] In particular, the information about the molecular order of the P3HT chains on the glass substrate are usually extracted by reproducing the angular dependence of the EPR spectra with best-fit spectral simulations that adopts a uniaxial orientational distribution function.[39] Therefore, we performed the spectral simulation of our EPR spectra (Figure 5.10.a/b) through a spectral simulation based on the following uniaxial orientational distribution function (described in detail in Appendix A):

$$p(\theta) = \frac{1}{Q} e^{-\frac{\lambda}{2}(1-3\cos^2\theta)} \qquad (2)$$

where Q is the partition function and θ defines the angle between a molecular axis (g-tensor axis) and a defined direction in the reference laboratory system (i.e. the *director*). In our case, we take the director perpendicular to the film plane. Finally, λ is called *potential coefficient* and quantifies the degree of orientation. A positive value of λ describes a preferential orientation of the molecular axis parallel to the director. Conversely a negative λ describes a molecular axis perpendicular to the director.

From the best-fit spectral simulations, we obtained in both case the g-tensor typical of P3HT polaron ([2.001, 2.002, 2.003]).[39] In addition, two similar λ values were obtained for the two samples (2.5 for P3HT and 2 for P3HT/N8 blend). This result underlines that there is no significant difference in the degree of preferential orientation of the polymer chains in the two cases. Therefore, the anomalous lineshape is not due to a different degree of orientational order but most probably to the motional narrowing regime induced by the higher mobility of polarons in the blend with respect to the neat P3HT film.

5.3.5 EPR ANALYSIS AT DIFFERENT TEMPERATURES

To corroborate our hypothesis, we acquired EPR spectra of the blend in a broad range of temperatures, from 80 K to 240 K (Figure 5.11). When the temperature is increased from 80 K to 240 K, a contraction of the EPR linewidth is observed. Nevertheless, the g-tensor anisotropy is substantially unvaried. To explain this observation, a thermally activated diffusion of the charge carriers along and between polymer chains must be considered. In particular, at higher temperatures, the charge carriers' diffusion is more favoured. A higher charge diffusion rate induces a more efficient averaging of the hyperfine broadening of EPR line (inhomogeneous broadening) and therefore a linewidth narrowing.[34] At the same time, however, if the motion of the polarons occurs within a crystalline domain, it does not necessarily result in an averaging of the g-anisotropy, since polymer chains possess all the same orientation within the same crystalline domain. Then, in presence of a high crystallinity of the sample, that allows

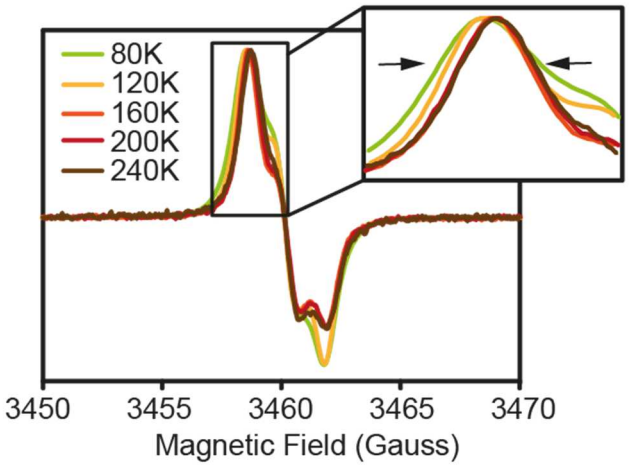

Figure 5.11 Normalized EPR spectra of P3HT/N8 blend acquired at various temperatures. The inset illustrates the narrowing of the EPR line with the temperature increase.

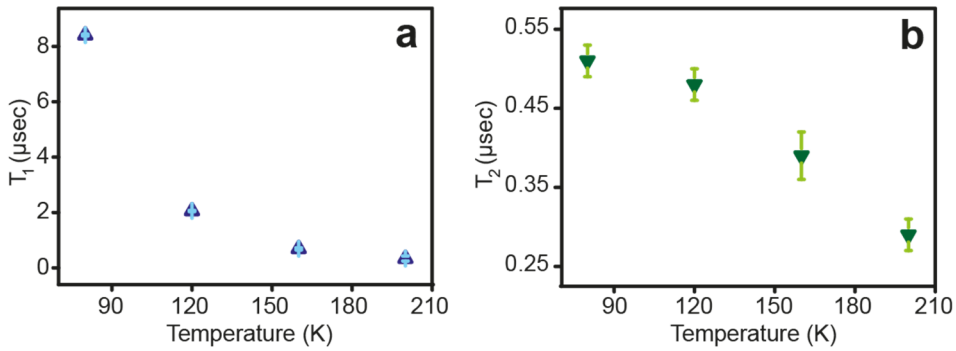

Figure 5.12 (a) T_1 and (b) T_2 spin relaxation times obtained from the exponential best-fits of T_1 and T_2 decays as a function of temperature for P3HT/N8 blend.

a high charge mobility, the resulting EPR spectrum of the polarons can show the full g-tensor anisotropy, but with a with a reduced linewidth.

Electron spin relaxation times measurements provided a further confirmation of the temperature dependent enhanced mobility of polarons in the P3HT/PNPs blend.[34] Similarly to previous section, we performed electron spin relaxation times measurements in correspondence of the maximum of the EPR spectrum of P3HT/N8 blend. From the exponential best-fits of the Inversion Recovery and Hahn echo decay curves we obtained the T_1 and T_2 decay times at various temperatures (from 80 K to 200 K). Figure 5.12 shows the plot of the obtained values for the T_1 and T_2 as a function of the temperature. From Figure 5.12, a decrease of electron spin-lattice and spin-spin relaxation times is observed as the temperature is increased. This result can be understood in the frame of the motional dynamics of the polaron. In organic systems, the electron spin relaxation is governed by local magnetic field fluctuations mainly due to dipole-dipole interactions between the unpaired electrons and between the unpaired electrons and the hydrogen nuclei. A faster charge carriers' diffusion along and between polymer chains increases the rate of the local magnetic field fluctuations that the polaron unpaired electrons experience. A higher rate of these fluctuations usually causes a decrease of the polaron spin relaxation times. Therefore, at increasing temperatures, a faster polaron diffusion lowers both electron spin-lattice and spin-spin relaxation times.

5.3.6 UV-VIS MEASUREMENTS

The polaron diffusion along and between P3HT chains is strongly influenced by the packing of the polymer chains within the crystalline domains, which in turn can be

determined by the relative orientation of transition dipoles, associated with the P3HT units. Thus, we used UV-vis spectroscopy to infer the degree of interchain order taking advantage of the coupled Frenkel excitons model developed by Spano for semiconducting polymers.[44,45] Upon deposition, interactions between monomers can be either interchain or intrachain. Hence, the competition between through-space and through-bond excitonic coupling contains information on the aggregation of P3HT. A dominant interchain coupling, associated with a high degree of interchain order, would result in co-facial H-aggregate signatures in the optical spectrum. Conversely, a dominant intrachain coupling, reflecting higher intrachain order, would result in J-aggregate signatures. These different aggregate formations lead to differences in vibronic bands intensities because of the different electronic dispersion of the molecular levels in the two cases. Therefore, the relative intensities of the vibronic bands are a sensitive probe for polymer inner structure. The ratio I_{00}/I_{01} is correlated with the degree of inter/intrachain order, in particular the lower this ratio the higher is the interchain order.

We report the UV-vis spectra recorded for pristine P3HT and P3HT/PNPs films in Figure 5.13. In the upper inset, we present the subtraction between the spectrum of P3HT with and without PNPs to magnify the differences. This subtraction reveals a redistribution of the relative intensities of the vibronic bands, associated with a microscopic ordering of the aggregated polymer. In particular, the strong decrease of I_{00} suggests an augmented interchain order. According to ref,[44,45] we quantitatively estimated the exciton bandwidth associated with H-aggregates formation, using the following relation:

$$\frac{I_{00}}{I_{01}} \approx \frac{n_{01}}{n_{00}}\left(\frac{1-0.24W/E_p}{1+0.073W/E_p}\right)^2 \qquad (2)$$

where W is the exciton bandwidth, E_p is the frequency of the coupled normal mode and n are the refractive indexes. Using parameter suggested in ref,[44] we estimated a threefold increase in the exciton bandwidth from 24 to 67 meV in the P3HT/PNPs blend. This result suggests that the presence of PNPs favours the formation of H-Aggregates within the crystalline domains.

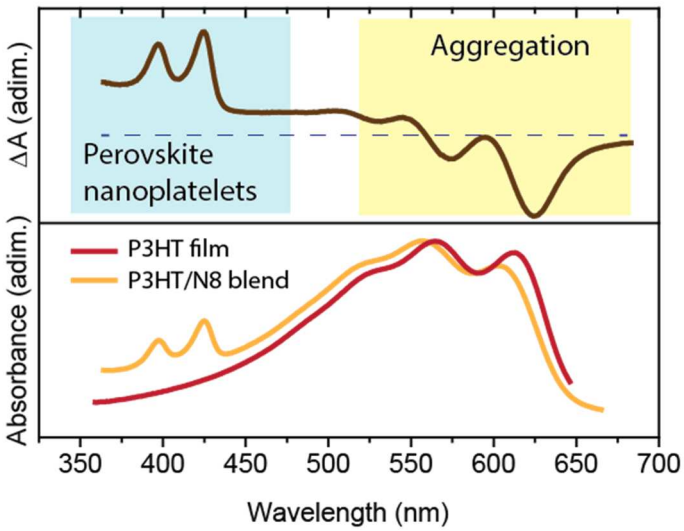

Figure 5.13 UV-vis absorption spectra of P3HT (red) and P3HT/PNPs films (orange) and their difference (brown). Changes in the vibronic structure of P3HT account for different aggregation, while appearance of novel absorption peaks on the orange absorption tail are ascribed to perovskite nanoplatelets.

Clearly, together with standard parameters (such as solvent choice and film deposition conditions), the interfacial regions between the PNPs and the P3HT rule the crystallization process of the polymer and actively modify the P3HT aggregation. We believe that the combination of the good miscibility between the two components of the blend and the nanometric size of PNPs increments the interfacial region and bolsters the formation of large crystalline domains of H-aggregates.

Finally, in addition to the enhanced H-aggregate formation, UV-vis spectrum in Figure 5.13 shows two additional peaks at shorter wavelengths. In agreement with literature and XRD analysis, we assign these peaks to perovskites nanoplatelets.[12] Indeed, in addition to the significant blue-shift due to the quantum confinement effect, nanoplatelets show also a stark change from a band-edge-like (bulk) absorption spectrum to a highly excitonic one (nanoplatelets). The sharp peak in the nanoplatelet absorption spectrum is indicative of a strong electron-hole Coulomb interaction, which results from dielectric confinement. The confirmation of the presence of perovskite nanoplatelets in the blend appears interesting because of their interesting photophysical properties that can be useful for the development of promising opto-electronic devices.

5.4 CONCLUSIONS

In this chapter, we report the synthesis of perovskite nanoparticles (PNPs) and the investigation of their interaction with two well-known organic photovoltaic materials: the electron-acceptor fullerene derivative PCBM, and the electron-donor semiconducting polymer P3HT.

Using the ligand assisted reprecipitation (LARP) method, it was possible to synthesize perovskite nanoparticles functionalized with two different ligands: oleylamine (N18) and octylamine (N8). The successful synthesis of PNPs was confirmed through the combined use of optical spectroscopy, X-ray diffraction and XPS analysis.

The as-synthesized PNPs were blended with PCBM to rationalize the contribution of the ligand length on the photoinduced electron transfer process from the PNPs to PCBM, occurring after visible light absorption. The Stern-Volmer analysis in solution revealed an efficient PNPs photoluminescence quenching induced by PCBM interpreted with the "sphere of action" quenching mechanism. A more significant quenching is observed for PNPs with the shorter ligand (N8). This effect is attributed to an easier accessibility of PCBM to the PNPs bearing shorter ligands. EPR analysis carried out in thin films unequivocally showed that the main quenching mechanism is the photoinduced electron transfer from the PNPs to the fullerene and that a more efficient electron transfer occurs in the blend with N8 nanoparticles. Finally, pulsed EPR measurements of spin relaxation times of the PCBM anion suggested the stabilization of photogenerated negative charges in proximity of PNPs.

The investigation of N8 nanoparticles blended with the semiconducting polymer P3HT revealed how the electrical and morphological properties of the polymer are influenced by the PNPs. The good miscibility between the P3HT and N8 and the optimal homogeneity of the composite was confirmed by SEM, EDS and XPS analysis. Through the combined use of X-ray diffraction (XRD), EPR spectroscopy and optical analysis, a triple contribution of the PNPs to the properties of P3HT was observed: first, an increment of the P3HT crystalline domains, second, a p-doping of the P3HT, and third, the extended formation of π-stacking between adjacent monomers of P3HT (H-aggregates).

5.5 EXPERIMENTAL

5.5.1 REAGENTS

All the following reagents were purchased from commercial suppliers and used as received without further purification. N,N dimethylformamide (DMF) (Sigma-Aldrich, anhydrous, 99.8%), toluene (Sigma-Aldrich, ≥99.5%), diethyl ether (Sigma Aldrich, ≥99.7%), methylamine (CH_3NH_2) (33% weight in absolute ethanol), lead (II) bromide ($PbBr_2$) (Sigma-Aldrich, 98%), n-octylamine (Sigma-Aldrich, 99%), oleylamine (Sigma-Aldrich, ≥70%), hydrobromic acid (HBr) (Sigma Aldrich, 48%), [6,6]-Phenyl C61 butyric acid methyl ester (PCBM) (Sigma-Aldrich, >99.5%) and poly(3-hexylthiophene-2,5-diyl) (P3HT, Sigma-Aldrich, 99.995%, average M_n 54000-75000).

5.5.2 SYNTHESIS OF CH_3NH_3Br

The preparation of methylammonium bromide was carried out following the literature.[18] A single-neck round bottom flask with methylamine in absolute ethanol was placed in a water bath at 0°C. Hydrobromic acid was slowly added dropwise in the flask under stirring and the reaction was allowed to proceed for 2 hours. Subsequently, the solvent was evaporated at 50°C and the precipitate was washed thoroughly with diethyl ether and dried.

5.5.3 THIN FILM PREPARATION

Four different materials are examined in this chapter: (1) the neat PCBM film, (2) the PCBM/PNPs blends, (3) the neat P3HT film and (4) the P3HT/PNPs blend.

For the PCBM film, a solution of PCBM (1 mg/mL) in toluene was prepared and for the PCBM/PNPs blend, 500 µL of PNPs solution in toluene were mixed with 500 µL of PCBM solution (2 mg/mL) in toluene. For the neat P3HT film, a solution of P3HT (1 mg/mL) in a mixed solvent (50% of toluene and 50% of oDCB) was prepared and for the P3HT/PNP blend, 500 µL of PNP solution in toluene were mixed with 500 µL of P3HT solution (2mg/mL) in oDCB.

The drop-casted films were prepared depositing the final solutions under inert conditions (N_2 atmosphere) on the substrates. The spin-coated films (P3HT and

P3HT/PNPs samples) were deposited starting from similar solutions but with a final P3HT concentration of 10 mg/mL.

5.5.4 OPTICAL SPECTROSCOPY

UV-vis spectra were recorded by using a Cary 5 spectrometer (Varian), in the range 200–800 nm. The PL spectra were measured using a FluoroMax-P (Jobin-Yvon) fluorimeter.

Photoluminescence spectra were measured with a FluoroMax-P (Jobin-Yvon) fluorimeter. All reported spectra were corrected for scattering effects by a calibration curve. Transient photoluminescence (TRPL) measurements were carried out using the time-correlated single photon counting (TCSPC) technique. The experimental setup exploits the Fluoromax-P detection unit (grating monochromator and photomultiplier tube), integrated with a FluoroHub Single Photon Counting unit. Chosen excitation source was a blue (370±15nm) pulsed Horiba NanoLED, generating 1 ns pulses at 1MHz repetition rate.

For Stern-Volmer measurements, solutions were prepared keeping optical absorbance at 370 nm below 0.1 in 1 cm path quartz cuvettes. Quenching experiments were performed by adding small volumes (20 uL – 200 uL) of a concentrated PCBM solution (2 mg/mL) to identical perovskite nanoparticles solutions. Film samples were deposited by spin-coating on microscope cover glass substrates.

Optical measurements were performed by Marcello Righetto in collaboration with the Laser spectroscopy and Nanophotonics group of the Department of Chemical Sciences of the University of Padova.

5.5.5 SEM AND EDS ANALYSIS

The micro-scale morphology of materials was studied by scanning electron microscopy (SEM). SEM micrographs were acquired using a field emission source equipped with a GEMINI column (Zeiss Supra VP35 and were obtained with an acceleration voltage of 5 kV using secondary electron detector. Energy Dispersive X-ray Spectroscopy (EDS) elemental maps were acquired with the same instrument. For sample preparation, the solutions were deposited on Si(100) wafer by drop-casting.

SEM and EDS analysis was performed by Francesco Carraro in collaboration with the Surfaces and Catalysts group of the Department of Chemical Sciences of the University of Padova.

5.5.6 X-RAY PHOTOEMISSION SPECTROSCOPY

X-ray Photoelectron Spectroscopy (XPS) spectra were collected in an Ultra High Vacuum chamber equipped with a EA 125 Omicrom electron analyzer. Core level photoemission spectra (C 1s, N 1s, O 1s, S 2p, Br 3d and Pb 4f regions) were collected at room temperature in normal emission with a non-monochromatized Al Kα X-ray source (hv=1486.6 eV) using 0.1 eV steps, 0.5 s collection time, and 20 eV pass energy. The studied samples were drop casted on stainless steel substrates. After drying under nitrogen atmosphere, the obtained films were introduced into the ultrahigh vacuum chamber and outgassed overnight.

XPS analysis was performed by Francesco Carraro in collaboration with the Surfaces and Catalysts group of the Department of Chemical Sciences of the University of Padova.

5.5.7 POWDER X-RAY DIFFRACTION (PXRD)

PXRD patterns of the nanoparticles were acquired with a with an Oxford Diffraction Gemini E diffractometer, equipped with a 2K × 2K EOS CCD area detector and sealed–tube Enhance (Mo) and (Cu) X–ray sources. Cu Kα (λ = 1.54184 Å) radiation was used. The diffractometer even if built for single crystals allows also powder data collection. A low amount of nanoparticles (few mg) were fastened on the external wall of a glass capillary by means of Paratone oil.

PXRD patterns of the pristine P3HT and the P3HT/PNPs blend were collected with a Bruker D8 Advance diffractometer in Bragg–Brentano geometry equipped with a Göbel mirror using Cu Kα as source operating at 40 kV and 40 mA. The studied samples were deposited on Si(100) wafer by drop-casting. PXRD analysis was performed by Dr. Marzio Rancan in collaboration with the Molecular Materials and Modeling group of the Department of Chemical Sciences of the University of Padova.

5.5.8 EPR SPECTROSCOPY

The description of the EPR instrumentation is reported in chapter 2.

For films preparation, 200 μL of the various solutions were put in quartz EPR tubes (4mm outer diameter) and the solvent was removed under vacuum. Finally, the tubes were flame-sealed under vacuum to avoid the presence of oxygen.

For spin coated film preparation, the solutions were spin-coated on microscope cover glass substrates (Brand microscope cover glasses, 18x18x0.15 mm) that were subsequently cut in 18x2 mm sections and inserted within the EPR tubes. Afterwards, tubes were flame-sealed under N_2 atmosphere.

5.6 REFERENCES

(1) Brenner, T. M.; Egger, D. A.; Kronik, L.; Hodes, G.; Cahen, D. Hybrid organic—inorganic perovskites: low-cost semiconductors with intriguing charge-transport properties. *Nat. Rev. Mater.* **2016**, *1*, 15007.

(2) Zhao, Y.; Zhu, K. Organic-inorganic hybrid lead halide perovskites for optoelectronic and electronic applications. *Chem. Soc. Rev.* **2016**, *45*, 655-689.

(3) Shi, Z.; Guo, J.; Chen, Y.; Li, Q.; Pan, Y.; Zhang, H.; Xia, Y.; Huang, W. Lead-Free Organic–Inorganic Hybrid Perovskites for Photovoltaic Applications: Recent Advances and Perspectives. *Adv. Mater.* **2017**, *29*, 1605005.

(4) Chen, Q.; De Marco, N.; Yang, Y.; Song, T.-B.; Chen, C.-C.; Zhao, H.; Hong, Z.; Zhou, H.; Yang, Y. Under the spotlight: The organic–inorganic hybrid halide perovskite for optoelectronic applications. *Nano Today* **2015**, *10*, 355-396.

(5) González-Carrero, S.; Galian, R. E.; Pérez-Prieto, J. Organometal Halide Perovskites: Bulk Low-Dimension Materials and Nanoparticles. *Particle & Particle Systems Characterization* **2015**, *32*, 709-720.

(6) Gonzalez-Carrero, S.; Galian, R. E.; Pérez-Prieto, J. Organic-inorganic and all-inorganic lead halide nanoparticles. *Opt. Express* **2016**, *24*, A285-A301.

(7) Luo, B.; Pu, Y.-C.; Yang, Y.; Lindley, S. A.; Abdelmageed, G.; Ashry, H.; Li, Y.; Li, X.; Zhang, J. Z. Synthesis, Optical Properties, and Exciton Dynamics of Organolead Bromide Perovskite Nanocrystals. *J. Phys. Chem. C* **2015**, *119*, 26672-26682.

(8) Zheng, K.; Žídek, K.; Abdellah, M.; Messing, M. E.; Al-Marri, M. J.; Pullerits, T. Trap States and Their Dynamics in Organometal Halide Perovskite Nanoparticles and Bulk Crystals. *J. Phys. Chem. C* **2016**, *120*, 3077-3084.

(9) Schmidt, L. C.; Pertegás, A.; González-Carrero, S.; Malinkiewicz, O.; Agouram, S.; Mínguez Espallargas, G.; Bolink, H. J.; Galian, R. E.; Pérez-Prieto, J. Nontemplate Synthesis of CH3NH3PbBr3 Perovskite Nanoparticles. *J. Am. Chem. Soc.* **2014**, *136*, 850-853.

(10) Mittal, M.; Jana, A.; Sarkar, S.; Mahadevan, P.; Sapra, S. Size of the Organic Cation Tunes the Band Gap of Colloidal Organolead Bromide Perovskite Nanocrystals. *JPCL* **2016**, *7*, 3270-3277.

(11) Luo, B.; Pu, Y.-C.; Lindley, S. A.; Yang, Y.; Lu, L.; Li, Y.; Li, X.; Zhang, J. Z. Organolead Halide Perovskite Nanocrystals: Branched Capping Ligands Control Crystal Size and Stability. *Angew. Chem. Int. Ed.* **2016**, *55*, 8864-8868.

(12) Weidman, M. C.; Seitz, M.; Stranks, S. D.; Tisdale, W. A. Highly Tunable Colloidal Perovskite Nanoplatelets through Variable Cation, Metal, and Halide Composition. *ACS Nano* **2016**, *10*, 7830-7839.

(13) Saini, P.: *Fundamentals of Conjugated Polymer Blends, Copolymers and Composites: Synthesis, Properties, and Applications*; Wiley, 2015.

(14) Carey, G. H.; Abdelhady, A. L.; Ning, Z.; Thon, S. M.; Bakr, O. M.; Sargent, E. H. Colloidal Quantum Dot Solar Cells. *Chem. Rev.* **2015**, *115*, 12732-12763.

(15) Kamat, P. V. Quantum Dot Solar Cells. Semiconductor Nanocrystals as Light Harvesters. *J. Phys. Chem. C* **2008**, *112*, 18737-18753.

(16) Kamat, P. V. Quantum Dot Solar Cells. The Next Big Thing in Photovoltaics. *JPCL* **2013**, *4*, 908-918.

(17) Sargent, E. H. Colloidal quantum dot solar cells. *Nat Photon* **2012**, *6*, 133-135.

(18) Zhang, F.; Zhong, H.; Chen, C.; Wu, X.-g.; Hu, X.; Huang, H.; Han, J.; Zou, B.; Dong, Y. Brightly Luminescent and Color-Tunable Colloidal CH3NH3PbX3 (X = Br, I, Cl) Quantum Dots: Potential Alternatives for Display Technology. *ACS Nano* **2015**, *9*, 4533-4542.

(19) Lindblad, R.; Bi, D.; Park, B.-w.; Oscarsson, J.; Gorgoi, M.; Siegbahn, H.; Odelius, M.; Johansson, E. M. J.; Rensmo, H. Electronic Structure of TiO2/CH3NH3PbI3 Perovskite Solar Cell Interfaces. *JPCL* **2014**, *5*, 648-653.

(20) Gonzalez-Carrero, S.; Galian, R. E.; Perez-Prieto, J. Maximizing the emissive properties of CH3NH3PbBr3 perovskite nanoparticles. *J. Mater. Chem. A* **2015**, *3*, 9187-9193.

(21) Chen, S.; Goh, T. W.; Sabba, D.; Chua, J.; Mathews, N.; Huan, C. H. A.; Sum, T. C. Energy level alignment at the methylammonium lead iodide/copper phthalocyanine interface. *APL Materials* **2014**, *2*, 081512.

(22) Muthu, C.; Agarwal, S.; Vijayan, A.; Hazra, P.; Jinesh, K. B.; Nair, V. C. Hybrid Perovskite Nanoparticles for High-Performance Resistive Random Access Memory Devices: Control of Operational Parameters through Chloride Doping. *Adv. Mater. Interfaces* **2016**, *3*, 1600092.

(23) Ahmed, G. H.; Liu, J.; Parida, M. R.; Murali, B.; Bose, R.; AlYami, N. M.; Hedhili, M. N.; Peng, W.; Pan, J.; Besong, T. M. D.; Bakr, O. M.; Mohammed, O. F. Shape-Tunable Charge Carrier Dynamics at the Interfaces between Perovskite Nanocrystals and Molecular Acceptors. *JPCL* **2016**, *7*, 3913-3919.

(24) Boaz, H.; Rollefson, G. K. The Quenching of Fluorescence. Deviations from the Stern-Volmer Law. *J. Am. Chem. Soc.* **1950**, *72*, 3435-3443.

(25) Biadala, L.; Siebers, B.; Gomes, R.; Hens, Z.; Yakovlev, D. R.; Bayer, M. Tuning Energy Splitting and Recombination Dynamics of Dark and Bright Excitons in CdSe/CdS Dot-in-Rod Colloidal Nanostructures. *J. Phys. Chem. C* **2014**, *118*, 22309-22316.

(26) Lakowicz, J. R.: *Principles of Fluorescence Spectroscopy*; Springer, 2007.

(27) Niklas, J.; Poluektov, O. G. Charge Transfer Processes in OPV Materials as Revealed by EPR Spectroscopy. *Adv. Energy Mater.* **2017**, 1602226-n/a.

(28) Mardis, K. L.; Webb, J. N.; Holloway, T.; Niklas, J.; Poluektov, O. G. Electronic Structure of Fullerene Acceptors in Organic Bulk-Heterojunctions: A Combined EPR and DFT Study. *JPCL* **2015**, *6*, 4730-4735.

(29) Witt, F.; Kruszynska, M.; Borchert, H.; Parisi, J. Charge Transfer Complexes in Organic−Inorganic Hybrid Blends for Photovoltaic Applications Investigated by Light-Induced Electron Spin Resonance Spectroscopy. *JPCL* **2010**, *1*, 2999-3003.

(30) Heinemann, M. D.; von Maydell, K.; Zutz, F.; Kolny-Olesiak, J.; Borchert, H.; Riedel, I.; Parisi, J. Photo-induced Charge Transfer and Relaxation of Persistent Charge Carriers in Polymer/Nanocrystal Composites for Applications in Hybrid Solar Cells. *Adv. Funct. Mater.* **2009**, *19*, 3788-3795.

(31) Marcus, R. A. On the theory of oxidation-reduction reactions involving electron transfer. I. *J. Chem. Phys.* **1956**, *24*, 966-978.

(32) Lefrançois, A.; Luszczynska, B.; Pepin-Donat, B.; Lombard, C.; Bouthinon, B.; Verilhac, J.-M.; Gromova, M.; Faure-Vincent, J.; Pouget, S.; Chandezon, F.; Sadki, S.; Reiss, P. Enhanced Charge Separation in Ternary P3HT/PCBM/CuInS2 Nanocrystals Hybrid Solar Cells. *Sci. Rep.* **2015**, *5*, 7768.

(33) Nelson, J. Diffusion-limited recombination in polymer-fullerene blends and its influence on photocurrent collection. *Phys. Rev. B* **2003**, *67*, 155209.

(34) Krinichnyi, V. I.: *Multi Frequency EPR Spectroscopy of Conjugated Polymers and Their Nanocomposites*; CRC Press LLC, 2016.

(35) Weil, J. A.; Bolton, J. R.; Wertz, J. E.: *Electron Paramagnetic Resonance: Elementary Theory and Practical Applications*; Wiley, 1994.

(36) Varga, A.; Endrődi, B.; Hornok, V.; Visy, C.; Janáky, C. Controlled Photocatalytic Deposition of CdS Nanoparticles on Poly(3-hexylthiophene) Nanofibers: A Versatile Approach To Obtain Organic/Inorganic Hybrid Semiconductor Assemblies. *J. Phys. Chem. C* **2015**, *119*, 28020-28027.

(37) Endrodi, B.; Mellar, J.; Gingl, Z.; Visy, C.; Janaky, C. Reasons behind the improved thermoelectric properties of poly(3-hexylthiophene) nanofiber networks. *RSC Advances* **2014**, *4*, 55328-55333.

(38) Duong, D. T.; Wang, C.; Antono, E.; Toney, M. F.; Salleo, A. The chemical and structural origin of efficient p-type doping in P3HT. *Org. Electron.* **2013**, *14*, 1330-1336.

(39) Aguirre, A.; Gast, P.; Orlinskii, S.; Akimoto, I.; Groenen, E. J. J.; El Mkami, H.; Goovaerts, E.; Van Doorslaer, S. Multifrequency EPR analysis of the positive polaron

in I2-doped poly(3-hexylthiophene) and in poly[2-methoxy-5-(3,7-dimethyloctyloxy)]-1,4-phenylenevinylene. *PCCP* **2008**, *10*, 7129-7138.

(40) Camaioni, N.; Tinti, F.; Franco, L.; Fabris, M.; Toffoletti, A.; Ruzzi, M.; Montanari, L.; Bonoldi, L.; Pellegrino, A.; Calabrese, A.; Po, R. Effect of residual catalyst on solar cells made of a fluorene-thiophene-benzothiadiazole copolymer as electron-donor: A combined electrical and photophysical study. *Org. Electron.* **2012**, *13*, 550-559.

(41) Pan, J.; Quan, L. N.; Zhao, Y.; Peng, W.; Murali, B.; Sarmah, S. P.; Yuan, M.; Sinatra, L.; Alyami, N. M.; Liu, J.; Yassitepe, E.; Yang, Z.; Voznyy, O.; Comin, R.; Hedhili, M. N.; Mohammed, O. F.; Lu, Z. H.; Kim, D. H.; Sargent, E. H.; Bakr, O. M. Highly Efficient Perovskite-Quantum-Dot Light-Emitting Diodes by Surface Engineering. *Adv. Mater.* **2016**, *28*, 8718-8725.

(42) Pan, J.; Sarmah, S. P.; Murali, B.; Dursun, I.; Peng, W.; Parida, M. R.; Liu, J.; Sinatra, L.; Alyami, N.; Zhao, C.; Alarousu, E.; Ng, T. K.; Ooi, B. S.; Bakr, O. M.; Mohammed, O. F. Air-Stable Surface-Passivated Perovskite Quantum Dots for Ultra-Robust, Single- and Two-Photon-Induced Amplified Spontaneous Emission. *The JPCL* **2015**, *6*, 5027-5033.

(43) Vorobiev, A. K.; Chumakova, N. A. Determination of orientation distribution function of anisotropic paramagnetic species by analysis of ESR spectra angular dependence. *J. Magn. Reson.* **2005**, *175*, 146-157.

(44) Spano, F. C. The Spectral Signatures of Frenkel Polarons in H- and J-Aggregates. *Acc. Chem. Res.* **2010**, *43*, 429-439.

(45) Clark, J.; Silva, C.; Friend, R. H.; Spano, F. C. Role of Intermolecular Coupling in the Photophysics of Disordered Organic Semiconductors: Aggregate Emission in Regioregular Polythiophene. *Phys. Rev. Lett.* **2007**, *98*, 206406.

SUMMARY

The need of a viable technology to tackle the global energy issue is urgent. Solar photovoltaics represents one of the most efficient response of the human kind to answer the increasing demand for energy. However, for real progress, a low-cost and highly efficient source of energy is desirable. In order to achieve this purpose, the development of new materials that take advantage of the knowledge frontiers in nanotechnology is crucial and the deep understanding of the photophysics behind nanostructured photovoltaic devices is essential.

The work presented in this thesis addresses towards the development and the photo-physical characterization of three different families of nanostructures (namely, (1) colloidal Quantum Dots, (2) carbon dots, and (3) hybrid organic/inorganic perovskite nanoparticles) blended with common organic photovoltaic materials. The main aim of the work is to thoroughly investigate the photo-physical and morphological interactions between the nanostructures and the organic materials in order to unravel the photophysics behind Quantum Dots Bulk Heterojunction (BHJ) Solar Cells and to suggest these hybrid nanostructured composite materials for next-generation solar cells.

The first emphasis of the work (**Chapter 3**) lies on the spectroscopic study of a prototypical BHJ active layer consisting in binary blends of fullerene derivative PCBM and CdSe/CdS core-shell Quantum Dots (QDs) capped with different ligands. The study unravels that QDs play a pivotal role role on the photophysical processes of the photoactive materials. In particular, QDs presence favours the charge transfer and charge separation processes and hinders the loss mechanism of charge recombination. On the other hand, QDs introduce deep trap levels for the charge carriers which are localized in proximity of QDs. In addition, the role of the length and the nature of the

ligands on electron transfer process is investigated and an enhanced charge transfer process is observed and rationalized in case of shorter ligands with thiol functionality.

In C**hapter 4**, the synthesis and photo-physical characterization of N-doped carbon dots (CDs) functionalized with two different thiophene-containing groups is described. The functionalization reveals to enhance the electron donating properties of the CDs and improve their solubility in nonpolar solvents in order to blend them with PCBM. The photophysical analysis carried out in solution allows to get a deep insight into the triplet excited states of CDs and sets TREPR as the prince technique for their investigation. In addition, the study of PCBM/CDs blends shows a strong photoinduced electron transfer between functionalized CDs and PCBM and promotes these systems as suitable active materials for all-carbon solar cells.

Finally, the last part of the thesis (**Chapter 5**) takes advantage of the main results of Chapter 3 and of the properties of hybrid perovskite nanoparticles (PNPs). In particular, the synthesis of PNPs functionalized with different ligands and the investigation of their interactions with two well-known organic photovoltaic materials (namely, the fullerene derivative PCBM, and the semiconducting polymer P3HT) are presented. In PCBM/PNPs blend an enhanced charge transfer and its dependence on ligand length, a favoured charge separation and deep trap states localized in proximity of PNPs are revealed analogously to PCBM/QDs blends. On the other hand, P3HT/PNPs blends disclose a triple contribution of the PNPs on the properties of P3HT: (1) an increment of the dimension of P3HT crystalline domains, (2) a p-doping of the P3HT, and (3) the extended formation of π-stacking between adjacent monomers of P3HT (H-aggregates).

To conclude, the results of my work underpin the relevance of applying nanostructured architectures in organic photovoltaic materials, highlighting their beneficial role not only in morphology, but also in the main photo-physical processes that occurs in solar cells. Additionally, the relevant role of the tailored surface engineering of nanostructures in the process of solar energy conversion is evidenced. All these observations aim at being beneficial to the design and the fabrication of highly efficient solar cells.

APPENDIX A.

PARTIALLY ORIENTED PHASES

Electron Paramagnetic Resonance spectroscopy is a well-suited technique for the investigation of molecular orientation within a partially oriented phase due to the anisotropy of the magnetic interactions. Indeed, partially oriented systems, such as liquid crystals or spin-coated films, show a significant dependence of the EPR spectrum on the orientation of the sample in the magnetic field of the spectrometer. In recent years, many research efforts have been focused toward the study of the molecular orientation within photovoltaic polymer/fullerene blends by means of EPR spectroscopy. This rising interest can be understood considering the pivotal role which is played by the morphology of the photoactive layers of the solar cells.

In this thesis, the adopted orientational distribution, which successfully reproduces the EPR spectra reported in Chapter 5, is taken from the theory of liquid crystals forming uniaxial nematic phases. In these systems, the orientational order is described by the distribution function p(θ) that is defined by the following relationship:

$$\mathrm{p}(\theta) = \frac{1}{Q} e^{-U(\theta)/k_B T} \qquad (1)$$

where Q is the partition function and U(θ) the orienting potential, which depends on the angle θ between the molecular symmetry axis and the nematic director.

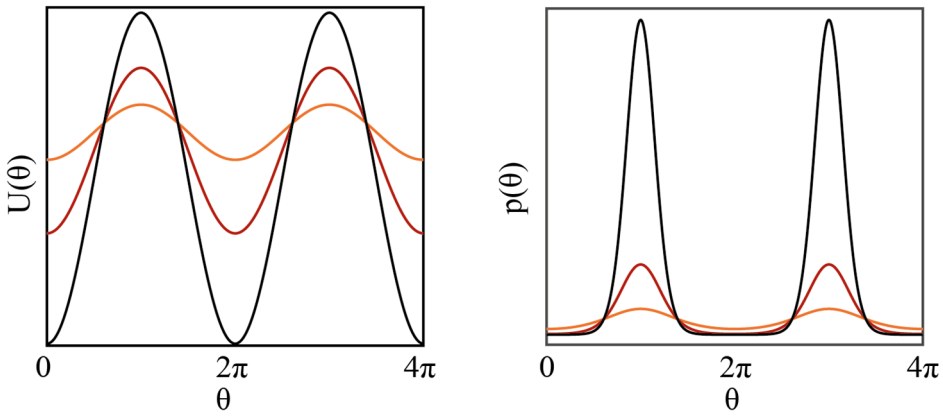

Figure A.1 Orientational potential U(θ) (left) and distribution function p(θ) (right) for different values of ε coefficient. Legend: black line: ε = 6, red line: ε = 3, orange line: ε = 1.

The orienting potential can be expanded as a sum of the Legendre polynomials $P_L(\cos\theta)$ with even values of L. To a first approximation, the sum can be truncated to the first even term $P_2(cos\theta) = \frac{1}{2}(3\cos^2\theta - 1)$, leading to:

$$p(\theta) = \frac{1}{Q} e^{-\frac{\varepsilon_{2,0}}{2k_BT}(1-3cos^2\theta)} \qquad (2)$$

Here, $\varepsilon_{2,0}$ parameter, also called 'potential coefficient', has the dimension of an energy and determines the degree of order. In liquid crystals, the orientation of the molecules results from a thermal equilibrium condition, while in spin-coating films the orientation depends on the deposition conditions and the interactions between the molecules and the substrate. Therefore, in our case $\varepsilon_{2,0}/k_BT$ should be considered as a phenomenological parameter that can be replaced by the adimensional ε coefficient. For positive values of ε, the preferred orientation corresponds to θ=0°, i.e. the molecular axis is mainly parallel to the director. Negative ε, by contrast, implies that the molecular axis lies preferentially perpendicular to the director (orientational distribution function peaked at θ=90°). The absolute value of ε determines the width of the p(θ) peaks: the higher is |ε| the smaller is the width, meaning that a greater number of molecules orients its axis parallel or perpendicular to the director. In Figure A.1, the representation of the orientational potential U(θ) (left) and distribution function p(θ) is reported for three values of adimensional ε coefficient.

To carry out the best-fit spectral simulation of EPR spectra reported in chapter 5, the normal to the film plane was considered as suitable director and the ε parameter was assumed to be temperature independent in a large range of temperatures. Spectral simulations were carried out using a home-made program implemented in Matlab and including some routines from the Matlab toolbox Easyspin.

PUBLICATIONS AND CONFERENCE CONTRIBUTIONS

5.7 LIST OF PUBLICATIONS

1. "Hybrid organic/inorganic perovskites composites: towards the enhancement of structural and electrical properties"
   Alberto Privitera*, Marcello Righetto, Michele De Bastiani, Francesco Carraro, Marzio Rancan, Lidia Armelao, Gaetano Granozzi, Renato Bozio, and Lorenzo Franco
   J. Phys. Chem. Lett., **2017**, 8, 5981–5986.

2. "The central role of ligands in electron transfer from perovskite nanocrystals"
   Alberto Privitera*, Marcello Righetto, Renato Bozio and Lorenzo Franco
   MRS Advances, **2017**, 1-9.

3. "Spectroscopic Insights into Carbon Dot Systems"
   Marcello Righetto, Alberto Privitera, Ilaria Fortunati, Dario Mosconi, Mirco Zerbetto, M. Lucia Curri, Michela Corricelli, Alessandro Moretto, Stefano Agnoli, Lorenzo Franco, Renato Bozio, and Camilla Ferrante*
   J. Phys. Chem. Lett. **2017**, 8, 2236−2242.

4. "Boosting Carbon Quantum Dots/Fullerene electron transfer via surface group engineering"
   Alberto Privitera, Marcello Righetto, Dario Mosconi, Francesca Lorandi, Abdirisak A. Isse, Alessandro Moretto, Renato Bozio, Camilla Ferrante, Lorenzo Franco*
   Phys. Chem. Chem. Phys., **2016**, 18, 31286-31295

5. "Synthesis and Photochemical Applications of Processable Polymers Enclosing Photoluminescent Carbon Quantum Dots"
   Dario Mosconi, Daniela Mazzier, Simone Silvestrini, Alberto Privitera, Carla Marega, Lorenzo Franco, Alessandro Moretto*
   ACS Nano, **2015,** 9, 4156-4164.

6. "Optical Excitation Dynamics at Hetero-Interfaces Fullerene/Quantum Dots"
   Marcello Righetto*, Alberto Privitera, Lorenzo Franco, Renato Bozio
   Organic, Hybrid, and Perovskite Photovoltaics XVIII 10363, 103632D
   (Conference Proceeding)

7. "Engineering Interactions in QDs-PCBM Blends: A Surface Chemistry Approach."
   Marcello Righetto, Alberto Privitera, Luca Bolzonello, Camilla Ferrante, Lorenzo Franco and Renato Bozio*
   In preparation.

5.8 CONFERENCE CONTRIBUTIONS

1. *"Photophysics of New Nanomaterials for Organic and Hybrid Solar Cells"*
   MRS-Spring Meeting, Phoenix, USA (2017)
   Oral contribution

2. *"Boosting Carbon Quantum Dots/Fullerene electron transfer via surface group engineering"*
   HOPV16, Swansea, UK (2016)
   Oral Contribution

3. *"Carbon Quantum Dots with Enhanced Electron Donor Capabilities for 'all-Carbon' Solar Cells"*
   HOPV16, Swansea, UK (2016)
   Poster

4. *"Enhanced Charge Transfer and Separation in PCBM/CdSe Quantum Dots Photoactive Films"*
   Xth EFEPR Conference, Torino, Italy (2016)
   Poster

5. *"N-doped Carbon QDs for Organic Solar Cells"*
   Bressanone Summer School, Bressanone, Italy (2015)
   Oral contribution